Title

Interface Engineering for Efficient and Stable Perovskite Thin-Film Solar Cells

ISBN

9798190928860

Author

Yang, Wenxin

Publication Date

2026-09-11

Peer reviewed|Thesis/dissertation

UNIVERSITY OF CALIFORNIA

Los Angeles

Interface Engineering for Efficient and Stable Perovskite Thin-Film Solar Cells

A dissertation submitted in partial satisfaction of the requirements

for the degree Doctor of Philosophy

in Materials Science and Engineering

by

Wenxin Yang

2026

ABSTRACT OF THE DISSERTATION

Interface Engineering for Efficient and Stable Perovskite Thin-Film Solar Cells

by

Wenxin Yang

Doctor of Philosophy in Materials Science and Engineering

University of California, Los Angeles, 2026

Professor Yang Yang, Chair

Metal-halide perovskite solar cells have attracted tremendous interest because of their compatibility with low-temperature processing, strong optical absorption, defect tolerance, and tunable electronic structures. Despite rapid improvements in power conversion efficiency, their practical deployment remains limited by insufficient operational stability. Interfaces are particularly important because they simultaneously govern charge extraction, non-radiative recombination, ionic redistribution, chemical reactions, and, at buried interfaces, the formation of the perovskite absorber itself. This dissertation investigates how molecularly engineered

polymeric interfaces can regulate these coupled electronic, ionic, and structural processes to improve both the efficiency and long-term stability of perovskite solar cells.

Chapter One introduces the fundamental properties and stability challenges of metal-halide perovskites, with particular emphasis on the multifunctional roles of interfaces. Electronic defect passivation, ionic and chemical stabilization, and buried-interface regulation of nucleation and crystal growth are established as complementary strategies for interface engineering.

Chapter Two focuses on defect passivation at the exposed perovskite surface. hree polymeric modifiers, including poly(vinyl acetate), polyethylene glycol, and poly(9-vinylcarbazole), are systematically compared to establish a molecular design principle linking electronic structure and steric accessibility with defect-interaction strength. Stronger Lewis-base interactions with undercoordinated Pb species suppress non-radiative recombination, improve charge transport, and substantially enhance device efficiency and operational stability.

Chapter Three extends the discussion from the exposed surface to the buried interface, highlighting its dual role as a dynamic ionic boundary during operation and as a template for perovskite formation during fabrication.

Chapter Four identifies cross-interface Sn redistribution from SnO_2 into the perovskite absorber as an important degradation pathway during prolonged operation. Sn migration is accompanied by chemical-state evolution, while ultrathin polymeric interlayers increase the energetic barrier for ionic transport and suppress Sn redistribution, leading to markedly improved long-term stability.

Chapter Five demonstrates that the same buried interlayers also regulate perovskite formation by modifying wettability, interfacial contact, crystallization, phase quality, and defect

formation. These changes reduce non-radiative recombination and enable high-efficiency small-area devices and modules.

Together, these studies establish polymeric interface engineering as a strategy for simultaneously controlling defect chemistry, ionic transport, buried-interface evolution, and perovskite formation, providing design principles for efficient and durable perovskite photovoltaics.

The dissertation of Wenxin Yang is approved.

Yuzhang Li

Nathan Szymanski

Jaime Marian

Yang Yang, Committee Chair

University of California, Los Angeles

2026

Dedicated to all the people who helped me.

CONTENTS

LIST OF FIGURES

Acknowledgment

My five-year journey has been far too long to be captured in just one or two pages, yet far too short to fully express my gratitude to everyone who has supported me along the way. This unforgettable chapter of my life would not have been possible without the kindness, encouragement, and generous help of so many wonderful people.

I would first like to express my sincerest gratitude to my advisor, Professor Yang Yang, for his guidance and support throughout my Ph.D. journey. I still vividly remember what he told me when we first met: to think outside the box, to search for the "blue ocean" and, at the same time, to build a strong foundation and develop rigorous, logical thinking. Beyond research, the values he has instilled in me including integrity, perseverance, and wholehearted dedication, have been equally important. Of all the things I have learned from Professor Yang, I believe these lessons will stay with me and continue to guide me through both the highs and lows of my future journey.

I would also like to express my sincere appreciation to my committee members, Professor Jaime Marian, Professor Yuzhang Li, and Professor Nathan Szymanski, for their valuable suggestions, thoughtful feedback, and generous support throughout my Ph.D. studies.

I am also deeply grateful to Dr. Yepin Zhao, who has been not only a technical mentor to me, but also like a big brother throughout my Ph.D. journey. Knowing him not only as a researcher, but more importantly as a great friend and a wonderful person, has meant a great deal to me.

I would also like to express my sincere appreciation to all my wonderful collaborators. I am grateful to Dr. Minhuan Wang from Dalian University of Technology; Professor Jing Cao and Zhen-Yang Suo from Lanzhou University; Professor Ilhan Yavuz from Marmara University; Professor Anatoly I. Frenkel and Weixuan Huang from Stony Brook University; Professor Jin-

Wook Lee, Dr. Joo-Hong Lee from Seoul National University; Professor Xiaoqing Pan, Dr. Jian-Guo Zheng and Dr. Mingjie Xu from UC Irvine; Yuran Shi, Chia-Yu Lin, Mr Aman Dhilon and Elizabeth Zhang from Stanford University; Dr. Ao Zhang and Dr. Ignacio Martini from UCLA for their valuable collaboration, assistance, and support.

I also feel incredibly fortunate to have shared so many unforgettable memories with wonderful group members and friends. I am deeply grateful to Dr. Haoxiang Duan, Dr. Zhichao Shen, Dr. Yu-Che Lin, Xinyang Tong, Zehao Xie, Ming Gong, Dr. Ran Zheng, Dr. Dong Meng, Dr. Jinsung Kim, Dr. Ying Zhang, Dr. Yingke Zhu, Professor Chunqing Ma, Dr Junkai Liu, Zhihang Jin, Yiushun Tong, Tso-An Yang, Dr. Zongqi Li, Qiyu Xing, Dr. Bin Chang, Tzu-Hsuan Wang, Dr. Ruxing Fu for their generous help, support, and companionship throughout my Ph.D. journey. I would also like to thank Ruitao Wang, Qingcheng Zeng, Haoyu Yang, Kangrui Li and Yanhao Sun for their unwavering friendship and for being such an important part of this journey. I am also grateful to Dr. Marta Pozuelo for giving me my first opportunity to serve as a teaching assistant, and to Dr. Isabella Kim, Dr. Kede Liu, and Dr. HyeonJi Hong for their support, collaboration, and guidance throughout my teaching assistant experience.

To my girlfriend, Jingyi Wu, your love, support, patience, and understanding have given me both calmness and strength whenever I needed them most. I am deeply grateful to have you by my side throughout this journey.

Lastly, to my parents, your unwavering love and support have always been my safe harbor, giving me the strength and courage to ride every wave and explore wherever life may take me.

Chapter 2 is adapted from work published in *Joule* **6**, 1032–1048 (2022), published by Cell Press. Chapter 4 and 5 are adapted from work accepted for publication in *Nature Communication* (2026).

VITA

2017-2021 Bachelor of Science, Materials Science and Engineering
Tianjin University

2021-2026 PhD Candidate, Materials Science and Engineering
University of California, Los Angeles

2021-2026 Teaching Fellow, Materials Science and Engineering
University of California, Los Angeles

2026 Device and Process Integration intern
Micron Technology

Chapter 1 Introduction to Perovskite Solar Cells and Interface Engineering

1.1 Status and Challenges of Halide Perovskite Solar Cell

For decades, the increasing global demand for energy, together with growing concerns over environmental pollution and climate change, has driven extensive efforts toward the development of clean and sustainable energy technologies. Among various renewable energy sources, solar energy has attracted particular attention because of its abundance, broad geographical availability, environmental compatibility, and renewable nature. Photovoltaic (PV) devices, commonly referred to as solar cells, directly convert incident solar radiation into electrical energy and have become an important technology for sustainable electricity generation.

Currently, crystalline silicon (c-Si) photovoltaics dominate the global PV market, while cadmium telluride (CdTe) represents the most successful commercial thin-film photovoltaic technology. Benefiting from decades of technological development and industrial optimization, these established photovoltaic technologies offer high power conversion efficiencies (PCEs), mature large-scale manufacturing processes, competitive production costs, and long operational lifetimes. Nevertheless, opportunities remain for photovoltaic technologies with simpler fabrication, reduced energy consumption, lower material usage, and greater compatibility with lightweight and flexible form factors. Conventional c-Si photovoltaics rely on high-purity silicon production, crystal growth, wafer slicing, and multiple energy-intensive processing steps. CdTe photovoltaics enable comparatively streamlined thin-film manufacturing, but their continued large-scale expansion faces considerations associated with tellurium availability, further improvements in conversion efficiency, and end-of-life material management. These considerations have motivated extensive research into emerging photovoltaic technologies that

may complement established PV platforms while offering new opportunities for low-cost, low-temperature, and versatile manufacturing.

Among various emerging photovoltaic technologies, metal halide perovskite solar cells (PSCs) have attracted intensive research interest owing to their excellent optoelectronic properties, compositional tunability, compatibility with low-temperature and solution-based processing, and potential for high-efficiency photovoltaic applications[1]. Metal halide perovskites used for photovoltaics generally adopt the chemical formula ABX_3, where A is a monovalent cation, typically formamidinium (FA^+), methylammonium (MA^+), or cesium (Cs^+); B is a divalent metal cation, most commonly Pb^{2+} or Sn^{2+}; and X is a monovalent halide anion, such as I^-, Br^-, or Cl^-. In the three-dimensional perovskite structure, corner-sharing BX_6 octahedra form the inorganic framework, while the A-site cations occupy the cavities within this framework.

In a typical PSC, the perovskite semiconductor serves as the photoactive absorber and is sandwiched between selective charge-transport layers and two electrodes[2]. Depending on the sequence of these functional layers, PSCs are commonly classified into conventional n–i–p and inverted p–i–n architectures. The electron-transport layer (ETL) and hole-transport layer (HTL) selectively extract photogenerated electrons and holes, respectively. Together with the perovskite absorber and electrodes, these functional layers constitute the basic device architecture required for efficient photon absorption, charge generation, transport, and collection.

Metal halide perovskites possess several distinctive optoelectronic properties that make them particularly attractive as photovoltaic absorbers. First, their electronic structures can be readily tailored through compositional engineering at the A, B, and X sites[3] (**Figure 1.2A**). Substitution of the metal and halide components enables the bandgap to be tuned over a broad range relevant to photovoltaic applications, from approximately 1.2 eV in Sn–Pb mixed

perovskites to above 2.2 eV in Br-rich Pb-based compositions. This tunability distinguishes metal halide perovskites from conventional semiconductors such as crystalline silicon, whose bandgap is largely fixed by the intrinsic electronic structure of the material, and enables perovskite compositions to be optimized for both single-junction and tandem photovoltaic applications.

Second, many metal halide perovskites exhibit a relatively high degree of defect tolerance[4]. Although solution-processed perovskite films can contain substantial densities of structural imperfections, many dominant intrinsic point defects generate relatively shallow electronic states rather than deep states within the bandgap. Consequently, these defects can be less detrimental to non-radiative Shockley–Read–Hall recombination than deep-level defects commonly encountered in conventional semiconductors. When detrimental deep traps are sufficiently suppressed, perovskite absorbers can therefore exhibit low non-radiative recombination rates, long carrier lifetimes, and long carrier diffusion lengths despite being fabricated through comparatively low temperature processes[5,6]. It should be noted, however, that defect tolerance is strongly dependent on composition and defect type, and deep defects at surfaces, grain boundaries, and interfaces can still substantially limit device performance.

Third, photovoltaic metal halide perovskites are predominantly direct-bandgap semiconductors with strong optical transitions and high absorption coefficients, commonly on the order of 10^5 cm^{-1} in the visible spectral region. As a result, a perovskite layer only several hundred nanometers thick can absorb a large fraction of incident sunlight, enabling efficient light harvesting with substantially less absorber material than is required for indirect-bandgap crystalline silicon. The combination of strong optical absorption, favorable charge-transport properties, long carrier diffusion lengths, and tunable electronic structure provides a compelling materials basis for the high photovoltaic performance achieved by PSCs.

These attractive optoelectronic and processing characteristics have driven intensive research into metal halide perovskites and underpinned the exceptionally rapid progress of perovskite photovoltaics. Since the first demonstration of a perovskite-sensitized solar cell with a PCE of 3.8% in 2009[1], the efficiency of single-junction PSCs has increased dramatically, with independently confirmed efficiencies reaching approximately 28% in 2026, approaching those of state-of-the-art crystalline silicon solar cells[7] (**Figure 1.1**). In parallel with advances in laboratory-scale devices, increasing efforts have been devoted to translating perovskite photovoltaics from small-area cells toward large-area devices and modules through scalable deposition and manufacturing processes, representing important steps toward eventual commercialization[8].

Despite this remarkable progress, long-term operational stability remains one of the most critical challenges facing perovskite photovoltaics. The commercial viability of a photovoltaic technology is ultimately determined by the interplay among power conversion efficiency, manufacturing cost, and operational lifetime (**Figure 1.2B**)[9]. While PSCs have already demonstrated efficiencies comparable to those of established crystalline silicon technologies at the laboratory scale and offer the potential for cost-effective manufacturing through low-temperature and scalable processing, their long-term durability remains substantially inferior to that of commercial silicon photovoltaics[10]. Bridging this stability gap is therefore essential for translating the outstanding laboratory performance of PSCs into reliable and economically viable photovoltaic technologies.

The stability limitations of metal halide perovskites arise from a combination of their intrinsic material properties and externally imposed stressors. Metal halide perovskites possess a relatively soft and dynamically disordered ionic lattice, which contributes to their distinctive optoelectronic behavior but also results in comparatively low activation barriers for the migration

of ionic species and ionic defects[11,12]. Under illumination, elevated temperature, or an electric field, mobile ionic species can redistribute within the perovskite lattice and accumulate at grain boundaries and interfaces, altering the local electronic and chemical environment. In addition, the low-temperature solution-processing methods widely used for perovskite fabrication can introduce structural and chemical imperfections, including vacancies, undercoordinated ions, grain boundaries, residual species, and interfacial defects. Although many intrinsic defects in metal halide perovskites are electronically shallow and are therefore relatively benign under pristine conditions, their redistribution and evolution during device operation can contribute substantially to long-term instability.

These intrinsic vulnerabilities can be further activated or accelerated by external stressors encountered during photovoltaic operation. In practical applications, perovskite solar cells are continuously or periodically exposed to illumination, electrical bias, elevated temperature, moisture, oxygen, and mechanical or thermal cycling[13,35] (**Figure 1.2C and D**). Effective encapsulation can substantially suppress degradation associated with the ingress of moisture and oxygen; however, operational stressors such as light, heat, and electrical bias cannot be eliminated because they are inherent to normal solar cell operation[14]. These stressors can promote ion migration, defect generation and redistribution, phase segregation, and interfacial reactions, ultimately destabilizing both the perovskite absorber and adjacent functional layers.

Although perovskite degradation does not necessarily follow a single universal sequence, a general degradation pathway can be conceptually described as the coupling of ionic redistribution, defect evolution, and chemical or structural transformation under operational stress. Ion migration and defect accumulation can modify local compositions and electric fields, facilitate interfacial reactions, and in some cases initiate phase transformation or chemical decomposition. These

changes can introduce additional non-radiative recombination pathways, impede charge transport and extraction, and progressively reduce the photovoltaic parameters of the device. Under sufficiently severe or prolonged stress, irreversible chemical reactions and decomposition of the perovskite or neighboring functional layers can ultimately lead to catastrophic device failure.

Currently, a variety of strategies have been developed to improve both the photovoltaic performance and operational stability of PSCs. These approaches can be broadly categorized into three major directions: compositional engineering, bulk and crystal engineering, and interface engineering. Each strategy targets a different aspect of the perovskite material or device structure and has contributed substantially to the rapid improvement of PSC performance.

Compositional engineering regulates the intrinsic properties of perovskite absorbers through modification of the A-, B-, or X-site components. Beyond enabling bandgap tuning, appropriate compositional design can improve phase and structural stability by optimizing lattice distortion and stabilizing the desired photoactive phase[15]. However, compositional modification must be carefully balanced, as mixed compositions may introduce phase segregation or compositional inhomogeneity under operational stress[16]. Bulk and crystal engineering focuses on regulating perovskite nucleation, growth, and crystallographic orientation during film formation[17, 18]. Through control of precursor chemistry, additives, solvent coordination, and thermal processing, the resulting grain structure, crystallinity, defect density, and residual strain can be optimized, thereby reducing non-radiative recombination and improving material stability. Nevertheless, these approaches can be sensitive to processing conditions and may become more difficult to control uniformly during large-area fabrication.

Interface engineering is another important strategy for improving PSC performance and stability. The interfaces between the perovskite absorber, charge-transport layers, and electrodes strongly influence charge extraction, non-radiative recombination, ion accumulation, and interfacial chemical reactions. Therefore, appropriate interface modification and passivation are critical for achieving efficient and stable perovskite solar cells.

1.2 Interfacial Properties and Engineering in Perovskite Solar Cell

Due to the multilayer architecture of perovskite solar cells, numerous interfaces are inevitably present within the device stack, including the interfaces between the perovskite absorber and charge-transport layers, as well as those between charge-transport layers and electrodes. Among these interfaces, the perovskite/charge-transport layer interfaces are particularly critical because they directly participate in charge extraction, transport, and interfacial interactions during device operation[19]. Even with an ideal perovskite bulk absorber possessing excellent optoelectronic properties, efficient photovoltaic operation still requires well-controlled interfaces that enable selective carrier transport and effective charge collection.

However, interfaces are intrinsically more vulnerable regions compared with bulk materials. As the termination of lattice periodicity, interfaces in crystalline semiconductors generally contain structural imperfections and unsatisfied chemical bonds. For conventional semiconductors such as silicon, broken lattice bonds at surfaces and interfaces can introduce electronic states within the bandgap and significantly affect device performance. In metal halide perovskites, the situation is further complicated by their soft ionic lattice and chemically dynamic nature[20]. The structural discontinuity, lattice mismatch, incomplete crystallization, and chemical incompatibility between perovskites and adjacent materials can generate abundant interfacial imperfections, including undercoordinated species, vacancies, residual strain, and structural

disorders. Although many intrinsic defects in perovskites exhibit relatively shallow electronic characteristics, interfacial defects can become highly detrimental due to their direct involvement in carrier transport and interfacial reactions. Interfaces therefore play essential roles in determining both the photovoltaic performance and operational stability of perovskite solar cells through coupled electronic, ionic, and chemical processes.

From an electronic perspective, interfaces regulate carrier extraction, transport, and recombination processes[21]. Properly engineered interfaces provide favorable energy-level alignment between the perovskite absorber and charge-selective layers, minimizing energetic barriers during electron and hole extraction[22]. In addition, interfacial modification can regulate work functions, band offsets, and interfacial dipoles, thereby improve charge selectivity and reduce transport losses. Conversely, interfacial defects can introduce trap states that act as recombination centers (**Figure 1.3**)[36]. Because photogenerated carriers must inevitably pass through interfaces before being collected, even a relatively small density of electronically active defects at interfaces can substantially increase non-radiative recombination, resulting in voltage losses, reduced fill-factor (FF), and degraded photovoltaic performance[23].

Beyond electronic processes, interfaces also serve as critical regions for ionic and chemical interactions (**Figure 1.4**)[36]. The ionic nature of metal halide perovskites enables the migration of mobile species under external stimuli such as electric fields, illumination, and thermal activation. Due to structural heterogeneity, local electric fields, and chemical potential gradients, interfaces can act as preferential sites for ionic accumulation and redistribution[24]. Such ionic processes can dynamically modify local electronic environments, alter defect landscapes, promote interfacial reactions, and accelerate structural degradation[25]. Furthermore, chemical incompatibility between perovskites and adjacent functional layers may induce interfacial decomposition, species diffusion,

or undesirable reactions during long-term operation. Therefore, interfaces are not only passive charge-transfer boundaries but also active regions that govern the long-term evolution of perovskite devices.

In addition to governing electronic, ionic, and chemical processes during device operation, interfaces can also influence the formation of the perovskite absorber itself. This role is particularly important at the buried interface, where the underlying charge-transport layer is already present during perovskite deposition and therefore acts as a substrate for nucleation and crystal growth[37]. Variations in surface chemistry, wettability, interfacial energy, and chemical interactions with precursor species can alter nucleation behavior, crystallization kinetics, grain formation, and interfacial morphology, ultimately affecting the structural and optoelectronic quality of the resulting perovskite film. The buried interface should therefore be considered not only as a charge-transfer boundary during device operation, but also as an active template that influences perovskite formation during fabrication.

Given the critical role of interfaces, extensive efforts have been devoted to interface engineering to simultaneously improve device efficiency and operational stability. Early interface engineering strategies primarily focused on improving the electronic quality of interfaces, while recent studies have increasingly emphasized the regulation of ionic and chemical processes during device operation. These strategies can generally be categorized into four interconnected aspects: electronic defect passivation, energetic and charge-transport regulation, ionic and chemical stabilization, and regulation of interfacial nucleation and crystal growth.

Electronic defect passivation aims to reduce electronically active defects at interfaces through chemical coordination, ionic interactions, or surface modification. A wide range of passivation materials, including molecular additives, ionic compounds, polymers, and inorganic

modifiers, have been developed to interact with undercoordinated species and suppress trap-assisted recombination[26-29]. Such approaches can improve carrier lifetime and reduce non-radiative losses, leading to enhanced photovoltaic performance. However, many passivation strategies primarily focus on improving the initial electronic quality of interfaces, while their ability to maintain interfacial integrity under prolonged operational stress remains an important consideration.

Interface modification can also regulate energy-level alignment and charge transport by tuning work functions, band offsets, and interfacial dipoles[23,30]. These approaches improve carrier selectivity and reduce extraction barriers, enabling more efficient charge collection. Compared with defect passivation, energetic regulation focuses more directly on optimizing the electronic coupling between the perovskite absorber and charge-selective layers. In practice, many interfacial modifiers can simultaneously influence both defect states and electronic structures, highlighting the multifunctional nature of interface engineering.

More recently, interface engineering has been increasingly recognized as an effective approach to regulate ionic and chemical processes[31]. Functional interlayers can serve as diffusion barriers, stabilize interfacial structures, and suppress detrimental reactions between perovskites and adjacent materials[32-34]. Achieving interfaces that simultaneously provide efficient charge extraction, suppress interfacial recombination, and maintain chemical and ionic stability during long-term operation remains a major challenge for the further development of perovskite photovoltaics.

Regulation of interfacial nucleation and crystal growth is particularly relevant at buried interfaces, where the underlying transport layer directly participates in the earliest stages of perovskite formation. By modifying surface chemistry, wettability, interfacial energy, and

precursor–substrate interactions, buried-interface engineering can regulate heterogeneous nucleation and crystal growth, thereby influencing grain structure, phase quality, interfacial morphology, and the resulting optoelectronic properties of the perovskite absorber.

Overall, interfaces in perovskite solar cells represent multifunctional regions where electronic, ionic, and chemical processes are closely coupled. While well-engineered interfaces are essential for efficient carrier extraction and suppressed recombination, they must also maintain structural and chemical integrity under continuous operational stress. Therefore, successful interface engineering requires not only improving the initial electronic quality of interfaces but also regulating their dynamic evolution during device operation. Despite significant progress in interfacial modification, achieving stable interfaces that simultaneously optimize charge transport, defect control, and long-term operational stability remains a critical challenge for advancing perovskite photovoltaics toward practical applications.

References

1 Kojima, A., Teshima, K., Shirai, Y. & Miyasaka, T. Organometal halide perovskites as visible-light sensitizers for photovoltaic cells. *Journal of the American Chemical Society* **131**, 6050–6051 (2009).

2 Lee, M. M., Teuscher, J., Miyasaka, T., Murakami, T. N., & Snaith, H. J. Efficient hybrid solar cells based on meso-superstructured organometal halide perovskites. *Science* **338**, 643-647 (2012).

3 Noh, J. H., Im, S. H., Heo, J. H., Mandal, T. N., & Seok, S. I. Chemical management for colorful, efficient, and stable inorganic–organic hybrid nanostructured solar cells. *Nano letters*, **13**, 1764-1769 (2013).

4 Yin, W.-J., Shi, T. & Yan, Y. Unusual defect physics in $CH_3NH_3PbI_3$ perovskite solar cell absorber. *Applied Physics Letters* **104**, 063903 (2014).

5 Stranks, S. D. et al. Electron-hole diffusion lengths exceeding 1 micrometer in an organometal trihalide perovskite absorber. *Science* **342**, 341–344 (2013).

6 Xing, G. et al. Long-range balanced electron- and hole-transport lengths in organic-inorganic $CH_3NH_3PbI_3$. *Science* **342**, 344–347 (2013).

7 *Best Research-Cell Efficiency Chart.*, <https://www.nlr.gov/media/docs/libraries/pv/cell-pv-eff.pdf> (2026).

8 Li, Z. *et al.* Scalable fabrication of perovskite solar cells. *Nature Reviews Materials* **3**, 18017 (2018).

9 Meng, L., You, J. & Yang, Y. Addressing the stability issue of perovskite solar cells for commercial applications. *Nature Communications* **9**, 5265 (2018).

10 Zhu, H. et al. Long-term operating stability in perovskite photovoltaics. *Nature Reviews Materials* **8**, 569–586 (2023).

11 Ball, J. M. & Petrozza, A. Defects in perovskite-halides and their effects in solar cells. *Nature Energy* **1**, 16149 (2016).

12 Eames, C. et al. Ionic transport in hybrid lead iodide perovskite solar cells. *Nature Communications* **6**, 7497 (2015).

13 Boyd, C. C., Cheacharoen, R., Leijtens, T. & McGehee, M. D. Understanding degradation mechanisms and improving stability of perovskite photovoltaics. *Chemical Reviews* **119**, 3418–3451 (2019).

14 Khenkin, M. V. et al. Consensus statement for stability assessment and reporting for perovskite photovoltaics based on ISOS procedures. *Nature Energy* **5**, 35–49 (2020).

15 Jeon, N. J. *et al.* Compositional engineering of perovskite materials for high-performance solar cells. *Nature* **517**, 476–480 (2015).

16 Chen, Z. et al. Unified theory for light-induced halide segregation in mixed halide perovskites. *Nature Communications* **12**, 2687 (2021).

17 Shi, P. et al. Oriented nucleation in formamidinium perovskite for photovoltaics. *Nature* **620**, 323–327 (2023).

18 Ma, C. et al. Unveiling facet-dependent degradation and facet engineering for stable perovskite solar cells. *Science* **379**, 173–178 (2023).

19 Schulz, P., Cahen, D. & Kahn, A. Halide perovskites: Is it all about the interfaces? *Chemical Reviews* **119**, 3349–3417 (2019).

20 deQuilettes, D. W. et al. Photo-induced halide redistribution in organic–inorganic perovskite photovoltaic materials. *Nature Communications* **7**, 11683 (2016).

21 Wang, Q. et al. Effects of interface engineering on the stability of perovskite solar cells. *Energy & Environmental Science* **10**, 516–522 (2017).

22 You, J. et al. Improved air stability of perovskite solar cells via solution-processed metal oxide transport layers. *Nature Nanotechnology* **11**, 75–81 (2016).

23 Stolterfoht, M. et al. The impact of energy alignment and interfacial recombination on the open-circuit voltage of perovskite solar cells. *Energy & Environmental Science* **12**, 2778–2788 (2019).

24 Tress, W. et al. Understanding the rate-dependent J–V hysteresis, slow time component, and aging in $CH_3NH_3Pb(I,Br)_3$ perovskite solar cells. *Energy & Environmental Science* **11**, 151–167 (2018).

25 Azpiroz, J. M. et al. Defect migration in methylammonium lead iodide and its role in perovskite solar cell degradation. *Energy & Environmental Science* **8**, 2118–2127 (2015).

26 Noel, N. K. et al. Enhanced photoluminescence and solar cell performance via Lewis base passivation of organic–inorganic lead halide perovskites. *ACS Nano* **8**, 9815–9821 (2014).

27 Jiang, Q. et al. Surface passivation of perovskite film for efficient solar cells. *Nature Photonics* **13**, 460–466 (2019).

28 Wang, R. et al. Constructive molecular configurations for surface-defect passivation of perovskite photovoltaics. *Science* **366**, 1509–1513 (2019).

29 Abate, A. et al. Supramolecular halogen bond passivation of organic–inorganic halide perovskite solar cells. *Nano Letters* **14**, 3247–3254 (2014).

30 Hou, Y. et al. A generic interface design for improving the efficiency and stability of perovskite solar cells. *Science* **358**, 1192–1197 (2017).

31 Chen, J. & Park, N.-G. Materials and methods for interface engineering toward stable and efficient perovskite solar cells. *ACS Energy Letters* **5**, 2742–2785 (2020).

32 Bi, E. et al. Diffusion engineering of ions and charge carriers for stable efficient perovskite solar cells. *Nature Communications* **8**, 15330 (2017).

33 Wang, R. et al. Buried interface engineering for efficient and stable perovskite solar cells. *Nature Photonics* **15**, 707–714 (2021).

34 Yang, S. et al. Stabilizing halide perovskite solar cells with a multifunctional interfacial layer. *Science* **365**, 473–478 (2019).

35 Li, B. et al. Fundamental understanding of stability for halide perovskite photovoltaics: The importance of interfaces. *Chem* **10**, 35–47 (2024).

36 Isikgor, F. H. et al. Molecular engineering of contact interfaces for high-performance perovskite solar cells. *Nature Reviews Materials* **8**, 89–108 (2023).

37 Luo, C. et al. Engineering the buried interface in perovskite solar cells via lattice-matched electron transport layer. *Nature Photonics* **17**, 856–864 (2023).

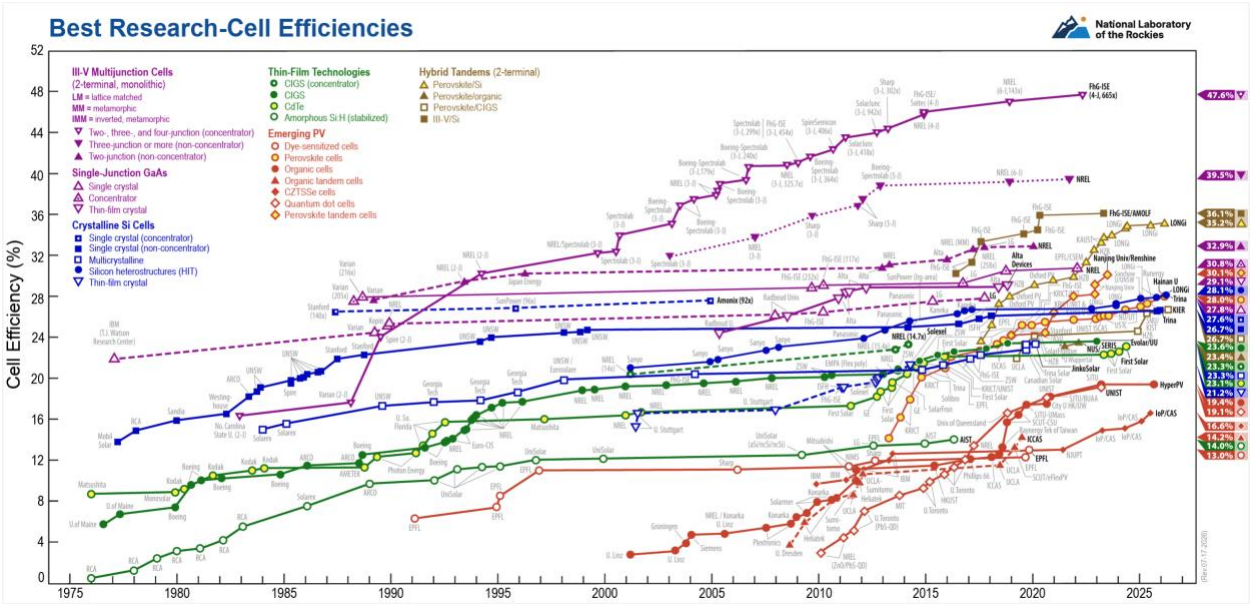

Figure 1.1 NREL best research cell efficiency chart[7].

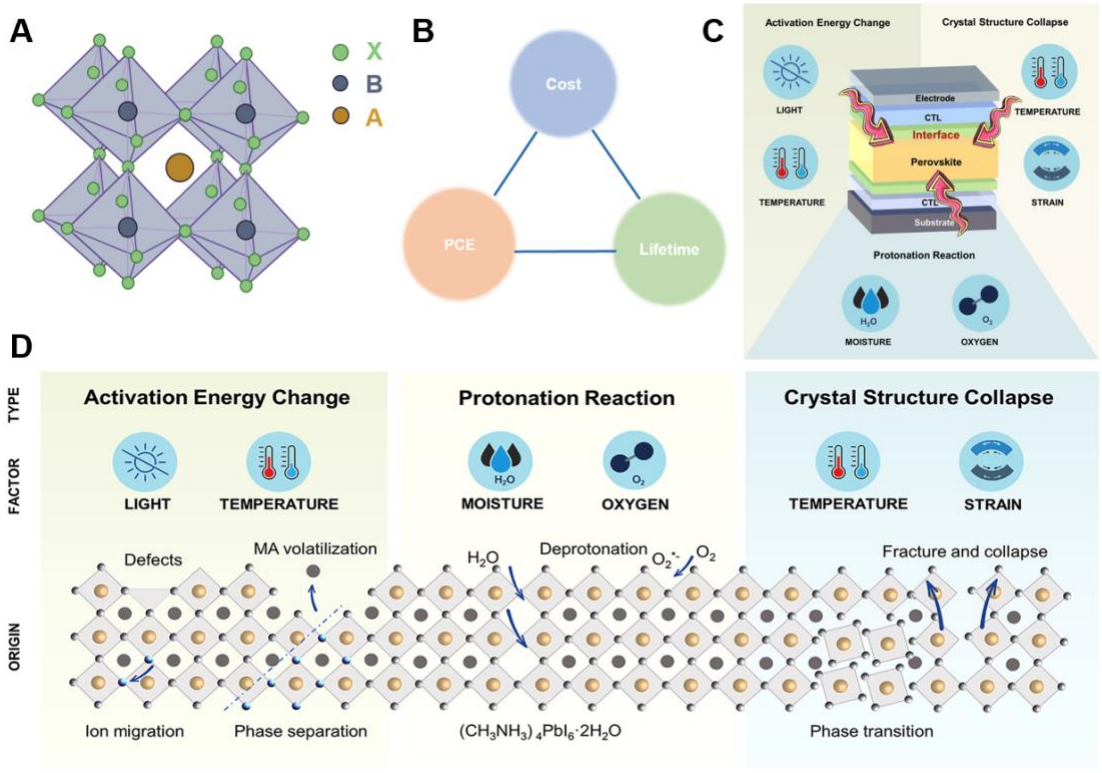

Figure 1.2 Major stability challenges and degradation pathways in metal halide perovskite solar cell. (A) Crystal structure of perovskite. (B) Solar cell performance golden triangle. (C) Perovskite degradation under different stressors[35]. (D) Schematic illustration of perovskite material degradation mechanism[35].

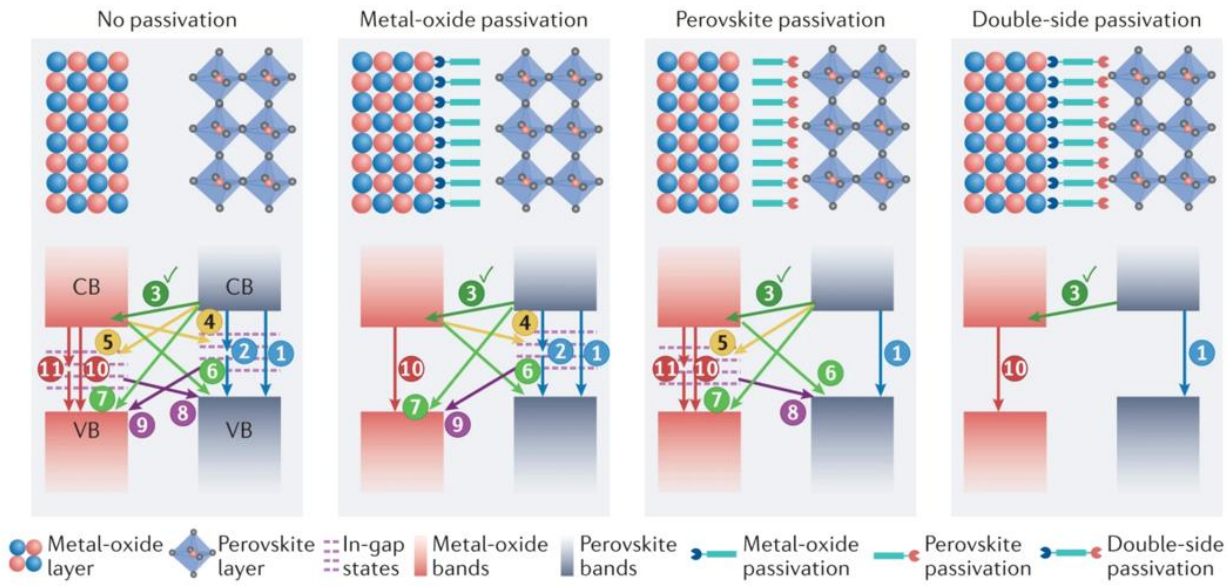

Figure 1.3 Schematic illustration of carrier dynamic pathways at metal-oxide/perovskite (n-type) interfaces with no passivation, passivation only at the metal-oxide side, passivation only at the perovskite side, and double-side passivation. CB, conduction band; VB, valence band[36].

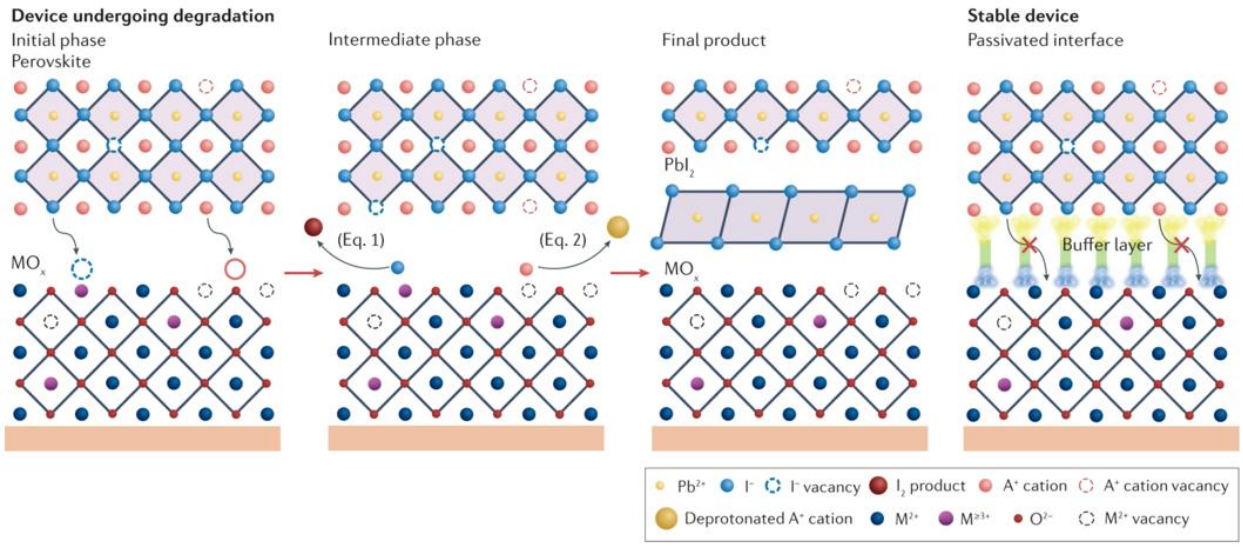

Figure 1.4 Schematic illustration of possible degradation mechanisms occurring at metal-oxide/perovskite interfaces. The intermediate phase can develop during multiple cycles, and the resulting PbI_2 phase in the final product forms at the interface. The use of a buffer layer stabilizes the system. MO_x, metal oxide[36].

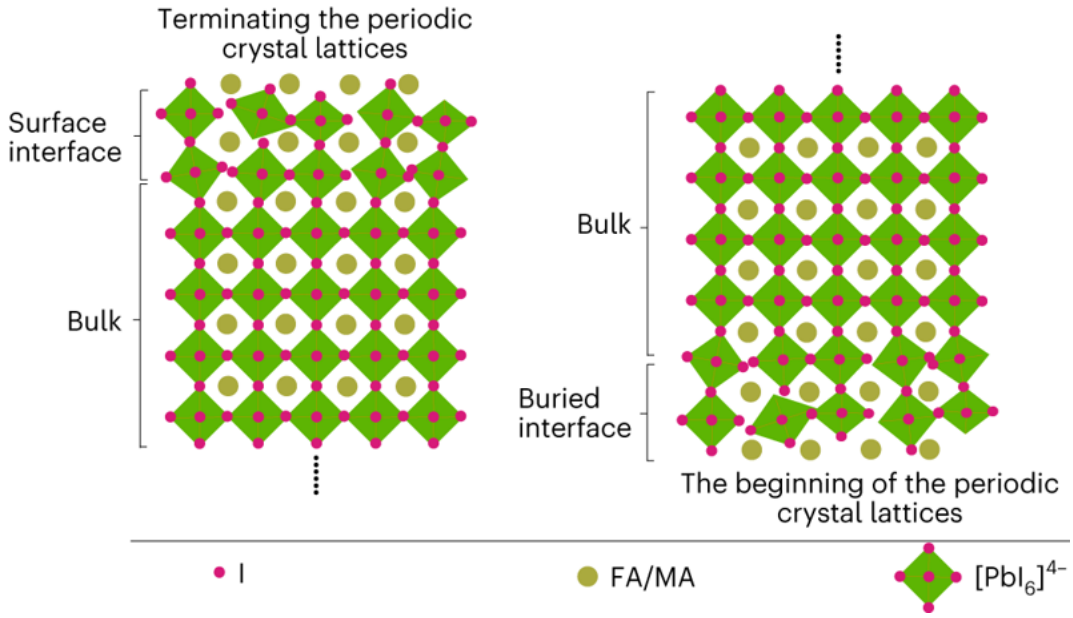

Figure 1.5 Termination and poor beginning inevitably disorder the upper and buried interfaces of the perovskite film, respectively. FA, formamidinium; MA, methylammonium[37].

Chapter 2 Polymeric Interface Engineering for Surface Defect Passivation

2.1 Interfacial Defects and Polymer-Based Passivation Strategies

Defects are ubiquitous in metal halide perovskites due to their soft ionic lattice and facile formation of lattice imperfections during material synthesis and device fabrication. In the general perovskite structure ABX_3, defects can be categorized into three major types: vacancies, interstitials, and antisite defects[1]. The intrinsic defect tolerance of metal halide perovskites enables high photovoltaic performance despite the presence of defects. However, this defect tolerance does not necessarily eliminate the detrimental effects of electronically active defects, particularly at surfaces and interfaces where defects directly interact with charge carriers.

Among these defects, halide vacancies, particularly iodine vacancies (V_I) in iodide-based perovskites, have received extensive attention due to their relatively low formation energies and significant impact on device performance[2-4]. The removal of an iodide ion from the perovskite lattice leaves undercoordinated lead species, which can introduce localized electronic states and serve as efficient carrier trapping centers. These defect states can facilitate trap-assisted Shockley–Read–Hall recombination, reducing the quasi-Fermi level splitting and leading to losses in open-circuit voltage and fill factor. In addition, halide vacancies provide migration pathways for mobile ionic species, linking defect formation with ionic redistribution and long-term device instability. Therefore, controlling iodine vacancies and related undercoordinated species is essential not only for improving initial photovoltaic performance but also for enhancing operational stability.

Other intrinsic defects, including interstitial and antisite defects, may also influence the electronic and ionic properties of perovskites[5]. However, their effects depend strongly on defect configuration and chemical environment. Compared with bulk defects, interfacial defects are particularly critical because they directly participate in carrier transport and interfacial reactions.

To mitigate the detrimental effects of interfacial defects, extensive efforts have been devoted to developing interface passivation strategies. Various passivation approaches, including molecular additives, ionic compounds, inorganic modifiers, and polymer-based materials, have been explored to chemically interact with undercoordinated species, suppress trap states, and reduce non-radiative recombination[6]. Among these approaches, polymer-based passivation has attracted increasing attention due to its unique advantages in interfacial modification[6,7]. Compared with small molecular passivators, polymers provide abundant functional groups along their backbones or side chains, enabling multiple interactions with defect sites through coordination, hydrogen bonding, or ionic interactions. In addition, the polymeric nature allows improved interfacial coverage, structural flexibility, and mechanical robustness, which enables more versatile regulation of interfacial properties and provides additional opportunities for designing robust passivation layers.

Despite significant progress in polymer-based interface passivation, the development of effective polymer modifiers has largely relied on empirical molecular selection and trial-and-error optimization. Different polymer structures may exhibit substantially different interactions with perovskite surfaces due to variations in functional groups, molecular configurations, and interfacial binding strength. However, the relationship between polymer molecular structure, defect interaction, and photovoltaic performance remains insufficiently understood. Establishing rational molecular design principles for polymer-based interface engineering is therefore essential for achieving predictable and optimized passivation effects in perovskite solar cells.

2.2 Rational Molecular Design of Polymeric Passivation Layers

The molecular structures of the selected polymers for surface modification are shown in **Figures B2.1a**–**B2.1c**. As demonstrated in the previous studies[8,9], calculated interaction energies

of model monomer can be used to estimate general trends in interaction energies of the polymers. Thus, the partial charge distribution and resultant interaction energies of the selected polymers are first investigated by density functional theory (DFT) calculation using their respective monomers (**Figure 2.1A**). Relatively stronger negative partial charge is localized on ester double-bond groups (C=O) on the side chain of the PVA monomer, whereas relatively weaker negative partial charge is found on ether bond (C–O) on the main chain of the PEG monomer. In the PVK monomer, the negative partial charge is delocalized on the carbazole functional group. The molecular interactions between the polymers and the charged surface defects on perovskite crystals are further investigated by the DFT calculation. It has been reported that the iodide vacancy (V_I) defects will most readily form on the perovskite surface due to its lowest formation energy[10,11]. The pristine film exhibited an I/Pb ratio lower than 3, which is indicative of iodide-deficient film surface (i.e., iodide vacancies, **Figure B2.2**). Therefore, we investigated the interaction between the V_I and the selected monomers based on the structural models shown in **Figures 2.1B**, **2.1E**, and **2.1H**. The PVA monomer molecule interacted strongly with the V_I defect, resulting in an interaction energy (E_{int}, defined as $E_{int} = E_{molecule\text{-}perovskite} - E_{perovskite} - E_{molecule}$)[12] of -0.590 eV, whereas the lower interaction energies of -0.536 and -0.406 eV were obtained for PEG and PVK monomers. The interaction strength followed the order PVA > PEG > PVK, consistent with the magnitude and accessibility of the negative partial charge on their coordinating functional groups. The sterically accessible carbonyl group in PVA provided the strongest interaction with the undercoordinated Pb species associated with V_I, whereas the weaker or more delocalized electron density in PEG and PVK resulted in progressively weaker interactions.

To confirm the interaction between the corresponding Lewis base functional groups of the polymers and the Lewis acid lead ions, we applied Fourier transform infrared spectroscopy (FTIR)

to investigate the C=O stretch in PVA, C–O stretch in PEG, and carbazole vibration in PVK (**Figure 2.1**). FTIR measurements experimentally confirmed the predicted interaction trend. The C=O stretching vibration of PVA shifted from 1722 to 1698 cm^{-1}after interaction with PbI_2, substantially larger than the shifts observed for PEG and PVK (5 and 2 cm^{-1}, respectively). The pronounced shift for PVA is consistent with stronger Lewis acid–base interaction between its carbonyl group and undercoordinated Pb species. The much more pronounced peak shift for PVA than those for other polymers supports the stronger interaction energy between the PVA and undercoordinated Pb^{2+} (V_I) owing to the sterically accessible Lewis base C=O functional group with more negative partial charges, consistent with the predications from computer simulations.

The strength of the interaction was further confirmed by X-ray photoelectron spectroscopy (XPS) analysis. **Figure 2.2A** shows the XPS spectra of the Pb *4f* orbitals measured from the perovskite films without and with surface post-treatment by PVA, PEG, and PVK (all at the concentration of 0.05 mg/mL). Consistently, Pb *4f* XPS peaks shifted toward lower binding energy after polymer treatment, with the largest shift observed for PVA, indicating increased electron density around Pb through polymer–perovskite interaction. Together, the DFT, FTIR, and XPS results establish the interaction-strength sequence PVA > PEG > PVK.

The X-ray diffraction (XRD) patterns of the perovskite films without and with the three polymer treatments are shown in **Figure 2.2B**. The intensities and full-width-half-maximums (FWHMs) of the (001) and (002) orientation peaks of the polymer-treated perovskite film were comparable with those of the peaks of the control perovskite film, indicating that the post-heat-treatment introduction of the polymer layer had a negligible effect on the crystallinity of the underlying perovskite film. The top-view scanning electron microscopic (SEM) images of the perovskite films without and with polymer treatments are shown in **Figures 2.2C**–**F**. Compared

with the control film (without any polymer treatment), the grain size of polymer-modified perovskite films almost remained unchanged. The larger (5×4 μm^2) SEM images and the corresponding statistical distribution of grains are shown in **Figure B2.3**. The average grain size of both control and polymer-treated films was 370 nm. The conductive AFM (c-AFM) was performed, and the results are shown in **Figures 2.2G–J** to observe the spatially resolved electrical properties of these perovskite films. The average current was 175, 1520, 879, and 323 pA for control, PVA-treated, PEG-treated, and PVK-treated perovskite films, respectively. Clearly, the current was higher but inhomogeneous in the films with the polymer post-treatment, whereas relatively uniform and lower current was observed in the control film, which indicates that the local charge collection efficiency of photo-generated carriers was facilitated for the polymer post-treatment samples. Meanwhile, the Kelvin probe force microscopy (KPFM) measurement was performed as shown in **Figure B2.4** to investigate changes in surface potential induced by the polymers. Compared with the control film, the contact potential difference (CPD) at the grain boundary region increases significantly for the films modified by polymers (100 mV). This indicates that the polymeric passivator mainly exists at the low-lying grain boundary region and passivates the defects at the grain boundaries. The CPD at grain interior region remains unchanged or slightly changed, indicating that surface-energy-level alignment in this region is not affected by the polymer coating.

2.3 Polymer-Induced Defect Passivation and Carrier Dynamics

To investigate the impact of the deposited polymers on carrier dynamics, we first examined the steady-state absorption and photoluminescence (PL) spectra of the perovskite films with and without polymer deposition (**Figure 2.3A**). The absorption spectra were almost identical for all perovskite films, indicating no significant contribution of the polymer layer to the absorption in

the visible wavelength region. In contrast, the steady-state PL intensity was significantly enhanced for the films with the polymer treatment, by 10.4 (PVA), 4.2 (PEG), and 2.8 (PVK) times higher than that of the control film. This result was consistent with the trap-state passivation effect of polymers. We then investigated carrier dynamics over a broad timescale from fs to μs through both the ultrafast transient absorption (TA) spectroscopy (**Figure B2.5**) and the time-resolved PL (TRPL) technique. **Figure 2.3B** shows the recovery kinetics of transient bleaching signal probed at 795 nm in TA spectra of perovskite films without and with the three polymeric modification layers (pump wavelength was 370 nm). The TA bleaching signal at 795 nm originates from the band-edge state filling by photo-excited charge carriers[13,14]. Its recovery kinetic can then reflect the carrier depopulation process. For all the examined samples, their TA kinetics did not exhibit any ultrafast decay process within the <1 ns window, indicating that the deposition of PVA, PEG, and PVK did not introduce any fast decay pathways to the carriers in perovskites. However, compared with the control sample, the TA decays became slower in the ns time window for the films with the polymer post-treatment. This trend can be further confirmed by the TRPL decays collected in the ns-to-μs time windows (as seen in **Figure 2.3C**). To quantitatively determine the photo-excited carrier lifetimes, the TRPL decays in **Figure 2.3C** were fitted by a bi-exponential decay function and the resulting parameters are summarized in **Table C2.1**. The averaged PL lifetimes were calculated to be 139.3, 877.2, 556.5, and 382.4 ns for the control film and PVA-, PEG-, and PVK-treated films, respectively. The carrier lifetimes in polymer-treated perovskite films became much longer than that in the control sample. Most importantly, among the three examined polymers, PVA was found to introduce the most prominent trap passivation effect in perovskites. This result is consistent with the predictions from DFT calculations.

To examine the PL homogeneity of perovskite films before and after the polymer deposition, the PL intensity and lifetime images with a sub-micrometer spatial resolution were taken using a laser-scanned and time-resolved imaging microscopy. **Figures 2.3D–G** show the PL intensity images of perovskite films with and without polymer depositions, and their corresponding PL lifetime images are shown in **Figures 2.3H–K**. Prominent improvements in both PL intensity and homogeneity (in micrometer scale) were observed in the films with polymer depositions. The results in PL lifetime images (**Figures 2.3H–K**) further confirmed the polymer-induced improvement of PL property by displaying longer local PL lifetimes and more homogeneous lifetime distribution.

Collectively, these results demonstrate that polymer treatment, particularly PVA, effectively suppresses non-radiative recombination and improves the photophysical quality of the perovskite films. The comparison between three different polymers also provides an important insight into the design of an effective polymer with specific molecular structure that regulates and optimizes the perovskite photophysical properties.

2.4 Photovoltaic Performance and Interfacial Charge Transport

Finally, we examined the effect of polymer treatment in practical PSCs. The complete device structure is ITO/SnO_2/perovskite/polymer/spiro-MeOTAD/Au. Here, the interface between the perovskite active layer and HTL is the focus of our investigation and is thus marked with a red dotted box. In the control device, regions of uneven morphology and interfacial gaps were observed. Compared with the control device, the interface contacts between perovskite and HTL improved significantly for the polymer-treated devices, especially with the post-treatment by PVA. This observation indicates that the polymer post-treatment can improve the interface contact, which may contribute to facilitating the carrier extraction from the perovskite layer. The current

density-voltage (*J-V*) curves and corresponding photovoltaic performance parameters of the champion PSCs with and without the polymer treatment process are compared in **Figure 2.4A** and **Table C2.2**. The control device had a J_{sc} of 23.28 mA cm^{-2}, V_{oc} of 1.120 V, FF of 78.5%, and a resulting PCE of 20.47% in the reverse scan. In comparison, the perovskite film treated by 0.05 mg/mL PVA solution had all the photovoltaic parameters increased, achieving a J_{sc} of 25.24 mA cm^{-2}, V_{oc} of 1.149 V, FF of 80.0%, and a resulted PCE of 23.20% in the reverse scan. The champion PCEs of the devices with PEG- and PVK-modified layers were 22.35% and 21.97%, respectively, which were both higher than that of the control devices. Therefore, we confirmed that all three polymers improved device performance, and the best improvement was achieved by PVA. **Figure 2.4B** displays the external quantum efficiency (EQE) spectra of the corresponding devices. The integrated J_{sc} values were calculated to be 23.20, 24.59, 23.64, and 23.52 mA cm^{-2} for control, PVA-, PEG-, and PVK-treated devices, respectively. These values were reasonably consistent with the average J_{sc} values obtained from the *J-V* measurements, with less than 5% discrepancy. The time-dependent photocurrent output at a fixed bias voltage was measured and is shown in **Figure 2.4C**, with the stabilized PCEs of 20.08%, 22.92%, 21.69%, and 21.26% for the control, PVA, PEG, and PVK treatment, respectively, which were also consistent with the PCEs obtained from the *J-V* measurements.

The transient photocurrent (TPC) and transient photovoltage (TPV) decay process were applied to study the charge-carrier behavior in the PSCs as shown in **Figures 2.4D** and **B2.6**. The TPC and TPV data were fitted with a single-exponential decay model to get the time constants for charge collection (τ_C) and charge recombination (τ_R) (**Figure B2.6**). The τ_C values for the control, PVA, PEG, and PVK were 4.75, 1.82, 2.07, and 2.34 μs, respectively, indicating a facilitated charge collection process in the PVA-treated device. The introduction of PVA might improve the

interfacial contact between the perovskite and HTL to promote the extraction of photo-excited carriers. The τ_{RS}s were 0.14, 0.30, 0.20, and 0.16 ms for the control, PVA-, PEG-, and PVK-treated devices, respectively, which are in accord with the trend observed in the PL intensity and lifetime measurements. The largest τ_R for the sample treated by PVA indicates that the recombination of electron and hole pairs can be most effectively mitigated by the PVA post-treatment. Based on the above analysis, it can be deduced that the density of defect states at the interface was greatly reduced via PVA post-treatment to facilitate the extraction of photo-excited hole carriers to the HTL layer. Thus, we attributed the improved photocurrent to (1) improved charge-carrier diffusion lengths in the perovskite layer due to reduced defect states, (2) the improved interfacial contact to promote the charge transfer from the perovskite layer to spiro-MeOTAD layer. Both factors should contribute to charge collection efficiency of the PSCs and thus photocurrent of the device[15,16]. Electrochemical impedance spectroscopy (EIS) is a powerful method to analyze the characteristics of heterointerfaces of perovskite devices. Here, the Nyquist plots by the EIS measurement are shown in **Figure 2.4E**. Using a modified Randles equivalent circuit, the radii of the semicircles can be assigned to a combination of the charge transport resistance (R_{ct}) and recombination resistance (R_{rec}) [17,18,19]. In comparison with that of the control device, the R_{ct} (the semicircle with relatively smaller radius) decreased significantly, but the R_{rec} (the semicircle with relatively larger radius) increased in the case of the PVA treatment. The observed trend exhibited by R_{ct} and R_{rec} correlates well with the TPV and photocurrent decay measurements. Thus, it can be speculated that an appropriately thin PVA-modified layer could effectively prevent interfacial charge recombination while improving the interfacial contact, and in turn facilitate the extraction of photo-generated carrier from perovskite layer. The Mott-Schottky plots of devices were further investigated, as shown in **Figure 2.4F**. The built-in potentials of the devices were 1.033, 1.093,

1.072, and 1.065 V for devices without and with polymer post-treatment by control and PVA, PEG, and PVK, respectively, which correlated with the V_{OC} measured from the devices. The trap density (N_t) of each device was estimated by using admittance spectroscopy measurement (**Figures 2.4G**) [20]. The N_t was lower for the polymer post-treatment devices (PVA < PEG < PVK < control), and the trend corresponded well with the TA, steady-state PL intensity, average PL lifetime, the τ_R, and interfacial contact, indicating that the polymer post-treatment by PVA, PEG, and PVK reduced the surface and/or interfacial defect density and enhanced the device performance. Furthermore, the space-charge-limited-current (SCLC) technique was utilized to cross-check the defect density in the perovskite films treated by different passivating agents, as shown in **Figures 2.4H** and **2.4I**. The device with a structure of ITO/perovskite/polymer/Au was fabricated and is shown in the inset of **Figure 2.4I**. The N_t can be calculated from the equation:

$$V_{TFL} = \frac{eN_t d^2}{2\varepsilon\varepsilon_0} \qquad \text{Equation (1)}$$

where e is the elementary charge, d is the perovskite film thickness, ε is the relative dielectric constant, ε_0 is the vacuum permittivity, and V_{TFL} is the trap-filling voltage. The perovskite film treated by PVA had the lowest defect density of 4.61×10^{15} cm^{-3}, which was significantly lower than that of the control sample (1.01×10^{16} cm^{-3}) and lower than those of PEG-treated films (5.19×10^{15} cm^{-3}) and PVK-treated films (5.44×10^{15} cm^{-3}). Additionally, dark *J-V* curves of the devices are presented in **Figure B2.7**. The series resistance (R_s), shunt resistance (R_{sh}), saturation current (J_0), and ideality factor (n) calculated from dark *J-V* curves are summarized in **Table C2.3**[21]. Compared with the control device, the reduced R_s and increased R_{sh} obtained in PVA-treated devices are consistent with the TPV and TPC measurements. The lower J_0 and n values also indicate the reduced interfacial recombination and improved interfacial contact between the perovskite and HTL.

2.5 Operational Stability of Polymer-Passivated Devices

To investigate the effects of different polymeric passivating agents on the operational stability of the solar cell devices, we exposed the encapsulated devices to continuous illumination under open-circuit conditions (**Figure 2.5A**). Ion migration can be particularly pronounced under open-circuit conditions because of the relatively high carrier concentration. After 1,600 h of exposure, the control device almost completely degraded, whereas the encapsulated device incorporated with PVA maintained 79.6% of its initial PCE. The devices incorporated with PEG and PVK retained 55.5% and 42.8% of the initial PCEs, respectively. To further evaluate the thermal stability of the devices, we kept the unencapsulated devices in a nitrogen-filled glove box at 85 °C (**Figure 2.5B**). The poly(triaryl amine) (PTAA) was used as the hole-transporting layer instead of spiro-MeOTAD owing to its poor thermal stability. After 1,600 h, we observed that the device incorporated with PVA maintained the highest PCE (retaining 72.8% of its initial PCE) relative to the other devices. The control, PEG-, and PVK-incorporated devices retained 0%, 58.2%, and 48.3% of their initial PCEs, respectively. Finally, the change of PCE for unencapsulated devices under dark conditions was investigated as shown in **Figure 2.5C**. All devices with polymeric surface modification maintained higher PCE than that of control device for 1,600 h. After 1,600 h, the control device and the devices with PVA, PEG, and PVK modifications maintained 33.3%, 98.7%, 84.3%, and 73.9% of their initial efficiency, respectively. The stability trend further supports the importance of strong and sterically accessible Lewis-base interactions in stabilizing interfacial defects during prolonged stress. Stronger coordination may reduce the mobility of charged defects and thereby contribute to improved stability under prolonged stress.

References

1 Xu, N. et al. Point defects in metal halide perovskites. *Nature Reviews Physics* 7, 554–564 (2025).

2 Kim, J. et al. The role of intrinsic defects in methylammonium lead iodide perovskite. The *Journal of Physical Chemistry Letters* **5**, 1312–1317 (2014).

3 Yin, W.-J. et al. Point defects and potential passivation strategies in lead halide perovskites. *Advanced Materials* **30**, 1703159 (2018).

4 Meggiolaro, D. et al. Iodine vacancies in lead halide perovskites: formation, migration, and impact on photovoltaic performance. *Energy & Environmental Science* **12**, 2737–2749 (2019).

5 Ball, J. M. & Petrozza, A. Defects in perovskite-halides and their effects in solar cells. *Nature Energy* **1**, 16149 (2016).

6 Chen, J. & Park, N.-G. Materials and methods for interface engineering toward stable and efficient perovskite solar cells. *ACS Energy Letters* **5**, 2742–2785 (2020).

7 Wang, R. et al. Constructive molecular configurations for surface-defect passivation of perovskite photovoltaics. *Science* **366**, 1509–1513 (2019).

8 Zhao, Y. et al. A polymerization-assisted grain growth strategy for efficient and stable perovskite solar cells. *Advanced Materials* **32**, e1907769 (2020).

9 Han, T. H. et al. Perovskite-polymer composite cross-linker approach for highly stable and efficient perovskite solar cells. *Nature Communications* **10**, 520 (2019).

10 Walsh, A. et al. Self-regulation mechanism for charged point defects in hybrid halide perovskites. *Angewandte Chemie* **127**, 1811–1814 (2015).

11 Tan, S. et al. Shallow iodine defects accelerate the degradation of α-phase formamidinium perovskite. *Joule* **4**, 2426–2442 (2020).

12 Zhao, Y. et al. Molecular interaction regulates the performance and longevity of defect passivation for metal halide perovskite solar cells. *Journal of the American Chemical Society* **142**, 20071–20079 (2020).

13 Wu, K. et al. Ultrafast interfacial electron and hole transfer from $CsPbBr_3$ perovskite quantum dots. *Journal of the American Chemical Society* **137**, 12792–12795 (2015).

14 Yin, Z. et al. Auger-assisted electron transfer between adjacent quantum wells in two-dimensional layered perovskites. *Journal of the American Chemical Society* **143**, 4725–4731 (2021).

15 Chen, W. et al. Improved charge extraction beyond diffusion length by layer-by-layer multistacking intercalation of graphene layers inside quantum dot films. *Advanced Materials* **31**, e1807894 (2019).

16 Wu, F. et al. Dynamic characterization of hybrid solar cells based on polymer and aligned ZnO nanorods by intensity-modulated photocurrent spectroscopy. *The Journal of Physical Chemistry C* **114**, 20225–20235 (2010).

17 Wang, M. et al. Stable and efficient methylammonium-, cesium-, and bromide-free perovskite solar cells by in situ interlayer formation. *Advanced Functional Materials* **31**, 2007520 (2021).

18 Jung, K.-H. et al. Solution-processed SnO_2 thin film for a hysteresis-free planar perovskite solar cell with a power conversion efficiency of 19.2%. *Journal of Materials Chemistry A* **5**, 24790–24803 (2017).

19 Jiang, X. et al. Molecular engineering of copper phthalocyanines: a strategy in developing dopant-free hole-transporting materials for efficient and ambient-stable perovskite solar cells. *Advanced Energy Materials* **9**, 1803287 (2019).

20 Lee, J.-W. et al. A bifunctional Lewis base additive for microscopic homogeneity in perovskite solar cells. *Chem* **3**, 290–302 (2017).

21 Lee, J.-W. et al. Tuning molecular interactions for highly reproducible and efficient formamidinium perovskite solar cells via adduct approach. *Journal of the American Chemical Society* **140**, 6317–6324 (2018).

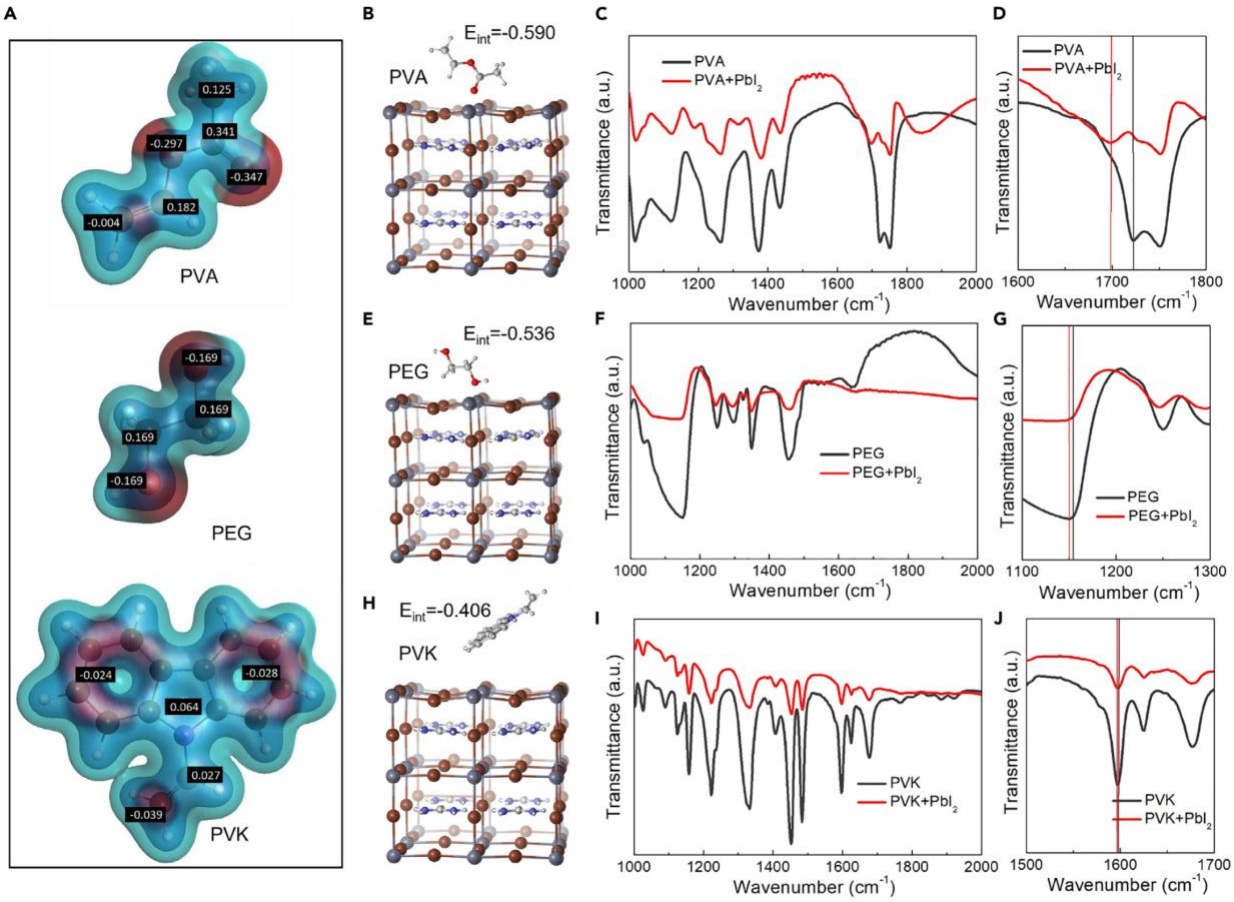

Figure 2.1 Interaction simulation and confirmation. (A) Partial charge distribution of three kinds of monomers determined by density functional theory (DFT) calculation. (B–J) Theoretical models of the monomers interacting with surface iodide vacancy (V_I) defect of perovskite crystals and the corresponding interaction energies (E_{int}): monomers of (B) poly(vinyl acetate) (PVA), (E) polyethylene glycol (PEG), and (H) poly(9-vinylcarbazole) (PVK). Fourier transform infrared spectroscopy (FTIR) spectra of (C and D) pure PVA and PVA-PbI_2 films, (F and G) pure PEG and PEG-PbI_2 films, and (I and J) PVK and PVK PbI_2 films.

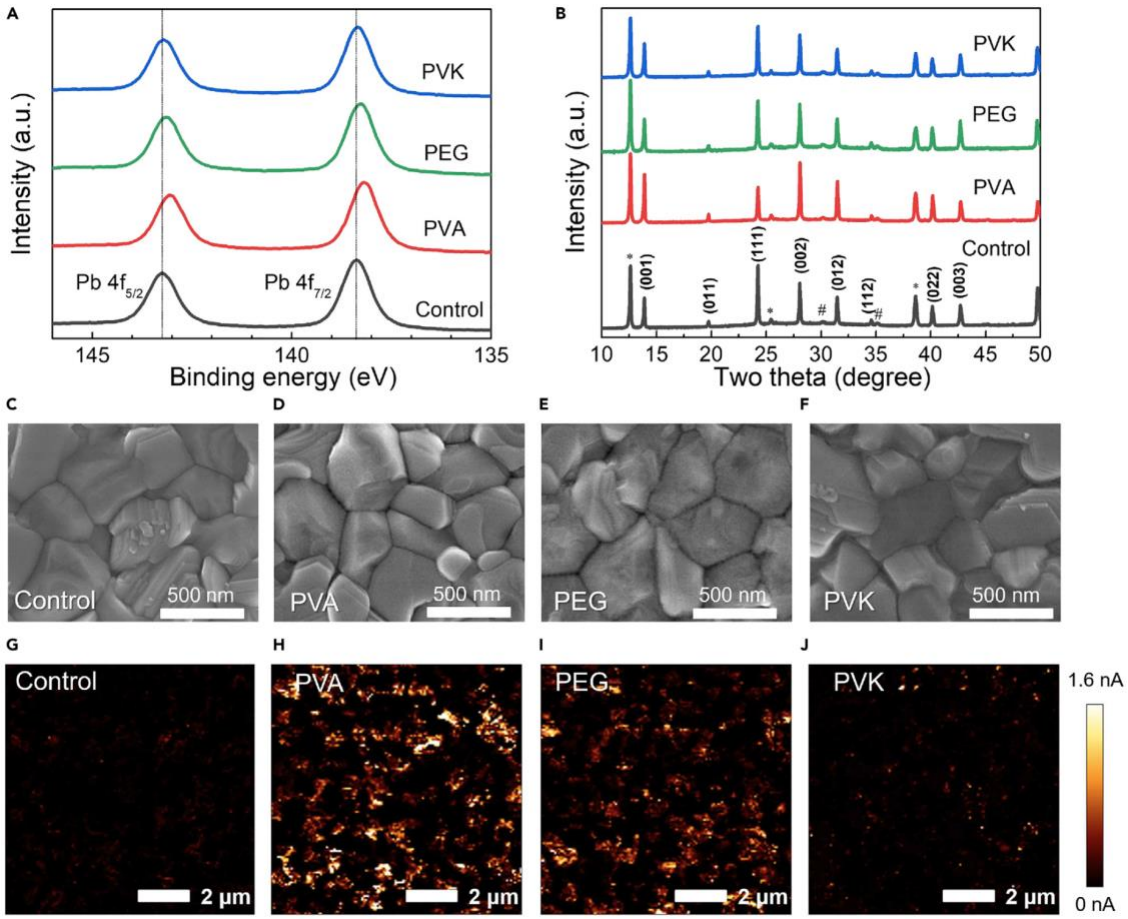

Figure 2.2 Characterizations of film surface changes with different treatments. (A and B) (A) XPS spectra of Pb 4f peaks of the perovskite films without and with polymer modification layer and (B) corresponding X-ray diffraction (XRD) patterns. (C–J) Scanning electron microscopy (SEM) images and conductive atomic force microscopic (c-AFM) images of the perovskite films (C and G) without and with surface treatment using (D and H) PVA, (E and I) PEG, and (F and J) PVK. The perovskite films were prepared on SnO_2-coated ITO glass. The c-AFM measurement was carried out with a bias voltage of 100 mV under room light.

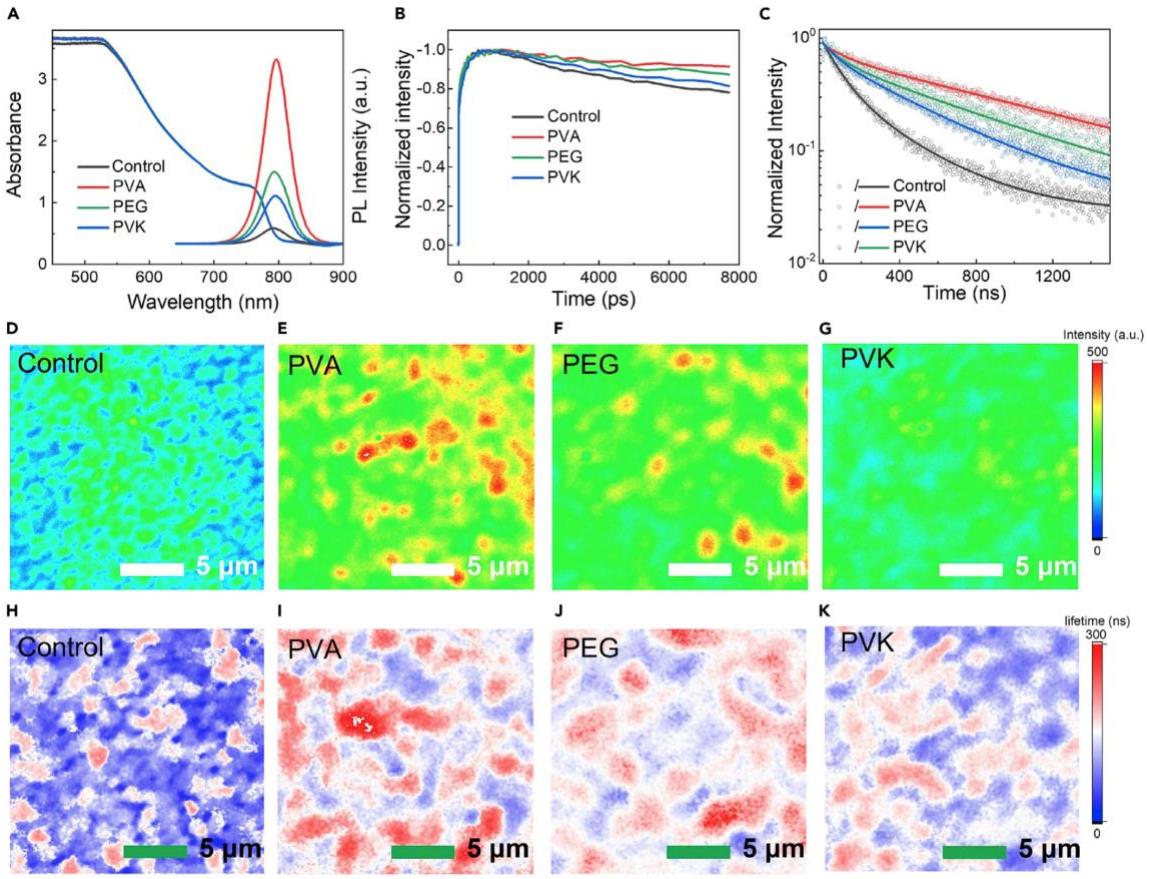

Figure 2.3 Carrier lifetime differences of the films with different treatments. (A–K) (A) Absorption and steady-state photoluminescence (PL) spectra, (B) transient absorption (TA) decay curves, (C) time-resolved PL decay, and two-dimensional PL intensity and PL lifetime images of the perovskite films without (D and H) and with polymer modification layers of PVA (E and I), PEG (F and J), and PVK (G and K). The empty circles indicate the measured data, and solid lines indicate the fitted curves in (C).

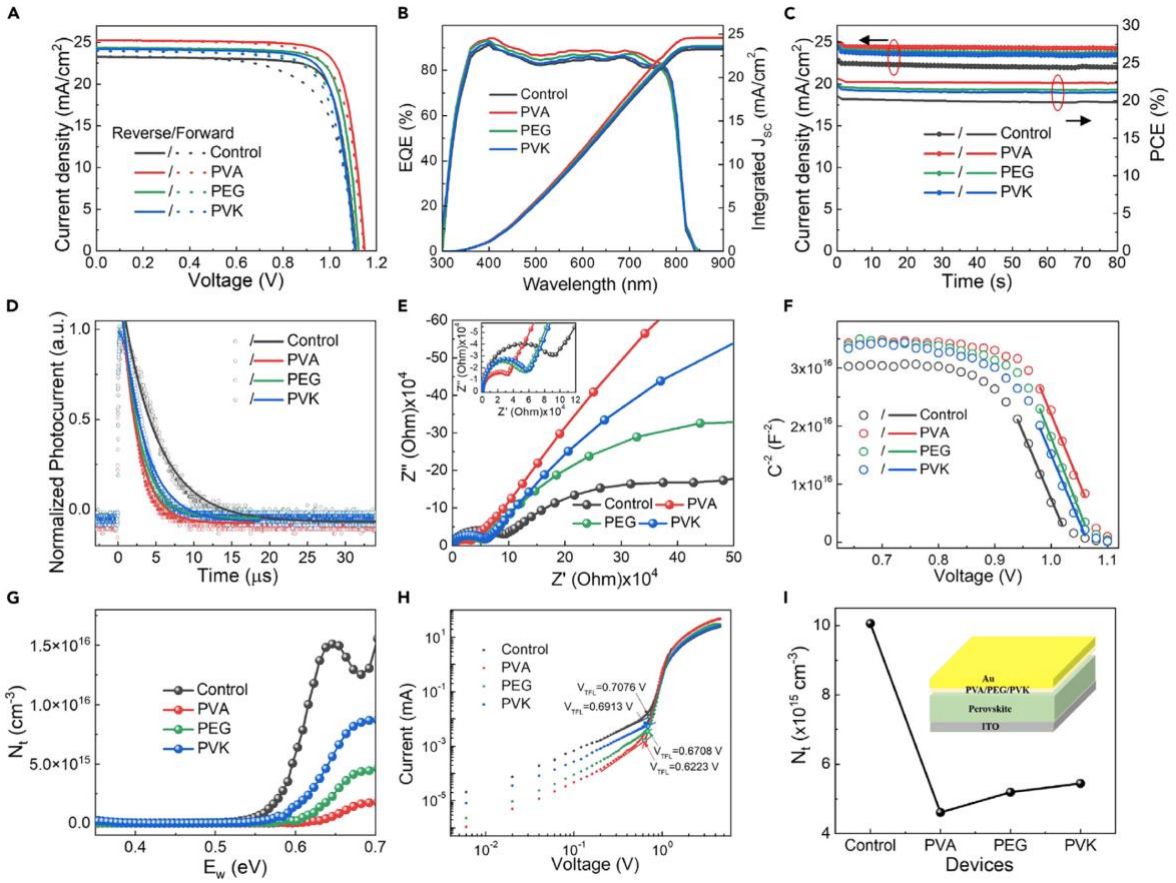

Figure 2.4 Device characterization. (A) Current density-voltage (J-V) curves of the PSCs without and with polymer post-treatment by PVA, PEG, and PVK. Solid and dotted lines are data obtained by reverse and forward scans, respectively. (B) The external quantum efficiency (EQE) spectra and corresponding integrated short-circuit current density (J_{sc}) of the PSCs. (C) Time-dependent power output measurements to monitor the stabilized power conversion efficiencies (PCEs) at constant bias voltage. (D–G) (D) Transient photocurrent (TPC) decay, (E) The Nyquist plots, (F) Mott-Schottky plots, (G) calculated trap density of the corresponding PSCs without and with polymer post-treatment by PVA, PEG, and PVK. (H and I) (H) Space-charge-limited-current (SCLC) measurements and (I) defect density calculated from SCLC measurements without and with polymer post-treatment. V_{TFL} is the trap-filling voltage. The empty circles indicate the measured data, and the solid lines indicate the fitted curves in (D) and (F).

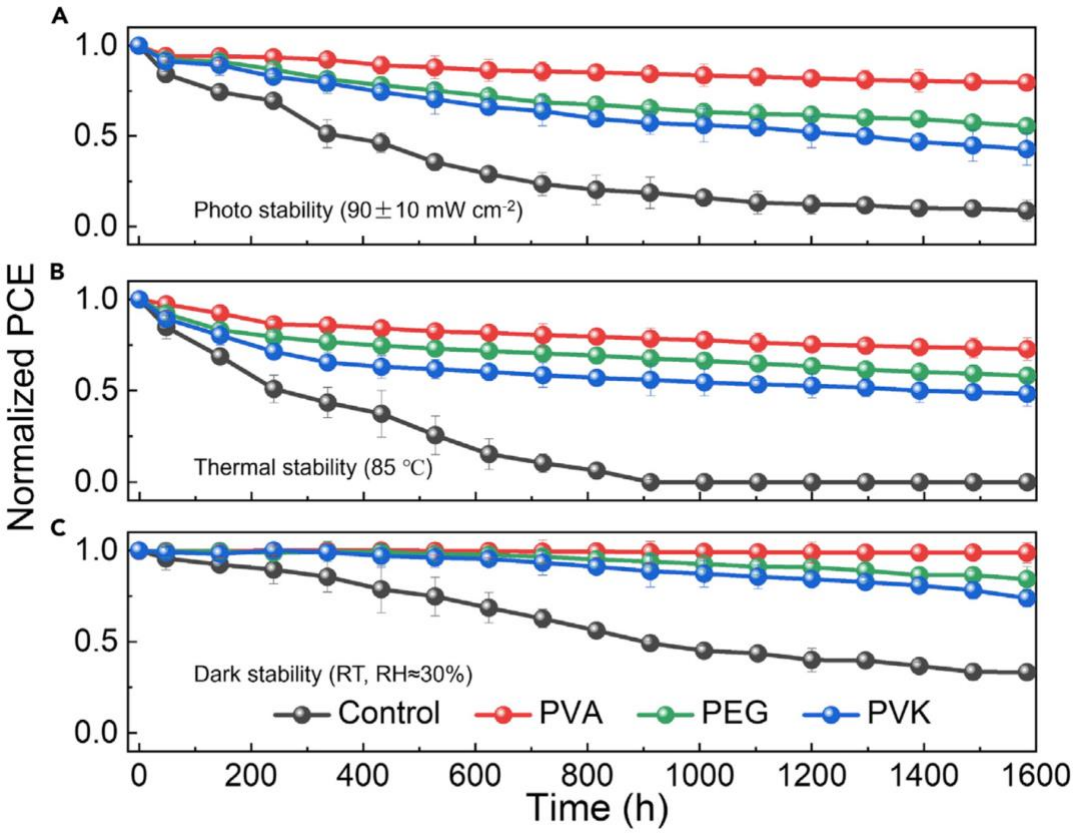

Figure 2.5 Stability tests. (A–C) The change of PCEs of the PSCs without and with polymer post-treatment by PVA, PEG, and PVK (A) under continuous illumination (90 ± 10 mW cm^2), (B) thermal stress (85 °C, under dark and nitrogen atmosphere), and (C) dark conditions without encapsulation.

Chapter 3 From Top Interface to Buried Interface

3.1 Why investigate the buried interface

The results presented in Chapter 2 demonstrate that molecularly designed polymeric modifiers can effectively passivate electronically active defects at the exposed perovskite surface. Lewis-basic functional groups with favorable electronic characteristics and sufficient steric accessibility can interact with undercoordinated species, suppress non-radiative recombination, and improve the photovoltaic performance of perovskite solar cells. Nevertheless, the exposed surface represents only one of the critical interfaces in a complete device[1]. In a typical n–i–p architecture, the perovskite absorber is deposited directly onto an electron-transport layer (ETL), forming a buried interface that becomes physically concealed after completion of the absorber layer. Understanding and engineering this region therefore represents an important extension beyond conventional surface passivation.

The buried interface occupies a distinct position within the device architecture and participates in both the formation and operation of the perovskite absorber. Unlike post-treatment of the exposed surface, any modification introduced at the buried interface is present before perovskite deposition and therefore constitutes the underlying surface on which the absorber is formed[2]. The buried region can consequently influence the initial formation of the perovskite film, while simultaneously serving as the heterointerface through which photogenerated electrons are extracted during device operation. The consequences of this buried-interface environment for perovskite formation are discussed in detail in Section 3.3.

The optical environment near the buried interface also differs from that at the exposed surface. In conventional n–i–p devices, illumination enters through the transparent substrate and

ETL before reaching the perovskite absorber (**Figure 3.1A and Figure B3.1**). The depth-dependent optical intensity can be described approximately by the Beer–Lambert relationship:

$$I(x) = I_0 e^{-\alpha x} \qquad \text{Equation (2)}$$

where I_0 is the incident light intensity, α is the absorption coefficient, and x is the penetration depth, the optical intensity decreases progressively through the absorber. Because metal-halide perovskites possess high absorption coefficients across much of the visible spectrum (**Figure 3.1B**), a substantial fraction of ultraviolet photons can be absorbed within a relatively short distance from the illuminated side of the absorber (**Figure 3.1C**)[3]. Consequently, photocarrier generation is not necessarily uniform throughout the film thickness. This asymmetric excitation profile does not by itself imply that degradation must be more severe at the buried interface; however, it provides additional motivation to examine whether different regions of the absorber undergo comparable chemical and structural evolution during prolonged operation.

Depth-resolved chemical characterization indicates that such evolution can indeed be spatially nonuniform (**Figure 3.2**). Comparison of fresh and operation-aged devices reveals relatively limited compositional changes near the exposed perovskite surface, whereas more pronounced changes emerge toward the buried region. In particular, the compositional transition across the SnO_2/perovskite boundary becomes broader after operation, accompanied by changes in the distribution of Sn-related species and perovskite-related elements (Pb, I and N) near the bottom of the absorber. These observations indicate that the buried interface undergoes substantial chemical evolution during device operation. Importantly, the depth-resolved measurements alone do not establish the buried interface as the sole origin of device degradation, nor do they identify a complete degradation mechanism. Instead, they demonstrate that this region evolves differently from the exposed surface and therefore warrants further mechanistic investigation.

The buried interface is also experimentally more difficult to access[4]. Conventional surface-sensitive characterization techniques, such as atomic force microscopy, photoelectron spectroscopy, and surface optical measurements, can readily probe the exposed perovskite surface. Once the absorber is deposited, however, the bottom interface becomes physically concealed beneath the perovskite layer. Investigating this region therefore often requires specialized approaches, including mechanical delamination, depth profiling, and cross-sectional microscopy. This limited accessibility has made buried-interface processes less straightforward to characterize, despite the direct involvement of this region in charge extraction, absorber formation, and long-term device operation.

Taken together, the buried interface represents a distinct interfacial problem because of its unique position within the device architecture, its involvement in absorber formation, its spatially distinct chemical evolution during operation, and its limited experimental accessibility. These characteristics motivate two complementary questions. First, how do ionic and chemical species redistribute across the buried interface during device operation, and how do these dynamic processes affect long-term stability? Second, how does the chemical and physical nature of the buried interface influence perovskite formation before operation begins? These two aspects are introduced in Sections 3.2 and 3.3 and form the basis of the studies presented in Chapters 4 and 5, respectively.

3.2 Buried Interfaces as Dynamic Ionic Boundaries

Metal halide perovskites are mixed ionic–electronic conductors in which mobile ionic defects can redistribute under illumination, electrical bias, and thermal activation. Ion migration is enabled by the presence of mobile defects and relatively low migration barriers within the soft perovskite lattice. Interfaces are particularly important because they represent chemically and

structurally heterogeneous boundaries, where local electric fields, defect distributions, strain, and chemical-potential gradients can modify the thermodynamic and kinetic landscape for ionic redistribution[5].

Ion accumulation at an interface can substantially alter the local properties of a device. Redistribution of charged ionic species can modify electrostatic potentials and band bending, influence defect populations, and alter carrier extraction and recombination[6]. Over extended periods of operation, ionic redistribution may also facilitate chemical reactions between the perovskite and adjacent functional layers. The electronic and ionic properties of an interface are therefore coupled: an interface that initially exhibits favorable electronic characteristics may gradually evolve as mobile species accumulate or redistribute during operation.

Importantly, ionic evolution at a buried interface is not necessarily limited to species originating within the perovskite absorber. A perovskite solar cell consists of chemically dissimilar functional layers in direct contact, and species from adjacent layers may also participate in interfacial transport under operational stress[7,8]. Cross-interface transport therefore extends the conventional picture of ion migration beyond redistribution within the perovskite lattice itself. In this context, the buried interface can serve not only as a region of ionic accumulation but also as a transport boundary across which atomic or ionic species redistribute between adjacent materials.

This behavior introduces an important design requirement for buried-interface engineering: detrimental ionic transport should be suppressed without compromising electronic charge extraction. Ionic migration generally requires physical displacement of atoms or defects across migration barriers, whereas electronic transport depends primarily on electronic coupling, energetic alignment, and transport distance. These processes can therefore, in principle, be regulated independently. An appropriately designed interlayer may increase the energetic barrier

for ionic motion while maintaining sufficiently favorable electronic transport across the interface. In contrast, a thick or electronically resistive barrier may suppress ionic transport at the expense of increased interfacial resistance, reduced charge extraction, and losses in fill factor or photocurrent. Effective buried-interface engineering must therefore balance ionic blocking capability with efficient electronic transport[9].

These considerations raise several fundamental questions. Which species migrate across the buried interface during operation? What chemical and structural features determine their migration barriers? How does cross-interface transport influence the chemical stability of the perovskite absorber? Most importantly, can an interfacial material selectively suppress detrimental ionic motion while retaining efficient electronic charge transport? These questions form the basis of the investigation presented in Chapter 4.

3.3 Buried Interfaces as Templates for Perovskite Formation

While the buried interface remains a dynamic boundary during device operation, its influence begins much earlier, during formation of the perovskite absorber. Unlike post-treatment of the exposed surface, buried-interface modification is introduced before perovskite crystallization. The underlying surface can therefore influence precursor wetting, heterogeneous nucleation, and subsequent crystal growth[2,10,11].

The initial interaction between the precursor and the underlying substrate is governed by both surface energetics and chemical affinity. Appropriate wetting is important for uniform precursor coverage, while interfacial interactions can alter precursor coordination and modify the energetic landscape and kinetics of heterogeneous nucleation. Therefore, changing the chemistry of the buried interface can affect the density and spatial distribution of nuclei formed during the early stages of film formation.

These early nucleation processes subsequently influence crystal growth and the final microstructure of the absorber. Changes in nucleation and interfacial interactions can affect grain morphology, crystallinity, phase formation, interfacial contact, and defect formation. Because these processes originate at the substrate/perovskite boundary, their influence can propagate beyond the immediate interface and affect the structural and electronic quality of the overlying perovskite film.

Buried-interface engineering therefore offers an opportunity to regulate perovskite quality during film formation rather than only passivating defects after crystallization. At the same time, the buried interface remains susceptible to ionic and chemical evolution during device operation. These two complementary roles—regulation of perovskite formation and control of dynamic interfacial processes—form the basis of Chapters 4 and 5.

References

1 Yang, Y. et al. Top and bottom surfaces limit carrier lifetime in lead iodide perovskite films. *Nature Energy* **2**, 16207 (2017).

2 Bi, D. et al. Polymer-templated nucleation and crystal growth of perovskite films for solar cells with efficiency greater than 21%. *Nature Energy* **1**, 16142 (2016).

3 De Wolf, S. et al. Organometallic halide perovskites: sharp optical absorption edge and its relation to photovoltaic performance. *Journal of Physical Chemistry Letters* **5**, 1035–1039 (2014).

4 Pu, Y. et al. A review on buried interface of perovskite solar cells. *Energies* **16**, 5015 (2023).

5 Eames, C. et al. Ionic transport in hybrid lead iodide perovskite solar cells. *Nature Communications* **6**, 7497 (2015).

6 Kress, J. A. et al. Persistent ion accumulation at interfaces improves the performance of perovskite solar cells. *ACS Energy Letters* **7**, 3302–3310 (2022).

7 Choi, S.-G. & Lee, J.-W. Irreversible phase back conversion of α-$FAPbI_3$ driven by lithium-ion migration in perovskite solar cells. *EcoMat* **5**, e12398 (2023).

8 Shen, L. et al. Ultrathin polymer membrane for improved hole extraction and ion blocking in perovskite solar cells. *Nature Communications* **15**, 10908 (2024).

9 Zai, H., Ma, Y., Chen, Q. & Zhou, H. Ion migration in halide perovskite solar cells: mechanism, characterization, impact and suppression. *Journal of Energy Chemistry* **63**, 528–549 (2021).

10 Bi, C. et al. Non-wetting surface-driven high-aspect-ratio crystalline grain growth for efficient hybrid perovskite solar cells. *Nature Communications* **6**, 7747 (2015).

11 Luo, C. et al. Engineering the buried interface in perovskite solar cells via lattice-matched electron transport layer. *Nature Photonics* **17**, 856–864 (2023).

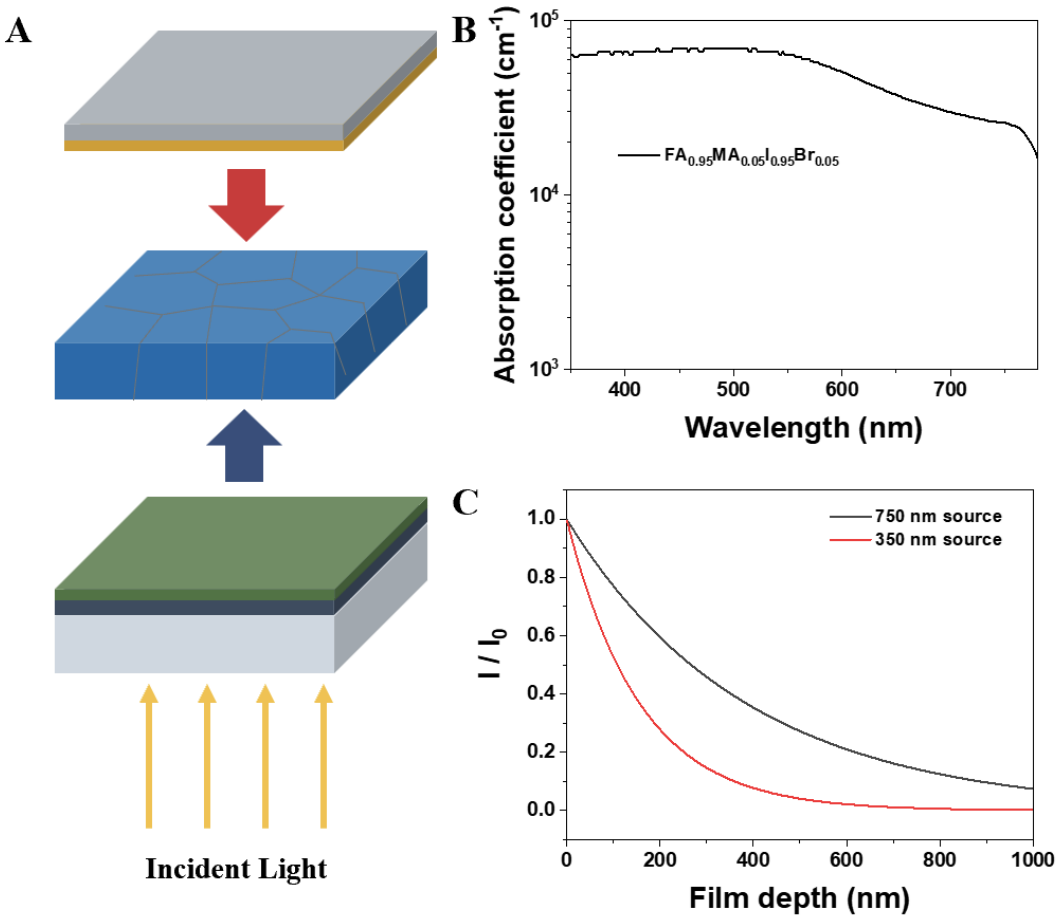

Figure 3.1 Asymmetric light absorption across the perovskite layer under substrate-side illumination. (A) Schematic illustration of light incident from the substrate side of a perovskite solar cell. (B) Wavelength-dependent absorption coefficient of the perovskite absorber. (C) Calculated normalized light intensity as a function of film depth for incident wavelengths of 350 and 750 nm based on the Beer–Lambert law.

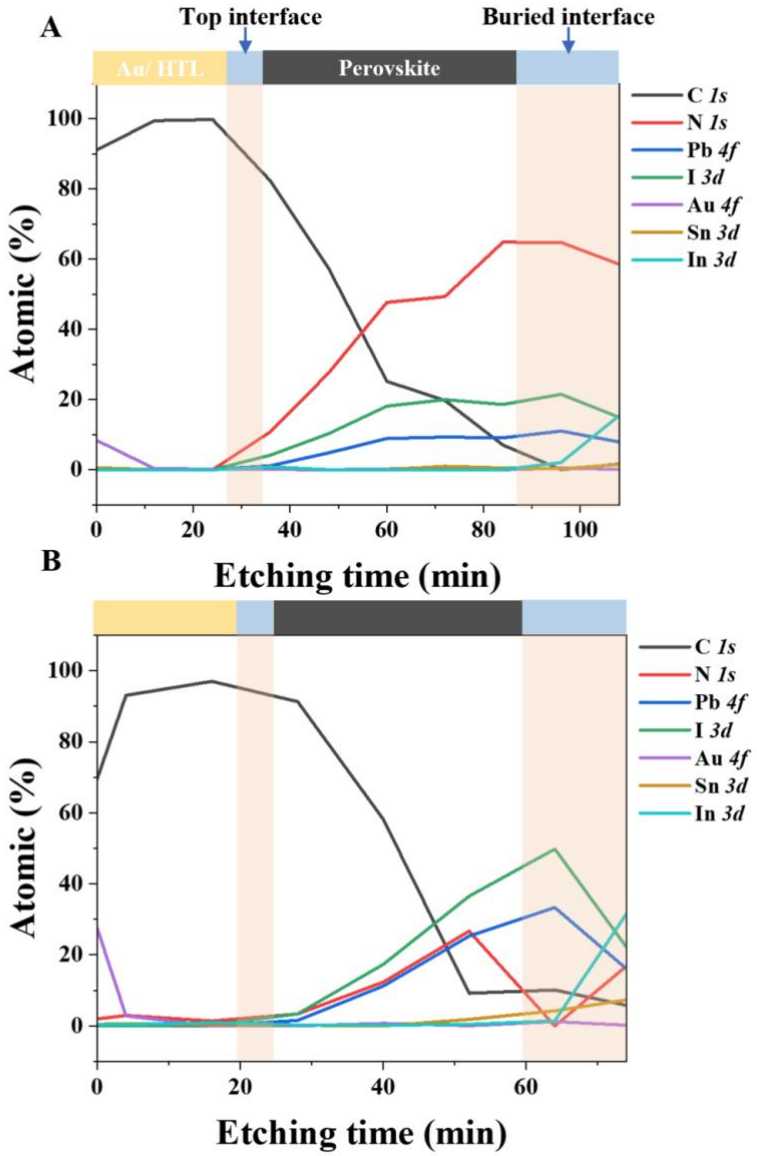

Figure 3.2 Depth-resolved XPS analysis of the perovskite device stack before and after operation. (A, B) Atomic concentration profiles of C *1s*, N *1s*, Pb *4f*, I *3d*, Au *4f*, Sn *3d*, and In *3d* as a function of etching time. The shaded regions indicate the approximate locations of the top interface, perovskite layer, and buried interface.

Chapter 4 Regulating Buried Interface Ion Migration for Enhanced Stability

4.1 Ion Migration at the Buried SnO_2/Perovskite Interface

Ion migration is one of the intrinsic processes that strongly influences the operational stability of metal halide perovskite solar cells. Owing to the soft and ionic nature of the perovskite lattice, mobile ionic species can redistribute under external stimuli such as illumination, electrical bias, and elevated temperature[1,2,3]. Such redistribution can modify local electric fields, alter defect populations, promote interfacial reactions, and eventually accelerate chemical and structural degradation[4]. While extensive studies have focused on the migration of intrinsic ionic species within the perovskite absorber, comparatively less attention has been paid to species originating from adjacent functional layers and migrating across heterogeneous interfaces.

As discussed in Chapter 3, the buried interface between the SnO_2 electron-transport layer and the perovskite absorber represents a particularly dynamic region during device operation. Depth-resolved characterization revealed pronounced compositional evolution near this interface after aging, suggesting that the buried region is not chemically static. Because SnO_2 is in direct contact with the perovskite absorber throughout device operation, an important question arises as to whether Sn-containing species from the electron-transport layer can redistribute across the interface and participate in perovskite degradation.

This possibility is particularly relevant because bulk SnO_2 is generally considered thermodynamically stable, whereas the actual SnO_2/perovskite interface exists in a chemically complex and nonequilibrium environment[5]. During device operation, illumination, carrier accumulation, local electric fields, and ionic redistribution may alter the local interfacial chemistry. Under such conditions, the behavior of Sn-containing species at the interface may differ substantially from that expected for bulk SnO_2.

Therefore, the first objective of this chapter is to directly examine whether Sn redistribution occurs across the buried interface during prolonged operation. The second objective is to determine whether the redistributed Sn undergoes chemical-state evolution after entering the perovskite absorber. Finally, based on this mechanistic understanding, polymeric interlayers are explored as ion-regulating barriers to suppress cross-interface Sn migration and improve long-term device stability.

4.2 Cross-Interface Sn Redistribution during Long-Term Operation

To directly investigate elemental redistribution at the buried interface, cross-sectional scanning transmission electron microscopy (STEM) combined with energy-dispersive X-ray spectroscopy (EDS) was performed on reference devices after prolonged maximum-power-point operation (**Figure 4.1A**). After 1000 h of MPPT aging, the cross-sectional STEM image showed a structurally degraded region near the SnO_2/perovskite interface. More importantly, the corresponding Sn EDS elemental map revealed that Sn-containing species were no longer confined to the SnO_2 electron-transport layer but extended into the lower region of the perovskite absorber.

This result provides direct spatial evidence that Sn species originating from the adjacent electron-transport layer can migrate across the buried interface during long-term device operation. Such behavior is fundamentally different from conventional descriptions of ion migration that primarily consider redistribution of intrinsic perovskite species, such as halide vacancies or halide ions, within the absorber itself. Instead, the observed Sn penetration represents a cross-interface degradation process involving chemical species originating from a neighboring functional layer.

The EDS results were further supported by X-ray photoelectron spectroscopy of the exposed buried perovskite surface. Compared with the fresh reference sample, a detectable Sn *3d* signal appeared after device aging, indicating that Sn-containing species had reached the

perovskite side of the buried interface. Supplementary XPS analysis of the aged reference sample quantified the Sn concentration at approximately 0.25 at% (**Table C4.1**), whereas no measurable Sn signal was observed for polymer-modified samples under comparable conditions (**Figure 4.3C**).

Taken together, the cross-sectional STEM/EDS and buried-interface XPS measurements demonstrate that Sn redistribution occurs across the SnO_2/perovskite interface during prolonged operation. These observations establish the SnO_2 layer as a potential source of mobile species and suggest that degradation at the buried interface involves interactions extending beyond the intrinsic ionic dynamics of the perovskite absorber.

The observation of migrated Sn raises a further question. If Sn species leave the SnO_2 layer and enter the iodide-rich perovskite environment, they may no longer retain the same local coordination or oxidation state as Sn in pristine SnO_2. Understanding the chemical state of the redistributed Sn is therefore essential for evaluating its possible impact on perovskite stability.

4.3 Chemical-State Evolution of Redistributed Sn

The chemical state of the redistributed Sn species was investigated using Sn K-edge X-ray absorption near-edge structure spectroscopy (XANES). Because the absorption-edge position and near-edge structure are sensitive to oxidation state and local coordination, XANES provides a useful approach for distinguishing Sn species in different chemical environments.

As shown in **Figure 4.1C**, SnO_2 and SnI_2 were used as reference materials representing predominantly Sn^{4+} and Sn^{2+} chemical states, respectively. The absorption edge measured from the operation-aged sample was located between those of SnO_2 and SnI_2, indicating that the migrated Sn no longer retained exclusively the Sn^{4+} environment characteristic of SnO_2. Instead, the data are consistent with partial evolution toward a lower-valence Sn state after redistribution

into the perovskite environment. The corresponding derivative spectra further confirm that the edge position of the aged sample lies between those of the SnO_2 and SnI_2 references (**Figure B4.1**).

This chemical-state evolution suggests that Sn migration is not simply a physical diffusion process. Once Sn-containing species enter the iodide-rich perovskite environment, they may participate in redox reactions or form new local coordination structures. One plausible reaction pathway involves reduction of Sn (IV) species toward Sn (II), accompanied by oxidation of iodide: $Sn\ (IV)+2I^{-}\rightarrow Sn\ (II)+I_2$. This reaction is proposed only as a possible stoichiometric scenario rather than a directly demonstrated or thermodynamically established pathway under the present experimental conditions[6,7]. Nevertheless, it provides a potential coupling between the chemical-state evolution of redistributed Sn and iodide oxidation.

Such a process may have at least two possible consequences. First, oxidation of iodide can contribute to halide loss and compositional instability, promoting phase degradation of the perovskite absorber[7]. Second, lower-valence Sn species introduced into a nominally Pb-based perovskite may perturb the local chemical and electronic environment. Uncontrolled Sn incorporation could alter defect chemistry, introduce additional trap states, or increase non-radiative recombination[8,9]. The key implication is therefore that the migration of Sn from the ETL may affect the perovskite through both physical redistribution and subsequent chemical transformation. In this sense, instability of the SnO_2 layer and degradation of the perovskite absorber are coupled through the buried interface.

These observations motivated the development of an interfacial strategy capable of suppressing cross-interface ionic transport before migrated species can chemically interact with the perovskite.

4.4 Ion-Filter-Inspired Polymeric Interlayers for Suppressing Ion Migration

To regulate cross-interface Sn transport, we drew inspiration from polymeric ion-selective barriers used in electrochemical energy-storage systems. In redox flow batteries, polymer-containing membranes or separators are frequently employed to reduce undesired species crossover while maintaining the transport processes required for cell operation[10]. PVP-containing polymers have been explored as materials for regulating selective ion transport[11]. This concept suggested that an ultrathin polymeric layer might similarly function as an interfacial "ion filter" in perovskite solar cells.

Importantly, the objective was not to introduce a thick insulating barrier that completely blocks transport across the interface. In a functioning solar cell, photogenerated electrons must still be efficiently extracted from the perovskite into the SnO_2 electron-transport layer. Therefore, the desired interlayer should selectively increase resistance to slow ionic motion while remaining sufficiently thin and electronically compatible to preserve charge extraction.

PVP was selected as a starting point because of its compatibility with perovskite processing and its previous use in ion-regulating polymer systems[12,13]. Based on this structural motif, two related polymers, poly(1-ethenyl-3-methylpyrrolidin-2-one) (PEM) and poly(1-ethenylpyrrolidine-2,5-dione) (PED), were synthesized in-house and further introduced as model interlayers (**Figure 4.1D** and **E**). These three polymers provide related carbonyl-containing chemical environments but differ in molecular structure and local coordination, allowing the relationship between polymer structure and ion-regulating capability to be systematically evaluated. The polymers were inserted as ultrathin interlayers between SnO_2 and the perovskite absorber.

The central hypothesis was that the polymeric interlayers could increase the energetic barrier for Sn migration across the buried interface. Because ionic migration involves atomic or

defect hopping along available pathways, even a moderate increase in migration barrier can substantially reduce the migration rate. This concept is fundamentally different from electronic charge transport, which can remain efficient through an ultrathin interlayer through electronic coupling and favorable energetic alignment.

The ability of the different polymers to impede Sn migration was therefore first evaluated computationally and subsequently verified through temperature-dependent electrical measurements. DFT calculations were employed to evaluate the energy barrier for Sn migration through the different polymer-modified interfaces (**Figure 4.2A**). For each polymer system, initial and final Sn configurations were first optimized, corresponding to Sn located above the polymer layer and Sn approaching the polymer/perovskite interface (**Figure 4.2B** to **D**). Intermediate structures were generated along the migration coordinate, and the minimum-energy pathway was evaluated using the nudged elastic band method and constrained minimization with 16 intermediate images.

All three polymeric interlayers introduced additional energetic barriers to Sn migration. Among them, PED exhibited the highest calculated migration barrier of 0.54 eV, followed by PVP at 0.35 eV and PEM at 0.25 eV. This trend indicates that the molecular structure of the polymer strongly influences the energetic accessibility of the cross-interface migration pathway, with PED providing the most effective barrier to Sn transport.

To experimentally probe the overall ionic migration behavior, temperature-dependent conductivity measurements were performed on devices with and without polymeric interlayers (**Figure 4.2E**). The apparent activation energy for ion migration was extracted from the temperature dependence of conductivity using the Nernst–Einstein relationship. The reference

device exhibited an activation energy of 0.262 eV, whereas the values increased to 0.402 eV for PED, 0.295 eV for PEM, and 0.320 eV for PVP.

Although the temperature-dependent conductivity measurement reflects the collective response of multiple mobile ionic species rather than Sn migration alone, the experimental trend is consistent with the DFT calculations. PED again exhibits the largest activation energy, supporting the conclusion that it creates the most resistant interfacial environment for ionic motion.

Resistive-switching measurements provided an additional probe of field-driven ion migration (**Figure 4.3A**). The transition from a high-resistance state to a low-resistance state is associated with the formation of conductive pathways facilitated by mobile ionic species. The reference structure exhibited an abrupt SET transition below approximately 1 V, whereas structures containing polymeric interlayers required larger applied voltages before switching. Representative PED-containing devices showed particularly delayed transitions, indicating substantially hindered ionic redistribution.

Statistical measurements further supported this trend as shown in **Figure B4.2**. The average SET voltage increased from approximately 0.955 V for the reference device to 2.33 V for the PED-containing structure, compared with 1.05 V for PEM and 1.14 V for PVP. In contrast, polymer-only structures without SnO_2 exhibited substantially lower switching voltages, indicating that the increased switching threshold in the complete device cannot be attributed simply to the intrinsic insulating character of the polymer layer. Instead, the results suggest that the SnO_2/polymer interfacial configuration plays an important role in restricting mobile-ion transport.

Collectively, the computational and experimental results identify PED as the most effective polymer for increasing the barrier to ionic motion. The next question is whether this increased

migration barrier translates into directly measurable suppression of Sn redistribution during device operation.

To directly evaluate the ability of the polymeric interlayers to suppress Sn migration, aged devices incorporating PED were analyzed using cross-sectional STEM/EDS under the same long-term operating conditions used for the reference devices (**Figure 4.1B**). In strong contrast to the reference sample, where Sn penetration into the lower perovskite region was clearly observed, the PED-modified device retained a much more sharply defined SnO_2/perovskite boundary. No discernible Sn penetration into the absorber was observed in the Sn elemental map after 1000 h of MPPT aging.

The suppression of Sn redistribution was independently quantified using inductively coupled plasma atomic emission spectroscopy (ICP-AES). Perovskite films were removed from the substrate after MPPT aging and dissolved for elemental analysis. In the reference sample, the Sn concentration increased from approximately 0.83 at% in the fresh film to approximately 2.03 at% after 100 h of MPPT operation (**Figure 4.3B**). In comparison, the PED-modified sample exhibited only a minor increase from approximately 0.34 at% to 0.41 at%. Duplicate ICP-AES measurements showed the same trend, confirming the strong suppression of Sn accumulation by the PED interlayer.

Buried-interface XPS measurements provided further supporting evidence (**Figure 4.3C**). A detectable Sn signal was observed in the aged reference sample, whereas no measurable Sn was found in polymer-interlayer-treated samples. The agreement among STEM/EDS, ICP-AES, and XPS is significant because these methods probe Sn redistribution through complementary spatial and analytical approaches.

The experimental suppression of Sn redistribution closely follows the calculated and measured migration barriers. PED exhibits the highest DFT Sn migration barrier, the highest apparent ionic activation energy, and the strongest suppression of Sn accumulation during operation. These results establish a direct relationship between the molecularly engineered interlayer, increased resistance to ionic transport, and reduced cross-interface Sn migration.

Thus, the polymer interlayer does not merely alter the static buried-interface chemistry. It actively regulates the dynamic redistribution of species during prolonged device operation.

4.5 Suppressed Ion Migration Enhances Long-Term Stability

The practical consequence of suppressing cross-interface ion migration was evaluated through long-term operational stability measurements. Encapsulated devices were operated continuously under maximum-power-point tracking using one-sun-equivalent white-light illumination at 65 °C in a nitrogen-filled glovebox (**Figure 4.4A**). The reference device exhibited progressive performance degradation and ultimately lost essentially all its initial photovoltaic performance. In contrast, the PED-modified device maintained approximately 96% of its initial PCE after 2000 h of continuous operation. Devices incorporating PEM and PVP also exhibited improved stability relative to the reference, although PED provided the strongest performance retention.

The devices were further subjected to accelerated thermal-light aging under ISOS-L-2I conditions. Unencapsulated devices were operated under one-sun-equivalent illumination at 85 °C in a nitrogen-filled glovebox (**Figure 4.4B**). After 2400 h, the reference device had completely degraded, whereas PED-, PEM-, and PVP-modified devices retained 90.5%, 63.7%, and 41.5% of their initial PCEs, respectively.

To further verify that the stability enhancement induced by the buried polymeric interlayers is reproducible in devices employing spiro-OMeTAD as the hole-transport layer, additional thermal-light stability measurements were performed under one-sun illumination at 65 °C. Ten devices were evaluated for each condition to provide statistical comparison. The reference devices exhibited rapid performance degradation, whereas all polymer-modified devices showed substantially improved stability. Among them, PED-modified devices maintained the highest photovoltaic performance throughout the aging period, followed by PEM- and PVP-modified devices. The consistent stability improvement observed in the spiro-OMeTAD-based devices further supports the conclusion that regulation of the buried interface, rather than a specific choice of the hole-transport layer, plays a central role in suppressing degradation during prolonged thermal-light stress.

The enhanced device stability was accompanied by improved preservation of the buried-interface chemical environment (**Figure 4.3D**). After aging, the Pb 4f spectrum of the reference sample exhibited substantial peak broadening and a positive binding-energy shift of approximately 0.81 eV, indicating pronounced chemical evolution of Pb-containing species. In comparison, the PED-modified sample showed a much smaller shift of approximately 0.15 eV and largely retained its original spectral line shape. PVP- and PEM-modified samples also showed improved chemical stability compared with the reference, although PED again provided the strongest protection.

These results link suppressed cross-interface ion migration with improved chemical and operational stability. PED consistently exhibits the highest migration barrier, the largest apparent ionic activation energy, the strongest suppression of Sn redistribution, and the best long-term device stability. The convergence of these independent measurements supports the conclusion that

regulation of cross-interface Sn migration is an important contributor to the enhanced operational durability of polymer-modified devices.

It should be emphasized that Sn migration is unlikely to represent the sole degradation mechanism in perovskite solar cells. Device degradation remains a coupled process involving ionic redistribution, interfacial reactions, phase evolution, defect formation, and structural changes. Rather, the results presented here identify cross-interface Sn redistribution as an important degradation pathway associated with the SnO_2/perovskite buried interface.

This chapter therefore establishes the buried interface as an active ionic boundary whose dynamic evolution can be regulated through polymeric interlayers. By increasing the energetic barrier to Sn migration, the polymeric interlayers suppress cross-interface redistribution and stabilize the chemical environment of the perovskite during prolonged operation. Among the investigated polymers, PED provides the most effective ion-regulating function and consequently enables substantially improved long-term operational stability.

The next chapter addresses a complementary role of the same buried interlayer: its influence on perovskite nucleation, crystallization, buried-interface formation, and the resulting optoelectronic quality of the absorber.

References

1 Eames, C. et al. Ionic transport in hybrid lead iodide perovskite solar cells. *Nature Communications* **6**, 7497 (2015).

2 Azpiroz, J. M. et al. Defect migration in methylammonium lead iodide and its role in perovskite solar cell degradation. *Energy & Environmental Science* **8**, 2118–2127 (2015).

3 Tress, W. et al. Understanding the rate-dependent J–V hysteresis, slow time component, and aging in $CH_3NH_3Pb(I,Br)_3$ perovskite solar cells. *Energy & Environmental Science* **11**, 151–167 (2018).

4 Boyd, C. C. et al. Understanding degradation mechanisms and improving stability of perovskite photovoltaics. *Chemical Reviews* **119**, 3418–3451 (2019).

5 Xu, Y. et al. Dual passivation of SnO_2/perovskite heterogeneous interfacial defects for efficient perovskite solar cells. *Solar Energy Materials and Solar Cells* **250**, 112088 (2023).

6 Sánchez-Díaz, J. et al. Tin perovskite solar cells with >1,300 h of operational stability in N_2 through a synergistic chemical engineering approach. *Joule* **6**, 861–883 (2022).

7 Domanski, K. et al. Migration of cations induces reversible performance losses over day/night cycling in perovskite solar cells. *Energy & Environmental Science* **10**, 604–613 (2017).

8 Klug, M. T. et al. Metal composition influences optoelectronic quality in mixed-metal lead–tin triiodide perovskite solar absorbers. *Energy & Environmental Science* **13**, 1776–1787 (2020).

9 Leijtens, T. et al. Mechanism of tin oxidation and stabilization by lead substitution in tin halide perovskites. *ACS Energy Letters* **2**, 2159–2165 (2017).

10 Huynh, T. T. K. et al. Construction of high-performance membranes for vanadium redox flow batteries: Challenges, development, and perspectives. *Nano-Micro Letters* **17**, 260 (2025).

11 Zeng, L. et al. Polyvinylpyrrolidone-based semi-interpenetrating polymer networks as highly selective and chemically stable membranes for all vanadium redox flow batteries. *Journal of Power Sources* **327**, 374–383 (2016).

12 Du, C. et al. Polyvinylpyrrolidone as additive for perovskite solar cells with water and isopropanol as solvents. *Beilstein Journal of Nanotechnology* **10**, 2374–2382 (2019).

13 Zhang, M. et al. High-efficiency perovskite solar cells with poly(vinylpyrrolidone)-doped SnO_2 as an electron transport layer. *Materials Advances* **1**, 617–624 (2020).

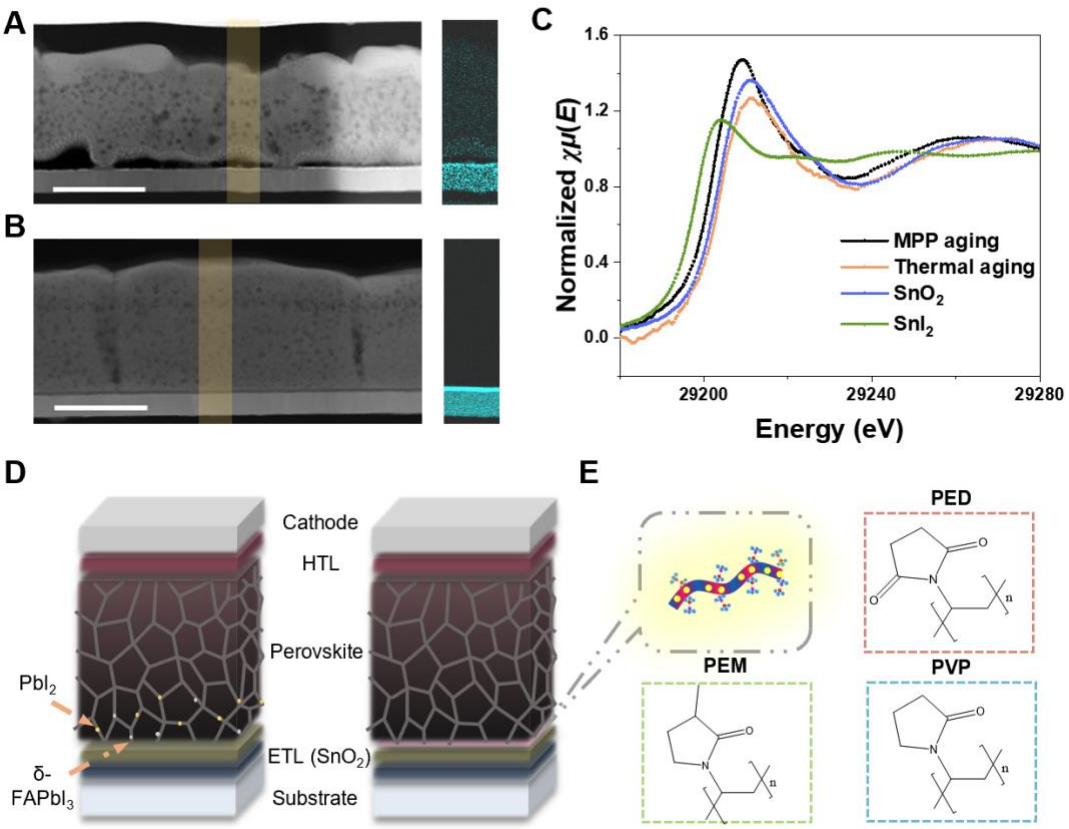

Figure 4.1 Cross-interface Sn redistribution, chemical-state evolution, and polymeric interlayer design. (A) Cross-sectional STEM image (scale bar, 500 nm) and Sn EDS elemental map of the highlighted area in the reference sample after 1000 hours of MPPT aging. The yellow shaded regions indicate the areas corresponding to the Sn EDS analysis. (B) Cross-sectional STEM image and tin EDS elemental map of the highlighted area in the PED-treated sample after MPPT aging for 1000 hours. The yellow shaded regions indicate the areas corresponding to the Sn EDS analysis. (C) Sn K-edge X-ray absorption near-edge spectra showing intermediate oxidation state (between those of SnI_2 and SnO_2) for the aged sample. (D) Schematic device illustration. (E) Polymer structures of PED, PEM and PVP.

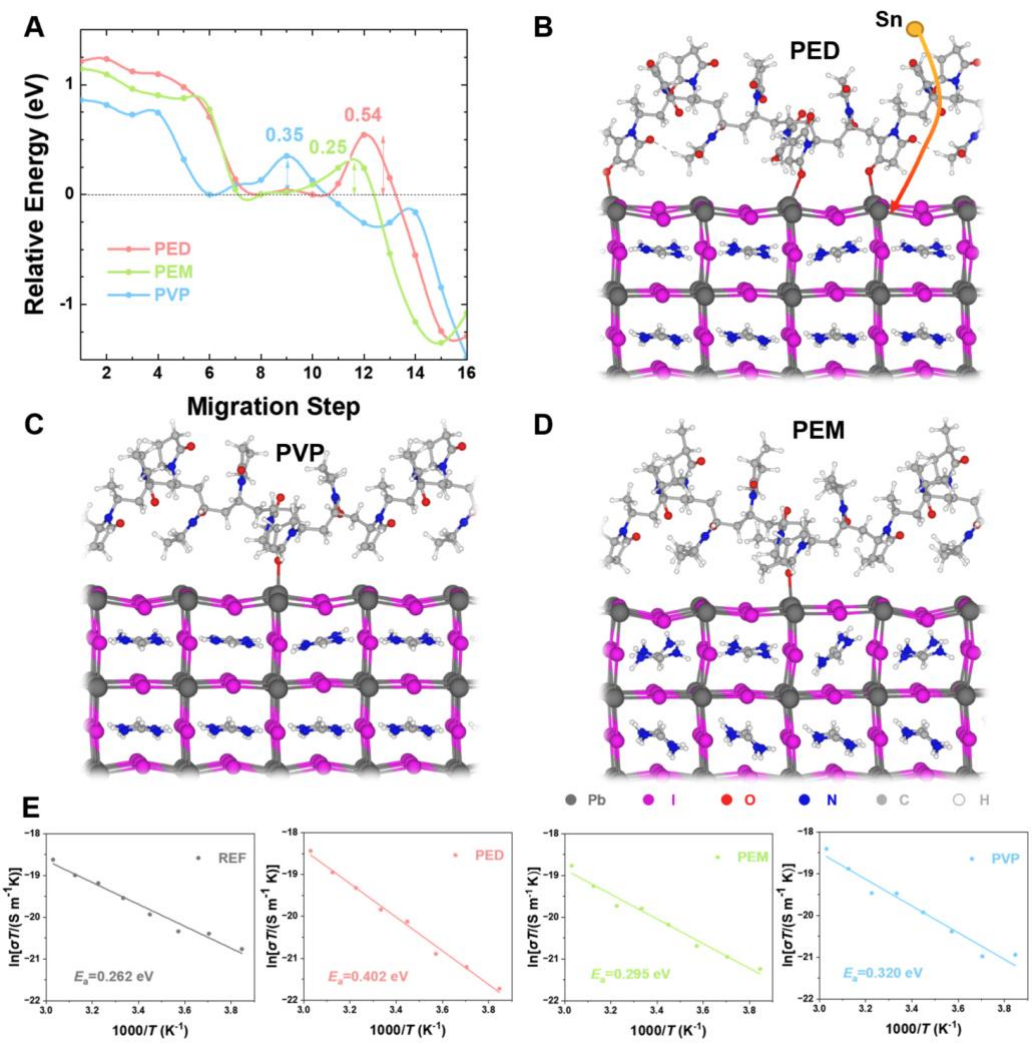

Figure 4.2 Polymeric interlayers increase the energetic barrier for cross-interface Sn migration. (A) Calculated Sn migration energy profiles for the PED, PEM and PVP interlayers. (B)–(D), Corresponding atomic models of the interfaces with PED (B), PVP (C) and PEM (D) interlayers. In B, the orange arrow indicates the simulated Sn migration pathway. (E) Temperature-dependent conductivity of devices without and with PED, PEM and PVP polymeric interlayers. E_a is the activation energy. Symbols represent measured data and lines represent linear fits.

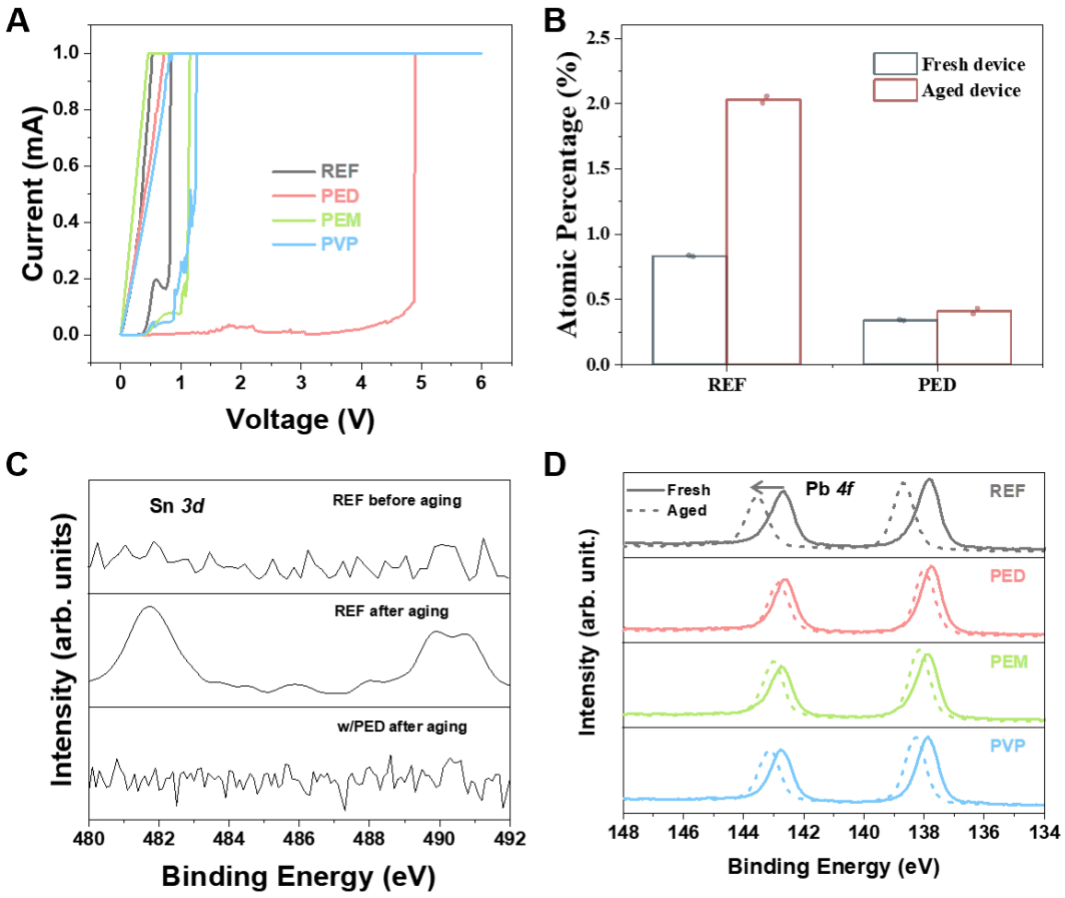

Figure 4.3 Polymeric interlayers suppress Sn redistribution and preserve buried-interface chemical stability. (A) Resistive switching measurements of perovskite solar cells with or without polymeric interlayers. (B) ICP-AES measurements of Sn content in aged and fresh samples. Bars represent the mean of two independent results (n=2), with individual data points shown. (C) XPS spectra for Sn 3d of the buried interface before aging and after aging. (D) Pb *4f* XPS spectra with and without polymeric interlayers before and after operation. The arrow indicates the binding-energy shift after aging.

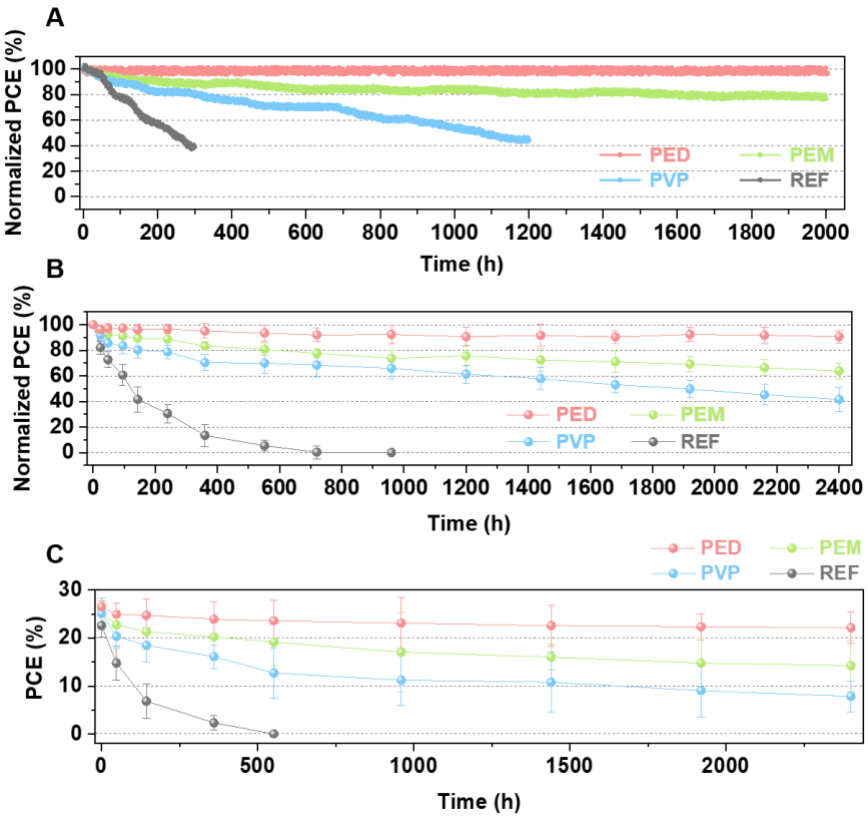

Figure 4.4 Stability of reference devices and devices with polymeric interlayer. (A) MPPT stability of PTAA-based devices under one-sun illumination at 65 °C with and without polymer interlayers. The initial PCEs of the reference, PED, PEM, and PVP devices were 21.88%, 24.89%, 24.08%, and 23.58%, respectively. (B) Thermal-light stability of PTAA-based devices under one-sun illumination at 85 °C with and without polymer interlayers. The initial PCEs of the reference, PED, PEM, and PVP devices were 22.57%, 25.28%, 24.31%, and 23.88%, respectively. Data points indicate the median values, and error bars represent the standard deviation across ten independent devices (n = 10). (C) 65 ℃ thermal-light stability test under one-sun illumination without or with the polymeric interlayers with spiro-OMeTAD as HTL. For each condition of the stability tests, ten devices were measured for statistical analysis. Centre is the median value. Error bars indicate the standard deviation from these samples.

Chapter 5 Strengthening the Buried Interface and Crystal Growth for Efficient Devices

5.1 Buried-Interface Regulation of Perovskite Formation

Chapter 4 demonstrates that the SnO_2/perovskite buried interface acts as a dynamic ionic boundary during prolonged device operation and that polymeric interlayers can substantially suppress cross-interface Sn redistribution. However, the role of the buried interface begins much earlier than device operation. Because the interfacial layer is introduced before formation of the perovskite absorber, it can directly influence the nucleation, crystallization, and morphology of the subsequently deposited perovskite film.

This distinction is particularly important for the two-step perovskite deposition process employed in this work. The SnO_2 electron-transport layer was first coated with an ultrathin polymeric interlayer, followed by deposition of the PbI_2 precursor and subsequent conversion into the mixed-cation perovskite through reaction with the organic halide solution. The polymer-modified SnO_2 surface therefore directly interacts with the precursor during the earliest stages of film formation. Changes in surface chemistry, wettability, and polymer–precursor interaction can consequently influence precursor distribution and heterogeneous nucleation at the buried interface.

In heterogeneous nucleation, the energetic environment of the underlying substrate plays an important role in determining the barrier for formation of stable nuclei[1,2]. Modification of the substrate surface can alter the density and spatial distribution of nucleation sites and subsequently affect crystal growth. In addition, carbonyl-containing groups within the polymeric interlayers may interact with Pb-containing precursor species, potentially modifying local precursor coordination and crystallization kinetics[3,4]. Such interactions provide a plausible pathway through which the buried interlayer can regulate the growth of the overlying perovskite absorber.

It should be emphasized that the present study does not directly track the nucleation process in situ. Therefore, the detailed microscopic mechanism by which the polymers alter nucleation and crystal growth cannot be established solely from the final film characterization. Instead, the influence of buried-interface modification is evaluated through its observable consequences, including substrate wettability, interfacial morphology, crystal-phase composition, trap-state density, carrier recombination, and ultimately photovoltaic performance.

The objective of this chapter is therefore to determine whether the same polymeric interlayers developed for buried-interface stabilization can also improve the formation and optoelectronic quality of the perovskite absorber.

5.2 Polymeric Interlayers Improve Buried-Interface Formation and Contact

Because perovskite formation begins directly on the underlying electron-transport layer, the surface properties of SnO_2 can strongly influence the morphology of the buried interface. The effect of polymer modification on substrate wettability was first examined through contact-angle measurements (**Figure 5.1A**). The water contact angle decreased from 26.25° for the pristine SnO_2 reference surface to 12.95° after PED modification, while PEM- and PVP-modified surfaces exhibited contact angles of 17.60° and 17.05°, respectively. These results indicate substantially enhanced surface wettability after polymer modification, with PED producing the strongest effect.

The smaller contact angles are qualitatively consistent with an increase in surface affinity toward polar species and changes in the effective surface-energy environment. These results should be interpreted primarily as a comparative indicator of surface modification rather than as a direct measurement of precursor wetting during film deposition. The systematic differences among the four substrates demonstrate that insertion of the polymer interlayers substantially alters the chemical environment encountered by the perovskite precursor.

Cross-sectional scanning electron microscopy (SEM) of fresh devices revealed a corresponding change in buried-interface morphology (**Figure 5.1 B–E**). Reference devices exhibited regions of incomplete contact and interfacial voids between the SnO_2 layer and the perovskite absorber. In contrast, devices incorporating polymeric interlayers showed more continuous contact between the perovskite and underlying electron-transport layer. PED produced particularly compact and uniform interfacial contact, consistent with its stronger modification of the substrate surface.

Additional information was obtained by mechanically peeling fresh perovskite films to directly expose their buried surfaces (**Figure B5.1**). Atomic force microscopy images showed distinct buried morphologies for the reference and polymer-modified films, confirming that modification of the underlying SnO_2 surface affects the bottom surface of the perovskite after crystallization.

To further examine the morphological stability of the buried interface during device operation, the perovskite layers were also peeled from the substrates, which were subsequently characterized by SEM before and after operation (**Figure 5.2A**). The fresh buried surfaces exhibited relatively compact morphologies for all conditions. After 200 hours of operation, however, the reference sample developed more pronounced void- and pinhole-like features at the buried surface, indicating substantial morphological deterioration during aging. In comparison, the polymer-modified samples preserved a more uniform and compact buried-interface morphology, with substantially fewer newly formed voids. Among the investigated interlayers, the PED-modified sample exhibited particularly good morphological integrity after operation. These observations indicate that polymeric interlayers not only improve the initial physical contact at the

SnO_2/perovskite interface but also help preserve the structural integrity of the buried interface during device operation.

To elucidate the distinct interfacial behaviors of the three polymers, molecular dynamics (MD) simulations were performed to investigate their interactions with the perovskite surface. As illustrated in **Figure 5B - D**, PED molecules exhibited strong adhesion and close packing at the perovskite interface, forming a compact and robust interfacial configuration. In contrast, a significant fraction of PEM and PVP molecules detached from the surface, suggesting weaker interfacial interactions and a higher tendency for nonuniform coverage. In practical device structures, such weak adhesion may promote polymer aggregation and result in incomplete interlayer formation, thereby reducing passivation effectiveness and allowing morphological defects to persist[5].

These observations are important because interfacial contact influences both the formation and electronic operation of the device. Interfacial voids can interrupt charge-transfer pathways and create regions with poor mechanical and chemical contact. At the same time, the geometry of grain-boundary grooves at the buried surface is sensitive to the interfacial energetic environment during film formation[6-8]. Modification of SnO_2 by the polymeric layers can therefore influence the physical configuration of the buried interface before any electronic passivation effect is considered.

Taken together, the contact-angle, cross-sectional SEM, and buried-surface morphology measurements demonstrate that polymeric interlayers do not simply remain as passive layers between SnO_2 and the perovskite. Instead, they modify the substrate environment during film formation and promote a more intimate and spatially uniform buried interface.

The next question is whether these morphological changes are accompanied by measurable differences in perovskite crystallization and phase composition.

5.3 Polymeric Interlayers Regulate Perovskite Crystallization and Phase Quality

X-ray diffraction was employed to investigate the crystal-phase composition of perovskite films formed on the different buried interfaces (**Figure 5.3A**). Fresh samples exhibited the characteristic diffraction peaks of the photoactive α-$FAPbI_3$-based perovskite phase together with a secondary PbI_2-related peak. Modification of the SnO_2 surface with polymeric interlayers altered the relative contribution of these phases, with PED-treated samples exhibiting reduced secondary PbI_2 features relative to the reference and improved formation of the desired perovskite phase.

The difference in residual PbI_2 is particularly relevant to the two-step deposition process used here. In this process, PbI_2 is first deposited onto the SnO_2 or polymer-modified SnO_2 substrate before reaction with the organic halide precursor. The properties of the underlying surface can therefore influence the initial PbI_2 nucleation and crystallization and, consequently, its subsequent conversion into the final perovskite phase. The reduced secondary PbI_2 observed after polymer modification is consistent with more effectively regulated precursor crystallization and conversion.

A plausible interpretation is that the polymeric interlayers modify two related aspects of film formation. First, the altered surface-energy environment changes heterogeneous nucleation at the bottom interface, promoting a more spatially uniform nucleation process[9]. Second, interactions between carbonyl-containing polymer groups and Pb-containing precursor species may modify local Pb coordination and crystal-growth kinetics[1]. These effects can provide more controlled crystal formation and reduce the formation of undesirable residual phases. However, because the nucleation and conversion processes were not directly monitored in real time, these mechanisms

should be regarded as a structure–processing interpretation consistent with the observed final film properties rather than as direct evidence of a specific nucleation pathway.

The influence of the buried interlayer was also apparent after device operation. XRD measurements of aged samples showed substantially more pronounced phase evolution in the reference film, including increased PbI_2-related diffraction and formation of the non-photoactive δ-$FAPbI_3$ phase (**Figure 5.3B**). In contrast, polymer-modified samples exhibited improved preservation of the photoactive α-perovskite phase, with PED providing the strongest phase retention. These results demonstrate both improved initial crystallization and suppressed phase degradation during operation.

This observation provides an important connection between Chapters 4 and 5. Chapter 4 demonstrates that PED suppresses dynamic cross-interface ion migration during operation, whereas the present results indicate that the same interlayer also creates a more favorable perovskite structure before operation begins. Enhanced long-term phase stability may therefore arise from both reduced dynamic chemical perturbation and improved initial crystal quality.

Importantly, the objective of buried-interface engineering is not simply to maximize crystallinity or eliminate all secondary phases. Rather, the relevant question is whether changes in film formation reduce electronically detrimental disorder and improve the optoelectronic quality of the resulting absorber. This was evaluated through carrier-recombination and trap-state measurements.

5.4 Polymeric Interlayers Reduce Trap States and Non-Radiative Recombination

The optoelectronic quality of the perovskite films was investigated using steady-state photoluminescence and time-resolved photoluminescence measurements. Polymer-modified perovskite films exhibited enhanced PL emission compared with the reference film, indicating

reduced non-radiative carrier losses (**Figure 5.3D**). The effect was most pronounced for the PED-modified sample.

Time-resolved PL measurements provided direct information on carrier recombination dynamics (**Figure 5.3C**). The average carrier lifetime increased from approximately 0.52 μs for the reference film to 0.96 μs for PVP, 1.10 μs for PEM, and 1.43 μs for PED. Thus, all three polymer-modified buried interfaces prolonged the photogenerated carrier lifetime, with PED producing nearly a threefold increase compared with the untreated reference.

The extended carrier lifetime is consistent with suppression of non-radiative recombination. In a semiconductor containing a large population of electronically active traps, photogenerated electrons and holes can be captured by defect states and recombine through trap-assisted pathways. Reducing the concentration or electronic activity of these defects decreases the first-order non-radiative recombination contribution and allows photogenerated carriers to persist for longer times.

To directly evaluate the density and energetic distribution of electrically active defect states, trap density of states (tDOS) was extracted from frequency-dependent capacitance measurements (**Figure 5.3E**). The polymer-modified devices exhibited lower tDOS compared with the reference, with PED showing the most pronounced reduction. This trend is consistent with the PL and TRPL measurements and confirms that the improved carrier lifetime originates from a reduction in electronically active defect states rather than from a change in optical absorption alone. These results combined with TRPL, steady-state PL, and tDOS to establish a consistent relationship between buried-interface modification and improved perovskite optoelectronic quality.

The reduced trap-state density likely reflects contributions from several effects that are difficult to separate experimentally. Direct chemical coordination between polymer functional groups and undercoordinated species can passivate defects close to the buried surface. At the same time, improved nucleation, reduced interfacial void formation, and more favorable crystallization can decrease the generation of structural imperfections during film formation. The observed electronic improvement should therefore be understood as the combined consequence of interfacial passivation and improved perovskite formation, rather than being attributed exclusively to either mechanism.

This distinction also differentiates the present buried-interface strategy from the top-surface passivation discussed in Chapter 2. In Chapter 2, polymeric modifiers were applied after perovskite crystallization and primarily interacted with already-formed surface defects. At the buried interface, the modifier is present before crystallization and can influence both defect passivation and defect formation itself.

The improved morphology, phase quality, carrier lifetime, and trap-state characteristics collectively suggest that polymer-modified buried interfaces should facilitate more efficient photovoltaic operation. This relationship was subsequently evaluated in complete solar-cell devices.

5.5 Enhanced Photovoltaic Performance and Device Scalability

Complete n–i–p perovskite solar cells were fabricated to determine whether the improvements in buried-interface formation and perovskite quality translated into enhanced photovoltaic performance. The introduction of polymeric interlayers improved the photovoltaic parameters relative to the reference devices, with PED producing the largest enhancement.

The champion reference device exhibited an open-circuit voltage of 1.136 V, a short-circuit current density of 25.20 mA cm^{-2}, a fill factor of 80.95%, and a power conversion efficiency of 23.17%. In comparison, the PED-modified device exhibited a V_{oc} of 1.191 V, J_{sc} of 26.10 mA cm^{-2}, and FF of 86.01%, yielding a champion reverse-scan PCE of 26.74% (**Figure 5.4A, Figure B5.2**). The simultaneous improvements in V_{oc}, J_{sc} and FF are consistent with the multiple effects of buried-interface engineering described above. Reduced non-radiative recombination contributes to the increase in V_{oc}, while improved interfacial contact and reduced defect-mediated transport losses can facilitate carrier extraction and enhance FF. The improved perovskite quality and charge collection also contribute to the increase in photocurrent.

Statistical measurements confirmed that the enhanced performance was not limited to a single champion device. Polymer-modified devices exhibited systematically higher PCE distributions than the reference, with PED producing the highest average performance. The polymer-modified devices also showed reduced current–voltage hysteresis relative to the untreated reference, consistent with improved interfacial quality and reduced defect-related electronic and ionic responses. **Figure B5.3** summarizes the statistical photovoltaic parameters and hysteresis behavior across multiple devices.

The performance enhancement was independently validated through third-party certification. A small-area PED-modified device with an active area of approximately 0.07 cm^2 achieved a certified PCE of 26.58%, confirming the high efficiency obtained from buried-interface engineering. The corresponding independent certification report is provided in **Figure B5.4**.

The stabilized PCE values also improved markedly, from 21.3% in the reference device to 26.2%, 24.4%, and 23.8% for PED-, PEM-, and PVP-modified devices, respectively (**Figure 5.4B**). External quantum efficiency (EQE) spectra (**Figure 5.4C**) confirmed these results, showing

excellent agreement between the integrated J_{sc} values and those obtained from *J–V* measurements, with less than 5% deviation for the PED-treated device (integrated J_{sc} = 25.2 mA cm^{-2}). While the EQE spectra displayed negligible differences above 500 nm, the PED-modified device exhibited a distinctly higher EQE in the 350-400 nm region, indicating improved photocarrier generation and extraction near the buried interface. As short-wavelength photons possess a high absorption coefficient and a shallow penetration depth in perovskites[10], they are predominantly absorbed adjacent to the bottom heterojunction. Therefore, this localized EQE enhancement supports improved suppression of interfacial non-radiative recombination and more efficient charge collection[11]. These results demonstrate that polymeric interlayers effectively enhance interfacial charge transport and overall photovoltaic performance, with PED yielding the most significant improvement.

To gain further insight into the origin of the improved device efficiency, the interfacial energy level alignment was examined using ultraviolet photoelectron spectroscopy (UPS) and Kelvin probe force microscopy (KPFM). Since the polymer layers function as interfacial modifiers rather than standalone charge-transport layers, UPS measurements were performed on SnO_2/polymer stacks to probe the device-relevant surface energetics at the buried interface. Polymer-only UPS spectra were also measured as references and are provided in **Figure B5.5**. As shown in **Figure B5.6** and Supplementary **Table C5.1**, the PED-modified SnO_2 exhibited a shallower work function compared with pristine SnO_2, while the valence-band onset remained nearly unchanged. These results indicate that PED modifies the surface electronic structure of SnO_2 without substantially changing its occupied-state onset. Such interfacial energy modulation is expected to improve energetic compatibility at the SnO_2/perovskite interface, contributing to more efficient electron extraction and reduced interfacial recombination. Crucially, this tailored

energy level alignment provides a clear physical link between the material energetics and the observed device performance. The minimized energy offset, likely driven by the interfacial dipoles of the polar polymer chains, is expected to increase the built-in potential and effectively suppress non-radiative carrier recombination at the buried interface. Together, this optimized interfacial energy alignment likely contributes to the substantial enhancement in V_{oc} observed in the *J-V* curves. The KPFM mapping also revealed a more homogeneous surface potential distribution for the PED-treated film, implying reduced surface trap density and a more uniform interface (**Figure B5.7**).

Building on the improvements observed in small-area devices, we further examined the scalability of the polymer-interlayer strategy by fabricating large-area perovskite modules with an active area of 21.54 cm^2. The optimized module achieved a certified efficiency of 24.17%, demonstrating that the beneficial effect of buried-interface engineering can be retained during substantial device-area scaling (**Figure 5.4D**). The module structure necessarily introduces additional losses compared with a small-area cell, including lateral resistive losses through the transparent electrode, interconnection resistance associated with P1/P2/P3 scribing (**Figure B5.8**), inactive-area losses, and spatial nonuniformity across the larger substrate. Nevertheless, the high certified module efficiency demonstrates that the polymeric interlayer remains compatible with large-area processing rather than functioning only under optimized small-cell conditions.

The module result is particularly significant in the context of the mechanisms established in this chapter. Large-area fabrication magnifies the consequences of nonuniform nucleation, local defects, interfacial voids, and subcell mismatch. The ability to obtain high module efficiency is therefore consistent with the more uniform buried-interface formation and improved perovskite quality observed after polymer modification.

Taken together, the results of this chapter establish a direct progression from buried-interface modification to photovoltaic performance. The PED interlayer provides the strongest improvement throughout this sequence, producing improved buried-interface morphology, favorable phase formation, the longest carrier lifetime, the lowest defect-state density, and the highest photovoltaic performance among the investigated conditions. Combined with the ion-regulation results presented in Chapter 4, these findings demonstrate that polymeric buried-interface engineering can address two complementary limitations of perovskite photovoltaics: the quality of the absorber formed during fabrication and the dynamic stability of the interface during operation.

References

1 Barua, P. et al. Bulk perovskite crystal properties determined by heterogeneous nucleation and growth. *Materials* **16**, 2110 (2023).

2 Kim, J. et al. Engineering of buried interfaces in perovskites: advancing sustainable photovoltaics. *Nano Convergence* **11**, 57 (2024).

3 Luo, C. et al. Engineering the buried interface in perovskite solar cells via lattice-matched electron transport layer. *Nature Photonics* **17**, 856–864 (2023).

4 Zhu, B. et al. Eliminating voids and residual PbI_2 beneath a perovskite film via buried interface modification for efficient solar cells. *ACS Applied Materials & Interfaces* **16**, 28560–28569 (2024).

5 Xing, Y. et al. Simultaneous Interfacial Defect Passivation and Free-Volume Reduction by Fluorinated Hole Transport Materials for High-Performance Perovskite Solar Cells. *Advanced Materials* **38**, e13884 (2025).

6 Hao, M. & Zhou, Y. Grain-boundary grooves in perovskite solar cells. *Joule* **8**, 913–921 (2024).

7 Xiao, T. et al. Elimination of grain surface concavities for improved perovskite thin-film interfaces. *Nature Energy* **9**, 999–1010 (2024).

8 Hao, M. et al. Flattening Grain-Boundary Grooves for Perovskite Solar Cells with High Optomechanical Reliability. *Advanced Materials* **35**, 2211155 (2023).

9 Bi, D. et al. Polymer-templated nucleation and crystal growth of perovskite films for solar cells with efficiency greater than 21%. *Nature Energy* **1**, 16142 (2016).

10 Lin, Q., Armin, A., Nagiri, R. C. R., Burn, P. L. & Meredith, P. Electro-optics of perovskite solar cells. *Nature Photonics* **9**, 106–112 (2015).

11 Min, H. et al. Perovskite solar cells with atomically coherent interlayers on SnO_2 electrodes. *Nature* **598**, 444–450 (2021).

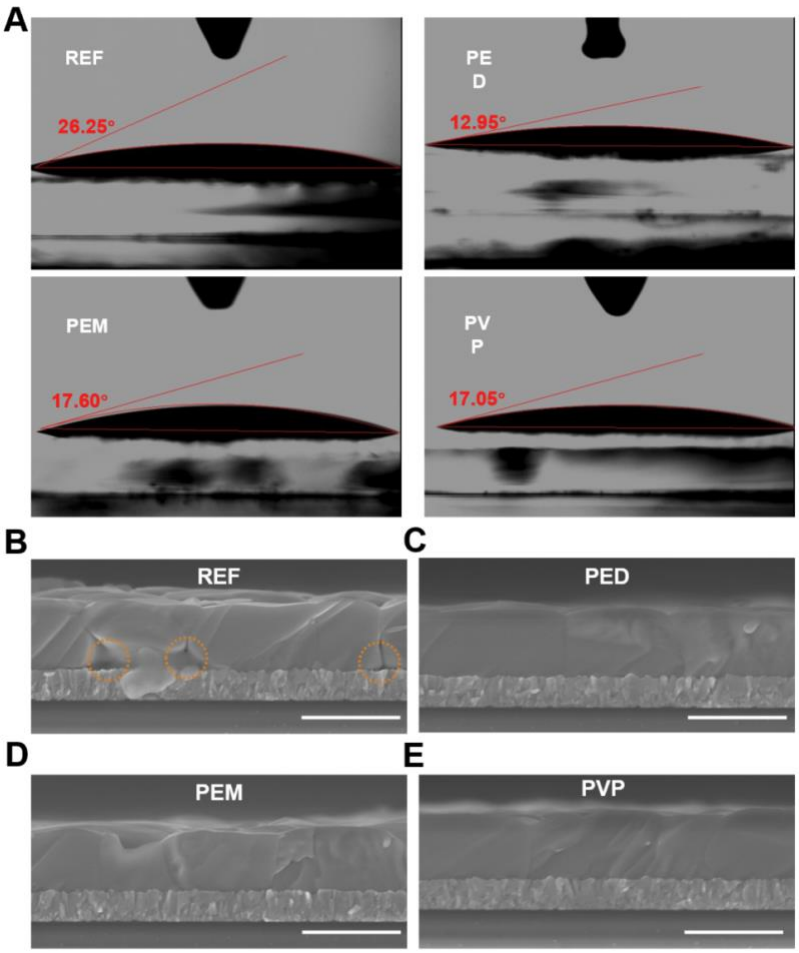

Figure 5.1 Polymeric interlayers improve surface wettability and buried-interface contact. (A) Contact angle of water on different surfaces. Cross-sectional SEM (scale bar, 1 μm) images of the fresh perovskite film: (B) without a polymeric interlayer; (C) with PED; (D) with PEM; (E) with PVP. Orange dashed circles highlight interfacial voids.

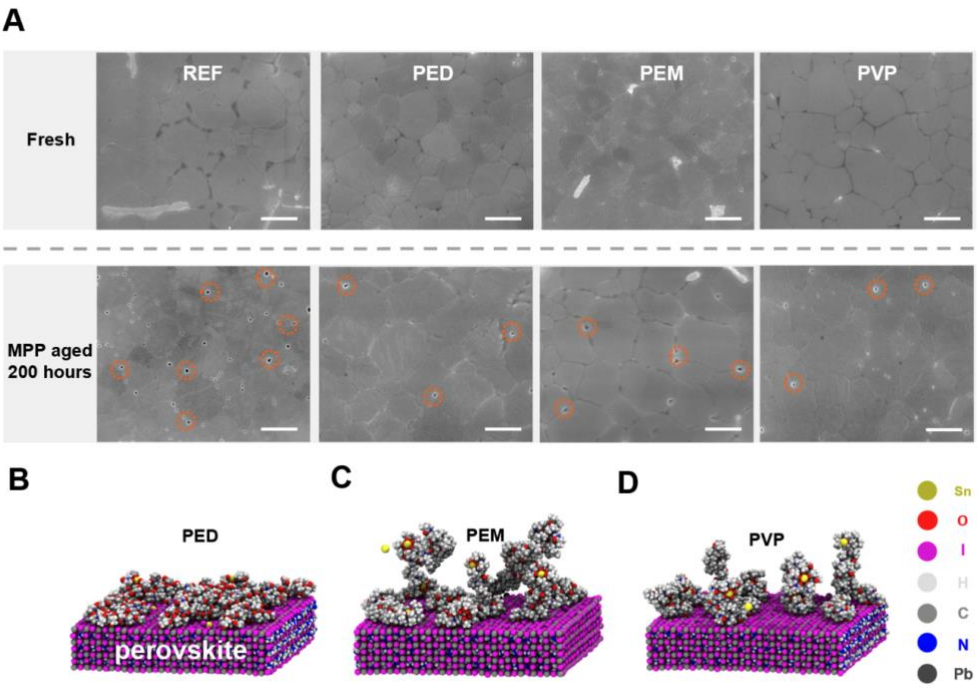

Figure 5.2 Polymeric interlayers preserve buried-interface morphology during operation. (A) SEM images (scale bar, 1 μm) of the buried perovskite surface with and without polymeric interlayers. Orange dashed circles highlight voids formed after aging. (B)–(D), MD simulation structures of PED (B); PEM (C); PVP (D) on the perovskite surface.

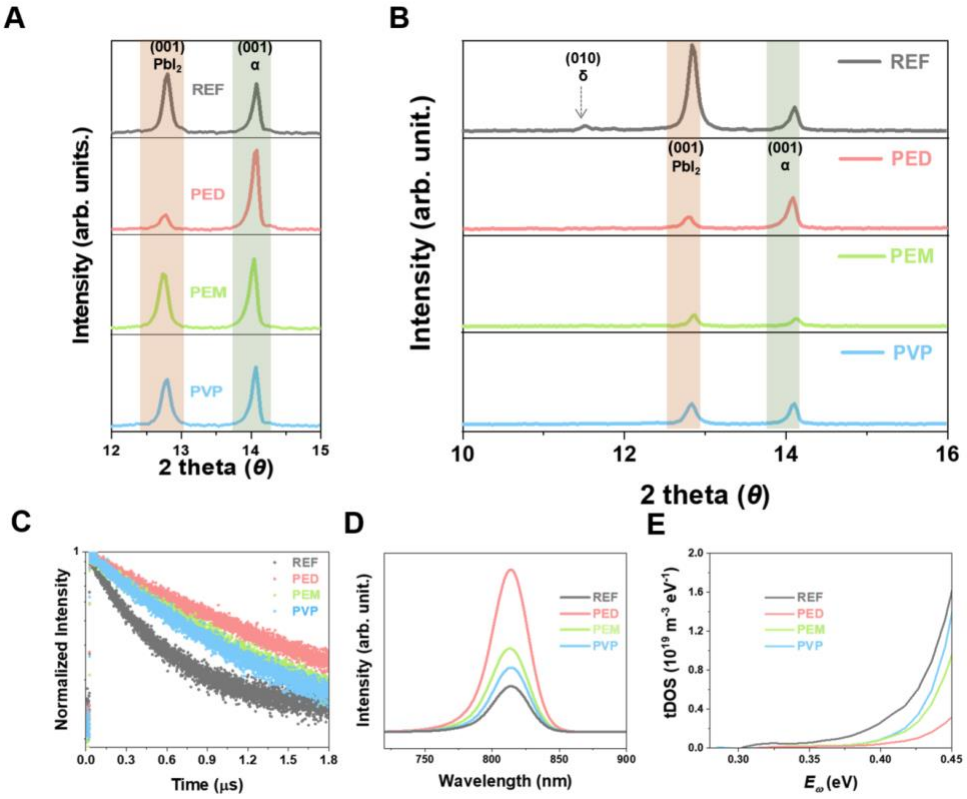

Figure 5.3 Polymeric interlayers improve perovskite phase quality and suppress defect-mediated recombination. (A) XRD patterns of buried perovskite interface with and without polymeric interlayers. (B) XRD patterns of buried perovskite surface after operation. (C) TRPL spectra without or with the polymeric interlayers. The testing structure was glass/ITO/SnO_2/perovskite. (D) Steady-state PL spectra. (E) tDOS in perovskite solar cells with or without polymeric interlayers.

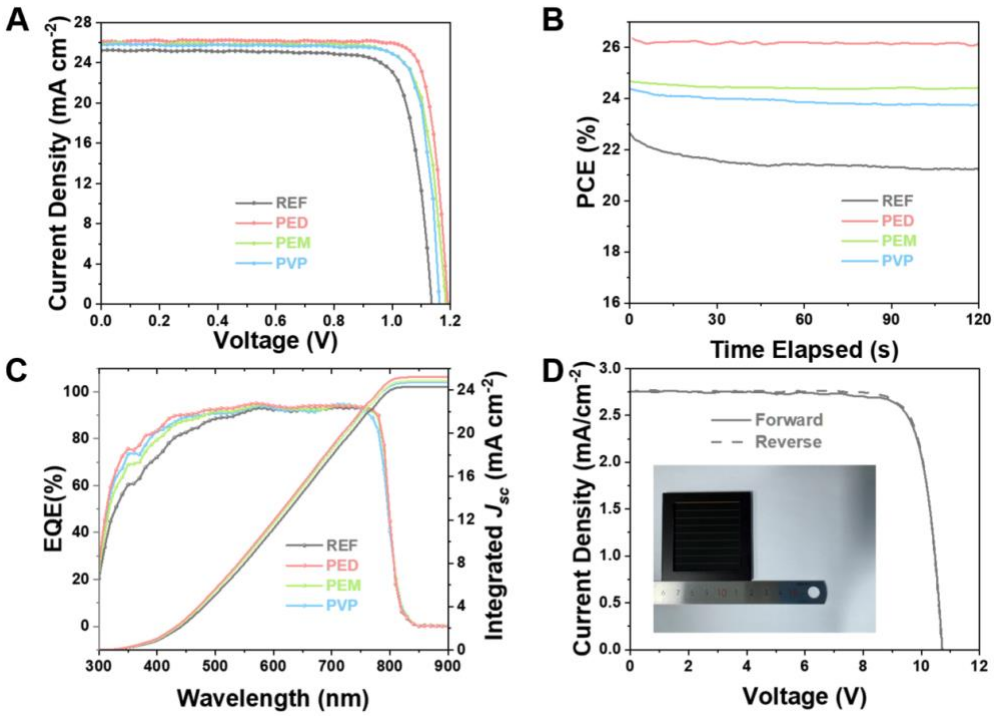

Figure 5.4 Polymeric interlayers enhance photovoltaic performance and device scalability. (A) *J–V* curves of devices with and without polymeric interlayers. (B) Stabilized power output measured under maximum power point tracking. (C) EQE spectra and integrated J_{sc} values of the best-performing devices. (D) Forward and reverse *J–V* curves of module with a PED interlayer.

Appendix A

Device fabrication

For the devices in Chapter 2: Indium-doped tin oxide (ITO)-coated glass was pre-patterned and cleaned with successive sonication in detergent, deionized water, acetone (99.9%, Sigma-Aldrich), and 2-propanol (IPA, 99.7%, Sigma-Aldrich) for 30 min, respectively. The substrates were dried under nitrogen flow and treated by UV-ozone to enhance the wettability and remove organic contaminants. A thin layer of tin oxide (SnO_2) nanoparticles (15 wt % in water, Alfa-Aesar) was spin-coated (3,000 rpm for 30 s) from a filtered aqueous solution (2 mg mL^{-1}) onto the ITO glass and annealed at 150 °C for 30 min. The SnO_2/ITO/glass substrates were transferred into a nitrogen glove box for perovskite film deposition after another treatment by UV-ozone. The PbI_2 (99.99%, Alfa-Aesar) solution was prepared by dissolving 1.5 M PbI_2 into 1 mL dimethylformamide (DMF, 99.8%, Sigma-Aldrich)/dimethyl sulfoxide (DMSO, 99.7%, Sigma-Aldrich) mixed solvent (v/v 9/1). The organic solution was prepared by dissolving 90 mg $HC(NH_2)_2I$ (FAI, 99%, GreatCell Solar), 6 mg CH_3NH_3Br (MABr, 99%, GreatCell Solar), and 9 mg CH_3NH_3Cl (MACl, 99%, Xi'an Polymer Light Technology) into 1 mL IPA. The solutions were stirred for over 1 hour before use. The PbI_2 solution was spin-coated on the substrate at 1,500 rpm for 30 s and annealed at 70 °C for 30 s. The FAI/MABr/MACl solution was spin-coated on the PbI_2 at 2,000 rpm for 30 s and annealed at 95 °C for 30 s; then, the film was annealed outside the glove box at 150 °C for 10 min with 40% humidity. Then, chlorobenzene (CB, 99.8%, Sigma-Aldrich) or polymer solutions was drop-casted at 2,000 rpm on the perovskite film. The film was dried at 80 °C for 30 s. The polymer materials (including poly(vinyl acetate) [PVA, 99.5%, Alfa-Aesar]), polyethylene glycol (PEG, 99.5%, Sigma-Aldrich), and poly(9-vinylcarbazole) (PVK, 99.5%, Alfa-Aesar) were dissolved in CB with different weight concentration. The Spiro-

OMeTAD solution (72.3 mg Spiro-OMeTAD [99.8%, Xi'an polymer light technology]) in 1 mL CB with 28 μL 4-tert-butyl pyridine (t-BP, 98%, Sigma-Aldrich) and 17.5 μL lithium bis(trifluorome-thanesulfonyl)imide (Li-TFSI, 99.95%, Sigma-Aldrich) (520 mg/mL in acetonitrile (99.8%, Sigma-Aldrich]) was spun onto the perovskite film at 3,000 rpm for 30 s by dropping 25 μL of the solution as a hole conductor. The devices were completed by evaporating 100 nm gold or silver in a vacuum chamber (base pressure, 5×10^{-6} Pa) at 0.5 Å s^{-1} on the top of spiro-MeOTAD layer. The device contact area was 0.12 cm^2.

For the devices in Chapter 4 and 5: The processes for substrate and SnO_2 are same as above. For the polymeric interlayers, PED was dissolved in chloroform (CF, 99.8%, Sigma-Aldrich) with a concentration of 1mg/ml. PEM and PVP were dissolved in CB with a concentration of 1mg mL^{-1}. The PED concentration was optimized through concentration-dependent device screening from 0.1 to 10 mg mL^{-1}, with 1 mg mL^{-1} providing the best representative photovoltaic performance and the most balanced improvement in V_{oc}, J_{sc}, and FF (**Figure B6.1**). PED was used as the representative polymer for concentration-dependent optimization because it showed the best overall device performance and buried-interface stabilization. After identifying 1 mg mL^{-1} as the optimized PED concentration, the same concentration was applied to PEM and PVP to ensure a fair comparison under identical processing conditions. The solutions were spin-coated at a speed of 3000 r.p.m. for 30 s and annealed at 75°C for 1 minute. This spin-coating condition was selected based on spin-speed-dependent device-performance screening using PED as the representative polymer interlayer (**Figure B6.2**). Additional attenuated total reflectance Fourier-transform infrared spectroscopy (ATR-FTIR) and proton nuclear magnetic resonance spectroscopy (^{1}H NMR) characterizations indicate that the polymer interlayers remain largely stable under the 150 °C perovskite annealing condition, with no obvious evidence of thermal decomposition or further

polymerization (**Figures B6.3**, **6.4** and **6.5**). For the fabrication of perovskite films, 1.5 M PbI_2 in DMF and DMSO (volume ratio, 9.5:0.5) was spin-coated at a rate of 1,500 r.p.m. for 30 s and annealed at 80 °C for 30 seconds. Organic salts of FAI/MACl/MABr (70 mg:10 mg:4 mg in 1 ml IPA) were spin-coated on PbI_2 films at a rate of 1,800 r.p.m. for 30 s, followed by thermal annealing at 150 °C for 13 min in ambient air with a controlled humidity (30–40%). The OAI solution (3 mg OAI was dissolved in 1 mL IPA) as a passivation procedure was spin-coated on perovskite films at 4000 rpm for 30 seconds. The processes for HTL layer and top electrode are same as above.

Module fabrication

Perovskite solar modules, consisting of nine sub-cells connected in series, were fabricated on FTO glass substrates with dimensions of 6 × 6 cm^2. The series interconnection of the module was achieved by patterning P1, P2, and P3 lines using a laser scribing system with a wavelength of 1064 nm and a power output of 20 W. The FTO substrate was pre-patterned for P1 (20 μm width) utilizing 40% laser power at a speed of 500 mm/s, a frequency of 200 kHz, and a pulse width of 50 ns. The subsequent processes were identical to those used for small-area devices.

The P2 lines (80 μm width) were etched prior to the Au evaporation step, using an average laser power of 33%, a speed of 500 mm/s, a frequency of 50 kHz, and a pulse duration of 50 ns. The distance between P1 and P2 was approximately 60 μm. Following the deposition of a 100 nm thick gold layer, the P3 line (10 μm width) was fabricated under the same scribing conditions as the P2 line. The distance between P1 and P3 was approximately 180 μm, and the geometric fill factor (GFF) was around 96.5%. Additionally, laser edge cleaning was applied to the perovskite components, resulting in a light-receiving area of 21.54 cm^2 for the perovskite component. And the certified test was conducted using a mask with an aperture area of 21.5 cm^2.

Polymers synthesis

For PED, the synthesis route is shown in **Figure B6.6**. Under a nitrogen atmosphere, 1-ethenylpyrrolidine-2,5-dione (Enamine) (0.2 mL) was dissolved in toluene (1 mL) together with 2,2′-azobis(2-methylpropionitrile) (AIBN, 0.002 g). The solution was heated and stirred at 80 °C for 14 hours to affect free-radical polymerization1,2. To improve the solubility of the product, 1mL chloroform (CF) was added to the solution. The mixture was then poured into diethyl ether (DE) to precipitate the polymer. The resulting precipitated polymer was collected by filtration, purified by three cycles of reprecipitation (dissolution in CF followed by precipitation with DE, and dried under vacuum to constant mass. The PED sample was obtained as flake-like solids (M_n=5033, M_w=7465) (**Figure B6.7**).

For PEM, the synthesis route is shown in **Figure B6.8**. Under a nitrogen atmosphere, 1-ethenyl-3-methylpyrrolidin-2-one (Enamine) (0.2 mL) was dissolved in toluene (1 mL) together with AIBN (0.002 g). The solution was heated and stirred at 80 °C for 14 hours to effect free-radical polymerization. To improve the solubility of the product, 1mL chlorobenzene (CB) was added to the solution. The mixture was then poured into diethyl ether (DE) to precipitate the polymer. The resulting precipitated polymer was collected by filtration, purified by three cycles of reprecipitation (dissolution in CB followed by precipitation with DE, and dried under vacuum to constant mass. The PEM sample appeared as a free-flowing granular powder (M_n=16304, M_w=62018) (**Figure B6.9**).

Characterization methods

FTIR spectroscopy was characterized by an FT/IR-6100 (Jasco) under purging with nitrogen gas. Silicon substrates were used for FTIR measurements. The UV-Vis absorption spectra were measured by a U4100 spectrophotometer (Hitachi). XRD was performed in regular q-2q

scanning mode using X-ray diffractometer (PANalytical, CuK_{a1}: l = 0.154056 nm) with a scan rate of 4 min^{-1}. The SEM (Nova Nano 230) and AFM (Bruker dimension fast scan) with peak-force tapping mode using silicon tips (OTESPA, Bruker) were used to characterize the morphology of the perovskite films. The PL signal was recorded using a Horiba Jobin Yvon system, whereas the time-resolved PL decay profiles were measured using a Picoharp 300 with time-correlated single-photon-counting capabilities. The films were excited using a 640 nm monochromatic pulse laser with a 100 kHz frequency provided by a picosecond laser diode head (PLD 800B, PicoQuant). XPS measurements were carried out on an XPS AXIS Ultra DLD (Kratos Analytical). An Al Kα (1,486.6 eV) X-ray was used as the excitation source. UPS measurements were carried out using a helium discharge lamp, emitting ultraviolet energy at 21.2 eV. All UPS measurements were performed using standard procedures with a −9V bias applied between the samples and the detectors. TA was based on a regenerative amplified Ti:Sapphire laser system from coherent (800 nm, 35 fs, 6 mJ/pulse, and 1 kHz repetition rate), nonlinear frequency-mixing techniques and the Helios spectrometer (Ultrafast Systems LLC). All the samples were excited using 370 nm laser source. Resistivity switching tests were measured using voltage sweep mode (CC=1 mA) on Keithley 4200 SCS under vacuum around 10^{-2} torr. X-ray absorption spectroscopy measurements were performed at the QAS (7-BM) beamline of National Synchrotron Light Source – II at Brookhaven National Laboratory. The measurements were performed in fluorescence mode and up to 50 scans for each sample were merged to improve the signal to noise ratio. Cross sectional TEM samples were prepared using Tescan Gaia3 Dual Beam FIB. STEM and EDS experiments were carried out by using a JEOL JEM-2800 S/TEM operated at 200 kV with dual 100 mm^2 silicon drift detector X-ray detectors. ICP-AES was performed on Shimadzu ICPE-9000. ICP-AES tuning solution and hydrochloric acid were from Alfa Aesar and Fisher Chemical, respectively. Standard

element solution was purchased from the National Center of Analysis and Testing for Nonferrous and Electronic Materials. The standard solution was diluted into 1,000.0, 500.0, 200.0, 100.0 and 20.0 ppb with 1% HCl for the calibration curve. Milli-Q water (18.2 MΩ) was used in all experiments. Collected perovskite powder was scraped from approximately 30 individual, fully fabricated devices (yielding about 0.2-0.5 mg per device to accumulate enough amount of powder for testing condition). Size exclusion chromatography (SEC) analysis was performed using a Tosoh EcoSEC Ambient (Room Temperature)-GPC equipped with two TSKgel SuperAW GPC columns connected in series (two SuperAWM-H; 6.0 mm I.D. x 15 cm) calibrated with a conventional calibration curve using Sigma-Aldrich monodisperse polystyrene standards ranging from 1.0 MDa to 500 Da. Dimethylformamide (DMF) with 0.1 wt% of Lithium Bromide (40 °C) was used as a carrier solvent at the flow rate of 0.6 mL/min. Samples were prepared at a concentration of around 1 mg/mL in DMF with 0.1% LiBr with a sample injection volume of 50 μL. Instrument equipped RI detector was used as the main source of peak detection, and peak analysis was conducted using EcoSEC Elite GPC System Workstation Software. J–V characterizations of the solar cells were carried out with a Keithley 2401 source meter, under simulated one-sun illumination (AM 1.5G, 100 mW cm−2; Oriel Sol3A with class AAA solar simulator, Newport). The intensity calibration of the light was done by a National Renewable Energy Laboratory (NREL)-certified Si photodiode with a KG-5 filter. For each condition, at least eight devices were fabricated and measured for statistical analysis. *J–V* characterizations were conducted from −0.1 V to 1.22 V at a scan rate of 0.1 V s^{-1}. The IPCE measurement was carried out using a specially designed system (Enli Tech) in a.c. mode (chopping frequency, 210 Hz) without bias light.

Computational methods

All Molecular Dynamics (MD) simulations were carried out using the GPU-accelerated version of AMBER24[1]. For molecular mechanics parameters, the General AMBER Force Field (GAFF) were used for PED, PEM and PVP and FA^+, following a standard protocol described in previous studies[2]. For the remaining ions, force-field parameters designated within AMBER24 code were selected. A large 10nm × 10nm $FAPbI_3$ perovskite slab, and a polymer layer on top with or without free Sn ions, were first generated. Initial geometries of the polymers (having few monomer units) were prepared by randomly placing 12 polymers on the surface using the PACKMOL code[3], ensuring a minimum intermolecular distance of 2 Å. Partial charges were generated via the Merz-Singh-Kollman scheme using HF/6-31G(d) as implemented in Gaussian09[4] and incorporated as restrained electrostatic potential (RESP) charges[5],[6]. Periodic boundary conditions were imposed. The whole structure was initially energy-minimized over 1000 MD steps, with positional restraints applied to all heavy atoms. Each system was then heated and equilibrated at 300 K for 4 ns, during which the temperature was controlled using a Langevin thermostat (collision frequency of 5.0 ps^{-1}). This was followed by an additional 2 ns of relaxation using a Berendsen barostat to equilibrate the system at a pressure of 1 atm. Lastly, all restraints are removed and a production run of 40 ns was performed, maintaining the system at a constant temperature of 300 K and a time-averaged pressure of 1 atm.

We calculated the energy barrier of tin migration through polymer materials on the perovskite surface with DFT. All simulations were performed in VASP (Vienna Ab initio Simulation Package) with a plane-wave basis and the projector-augmented wave (PAW) method[7],[8]. We used the Perdew–Burke–Ernzerhof (PBE) generalized-gradient functional for both the self-consistent field steps and the geometry optimizations. For the optimizations, we used a Γ-centered 2 × 2 × 1 k-point mesh and a 400eV plane-wave cutoff. Atoms and cell parameters were

relaxed with a conjugate-gradient algorithm until the residual forces were below 0.02 eV/Å. To avoid spurious interactions between periodic images, we added a 10–15 Å vacuum layer along the z direction. We placed the polymer atop the perovskite slab and made it laterally periodic, so its repeat matches the perovskite lattice.

We evaluated tin migration barriers by tracking how the energy changes as the tin ion moves along its migration pathway. First, we optimized the initial and final structures; tin ion above the polymer and tin at the polymer-perovskite interface. We then generated intermediate geometries by linearly interpolating between them and mapped the pathway with the nudged elastic band (NEB) method and constrained minimization, using 16 images in total. The energy barrier height was taken as the energy difference between a minimum-energy state and the saddle point along the path.

References

1 Case, D. A. et al. Amber 2025. University of California (2025).

2 Wang, J., Wolf, R. M., Caldwell, J. W., Kollman, P. A. & Case, D. A. Development and testing of a general amber force field. *Journal of Computational Chemistry* **25**, 1157–1174 (2004).

3 Martínez, L., Andrade, R., Birgin, E. G. & Martínez, J. M. PACKMOL: A package for building initial configurations for molecular dynamics simulations. *Journal of Computational Chemistry* **30**, 2157–2164 (2009).

4 Frisch, M. J. et al. Gaussian 09, Revision A.02. Gaussian, Inc. (2016).

5 Singh, U. C. & Kollman, P. A. An approach to computing electrostatic charges for molecules. *Journal of Computational Chemistry* **5**, 129–145 (1984).

6 Besler, B. H., Merz Jr, K. M. & Kollman, P. A. Atomic charges derived from semiempirical methods. *Journal of Computational Chemistry* **11**, 431–439 (1990).

7 Kresse, G. & Hafner, J. Ab initio molecular dynamics for liquid metals. *Physical Review B* **47**, 558 (1993).

8 Kresse, G. & Furthmüller, J. Efficiency of ab-initio total energy calculations for metals and semiconductors using a plane-wave basis set. *Computational Materials Science* **6**, 15–50 (1996).

Appendix B

B2

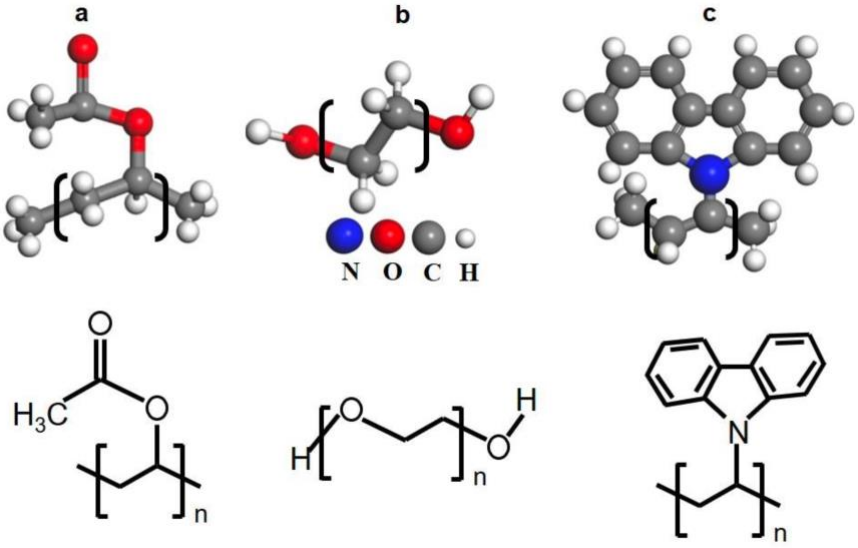

Figure B 2.1 Molecular structure. The molecular of the three passivating polymers, poly(vinyl acetate) (PVA) (a) polyethylene glycol (PEG) (b) and poly(9-vinylcarbazole) (PVK) (c).

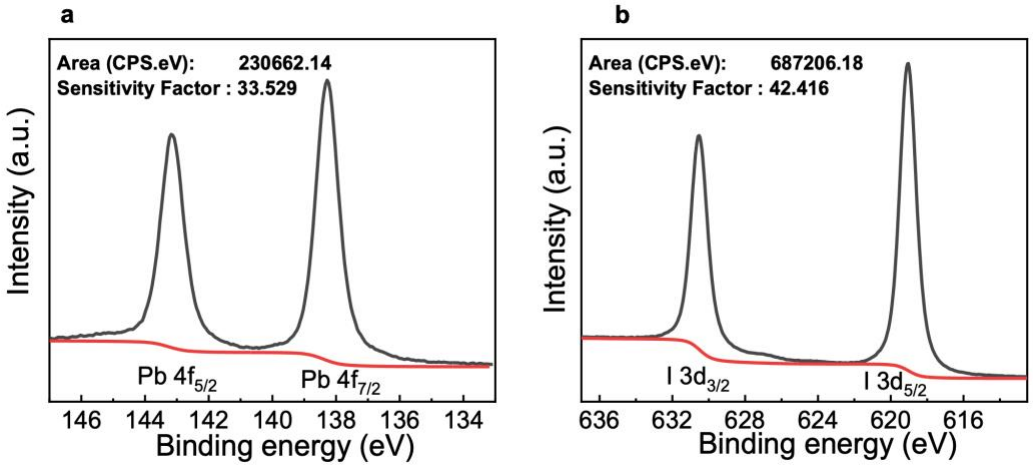

Figure B 2.2 Estimating the I/Pb ratio. High-resolution X-ray photoelectron spectroscopy (XPS) of the control perovskite film with an estimated penetration depth of 5-10 nm. The enlarged high resolution Pb *4f* and I *3d* spectra are shown in (a) and (b). The estimated I/Pb ratio for the pristine perovskite film from the XPS measurement was 2.355, indicating that an iodide-deficient characteristic exists in the neat perovskite film surface.

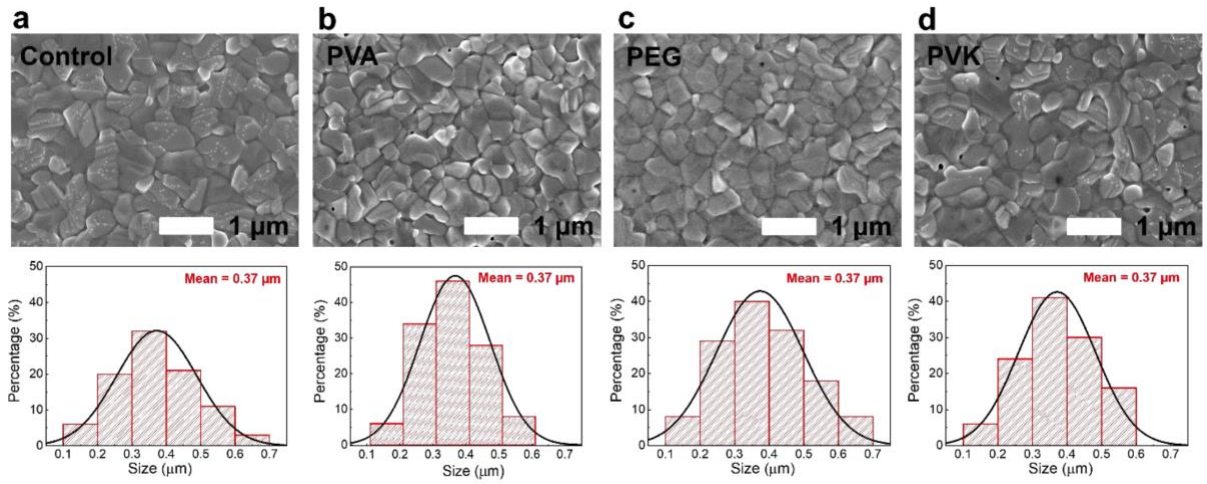

Figure B 2.3 The surface morphology of the perovskite films. Scanning electron microscopy (SEM) images of perovskite films (a) without and with surface treatment using (b) PVA, (c) PEG and (d) PVK and the corresponding statistical distribution of grains in the 5×4 μm^2 area. The average grain size of both control and polymer treated films are ~370 nm.

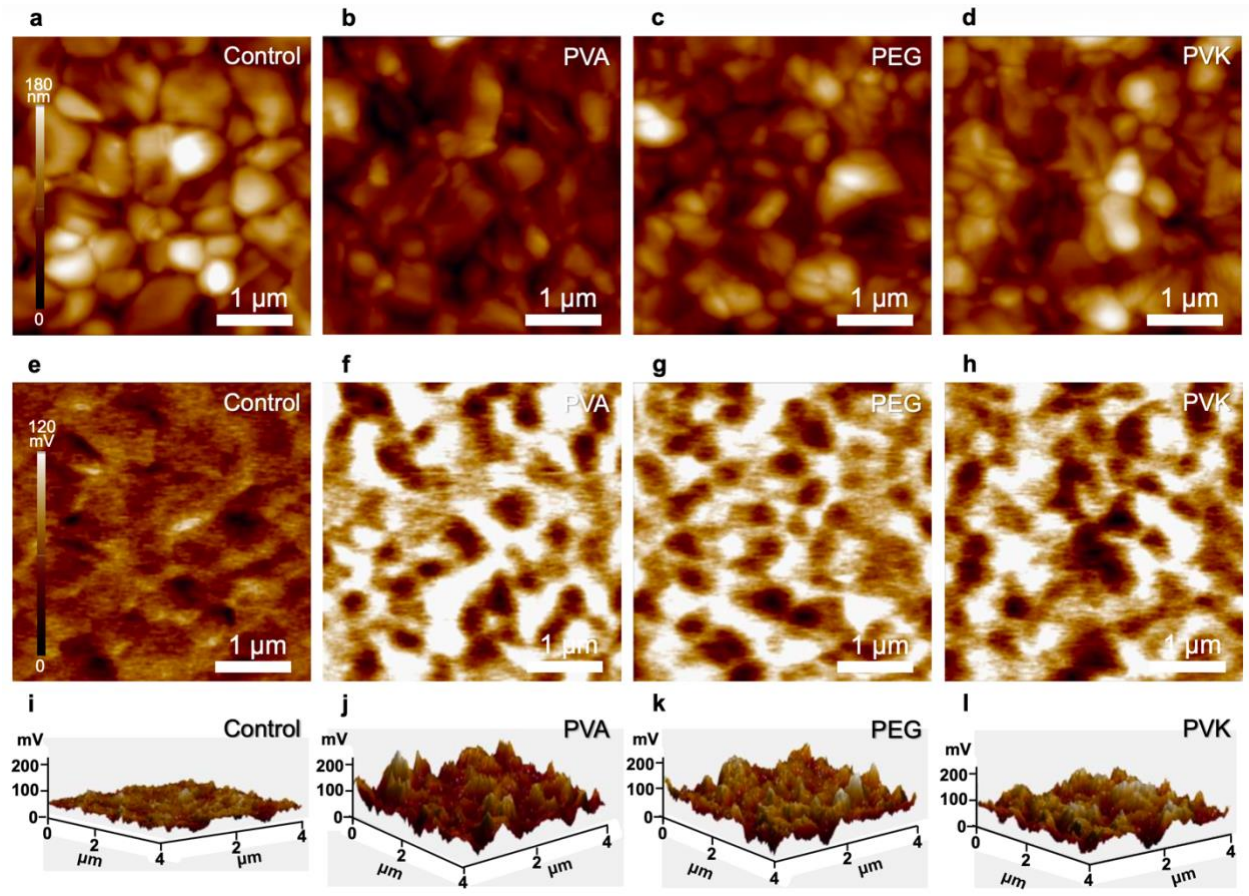

Figure B 2.4 The surface energy of the perovskite films. The surface 2D morphology, 2D and 3D Kelvin Probe Force Microscopy (KPFM) images of the perovskite films (a,e,i) without and with surface treatment using (b,f,j) PVA, (c,g,k) PEG and (d,h,l) PVK.

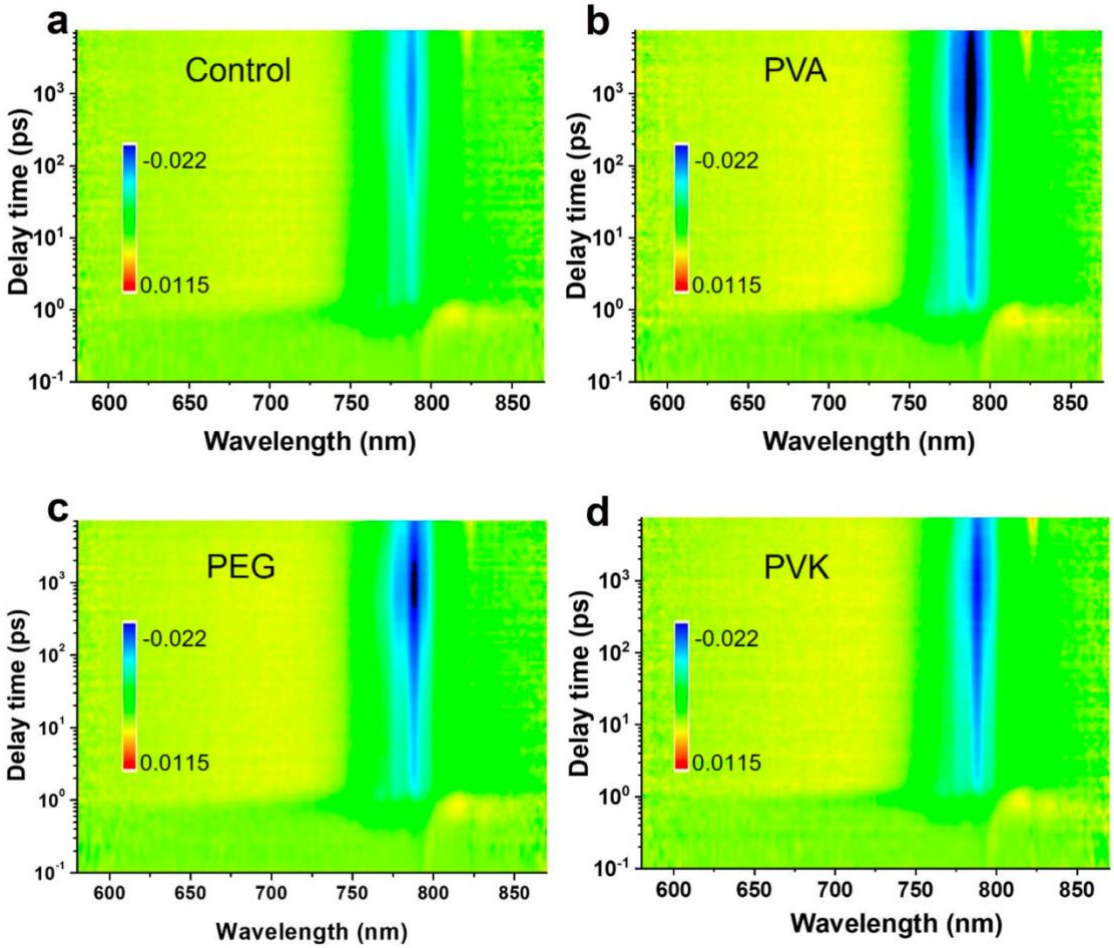

Figure B 2.5 The ultrafast transient absorption (TA) spectroscopy of the perovskite films. The TA decay curves of the perovskite films (a) without (control) and with the surface treatment using (b) PVA, (c) PEG and (d) PVK solutions, respectively.

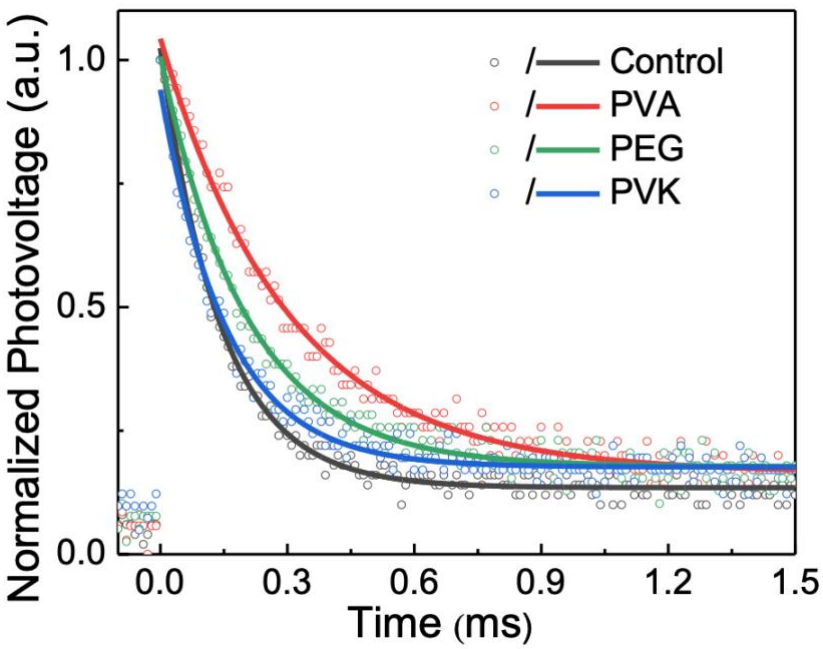

Figure B 2.6 Behavior of carriers in PSCs. Transient photovoltage (TPV) decay of the PSCs without and with polymer modification layers including PVA, PVK and PEG. The empty circles indicate measured data, and solid lines indicate fitted curves.

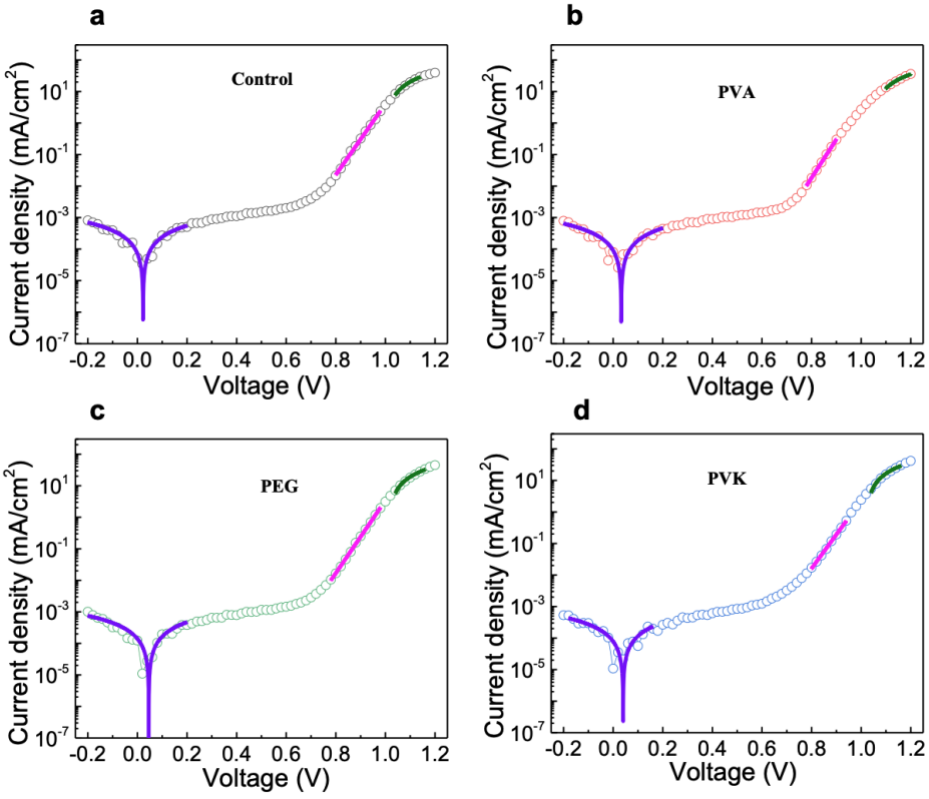

Figure B 2.7 Calculate the intrinsic parameters. Dark current density-voltage (*J-V*) characteristics of the perovskite solar cells (a) without (control) and with surface treatment with the (b) PVA, (c) PEG and (d) PVK solutions, respectively. The empty circles indicate the measured data, while the solid lines represent the fit of the data.

B3

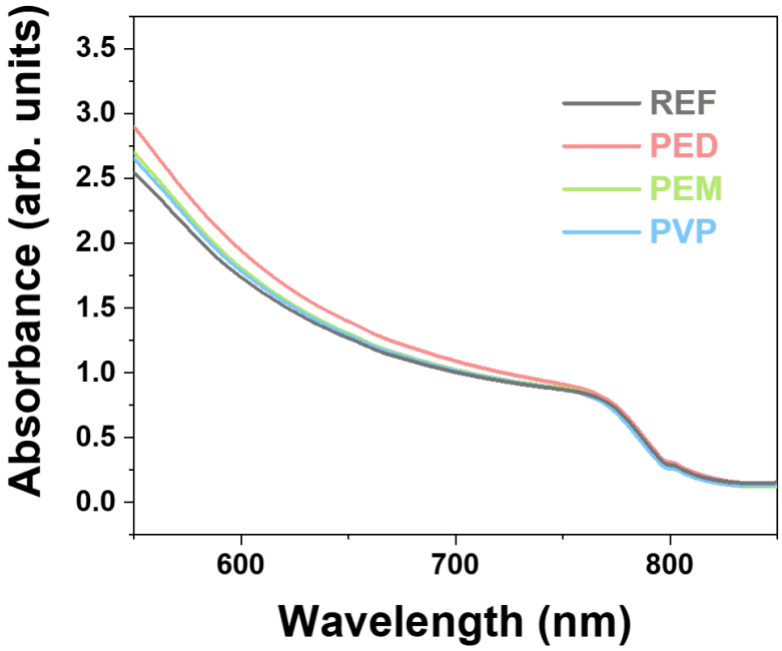

Figure B 3.1 UV-vis spectra of perovskite thin film.

B4

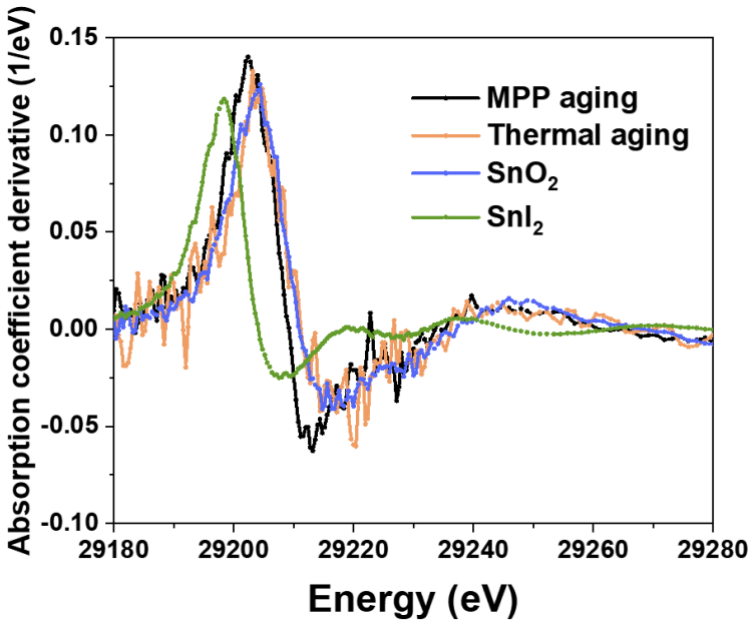

Figure B 4.1 Derivative of X-ray absorption coefficient in the Sn K-edge region for the MPP and thermal aging samples. SnO_2 and SnI_2 samples are used as references.

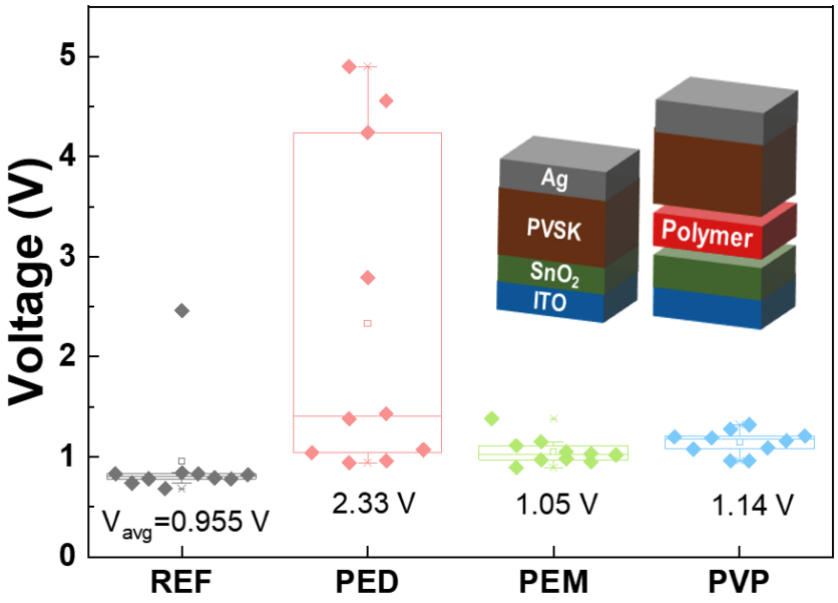

Figure B 4.2 Resistivity switching measurements for polymeric interlayers with SnO_2.

B5

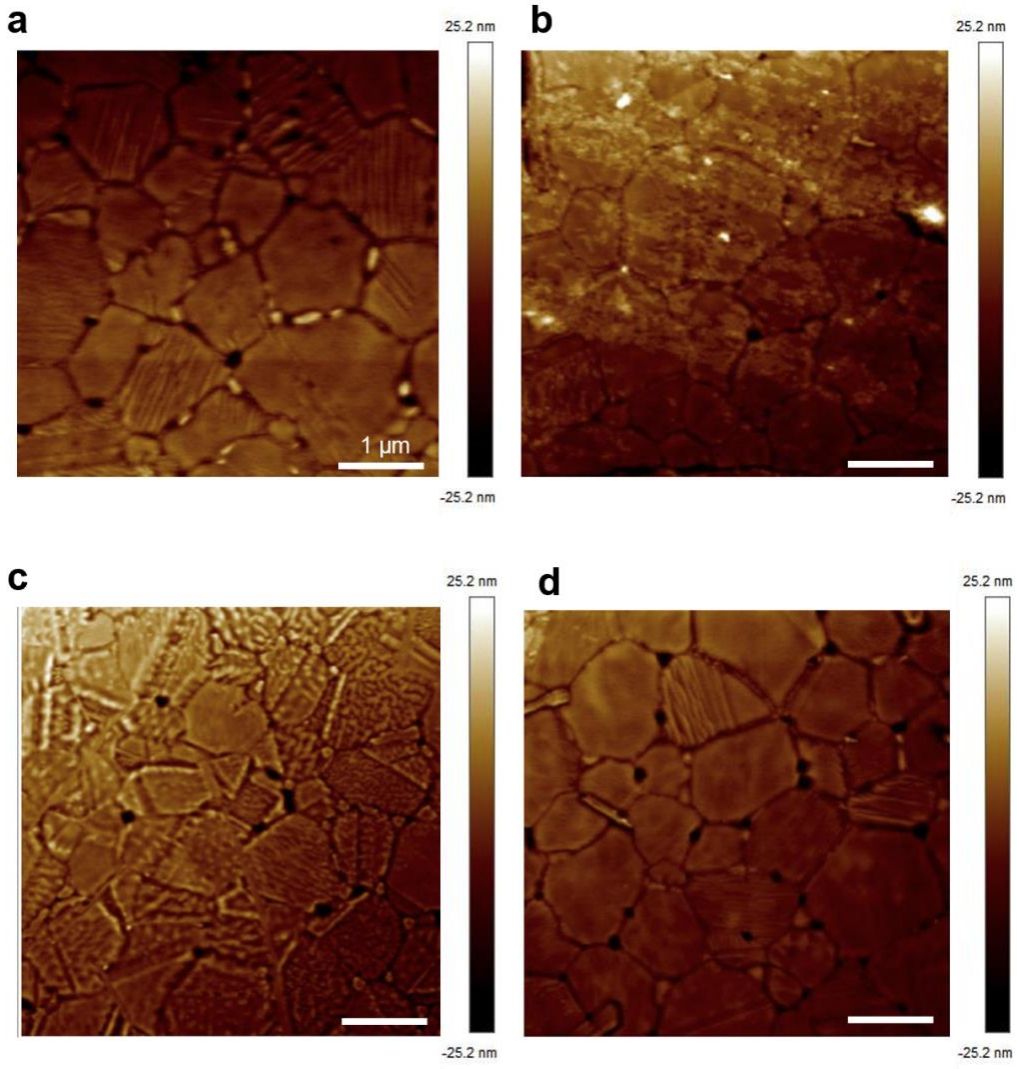

Figure B 5.1 AFM images for buried interface peeled from fresh device.

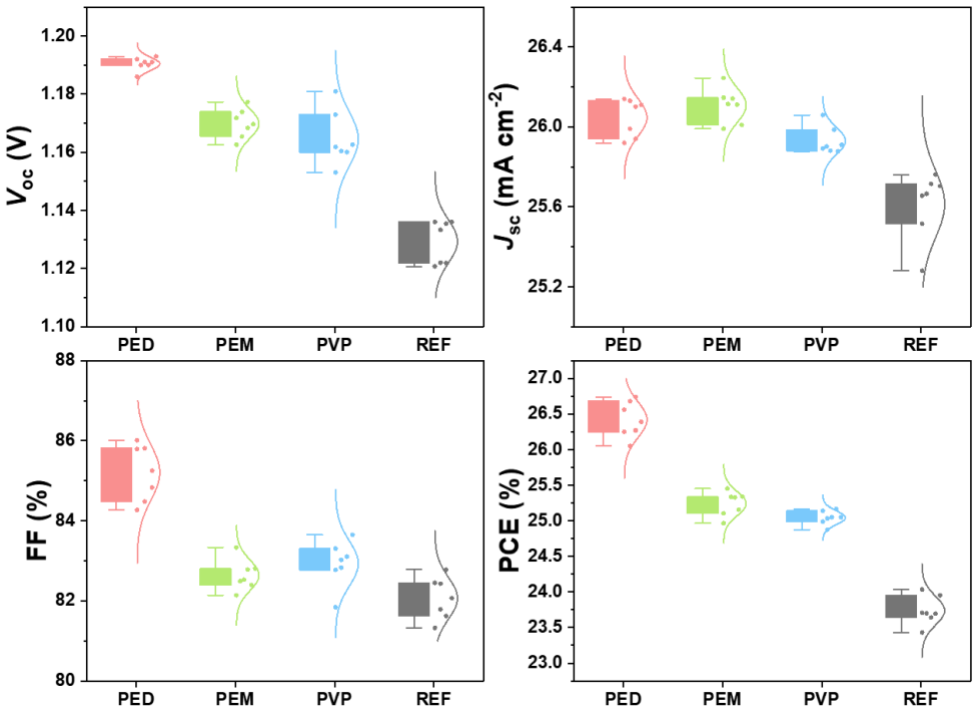

Figure B 5.2 Statistical photovoltaic parameters of devices with different polymeric interlayers and references. Results are extracted from 7 devices. Box plots show the median (center line), 25th–75th percentiles (box limits), and the 1.5× the interquartile range (whiskers). Individual data points are shown as diamonds, and the dashed curves represent the fitted normal distributions.

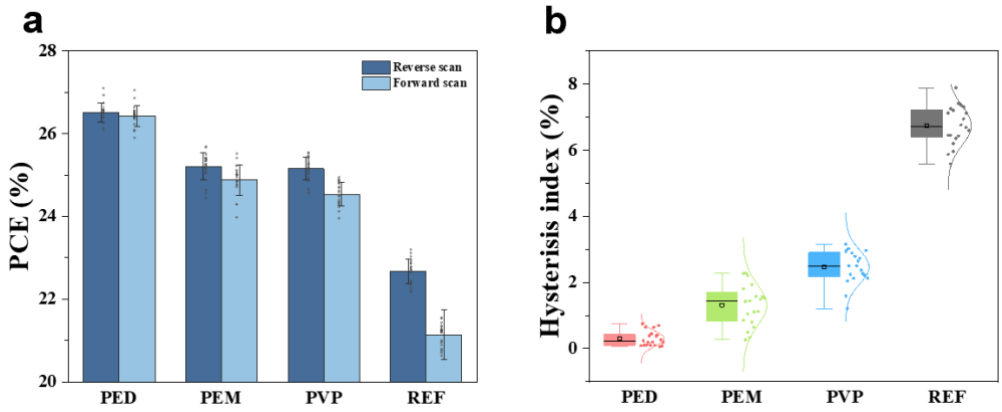

Figure B 5.3 Effects of polymer interlayers on device performance and hysteresis. a, Statistical comparison of reverse- and forward-scan PCEs for PED-, PEM-, PVP-modified and reference devices. Bars represent mean values, error bars represent standard deviation, and overlaid points represent individual devices (n = 20). b, Distribution of hysteresis index (HI) calculated from the same devices using $\mathbf{HI = (PCE_{reverse} - PCE_{forward})/PCE_{reverse} \times 100\%}$. Box-plots show the median and interquartile range, and overlaid points represent individual devices. Box plots show the median (center line), 25th and 75th percentiles (box limits), and the most extreme data points within 1.5× the interquartile range (whiskers). Squares represent the mean, individual data points are shown as dots, and the curves represent the fitted normal distributions.

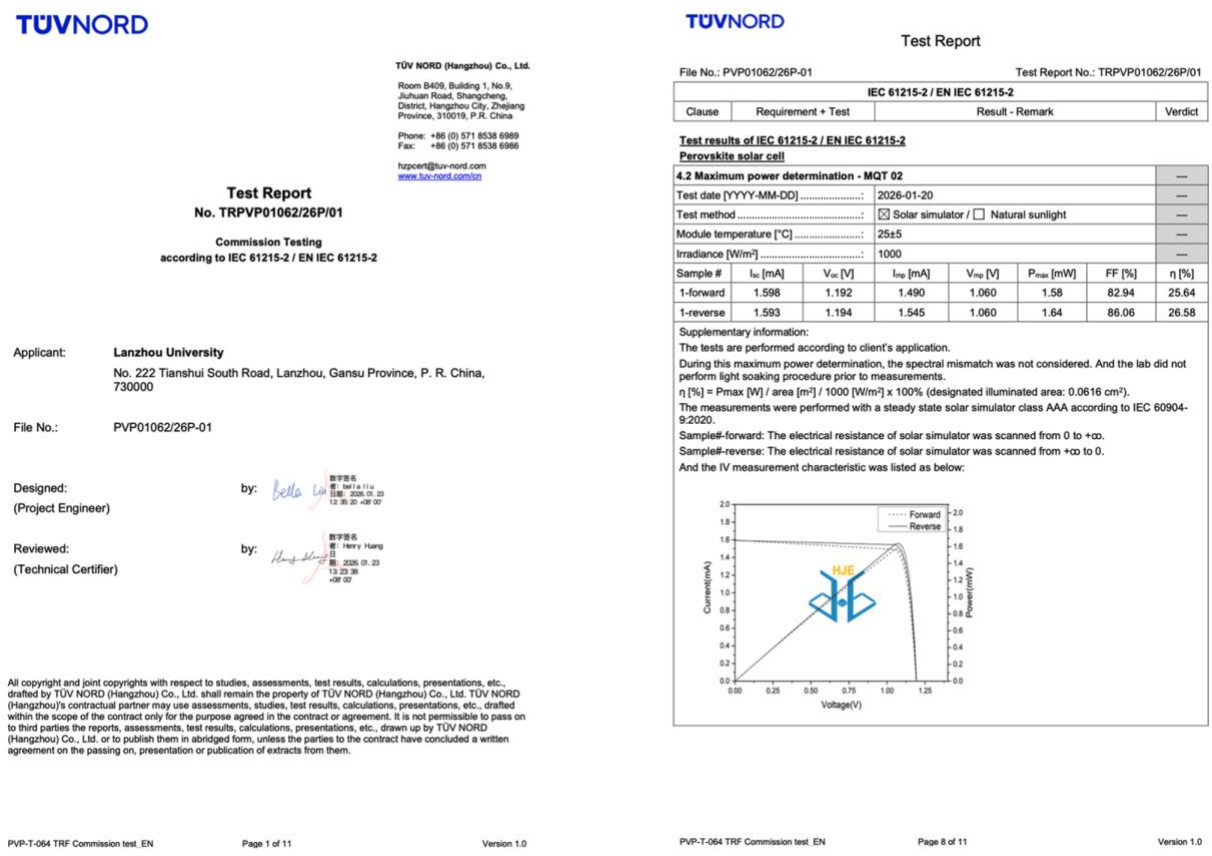

TÜVNORD

TÜV NORD (Hangzhou) Co., Ltd.

Room B409, Building 1, No.9, Jiuhuan Road, Shangcheng, District, Hangzhou City, Zhejiang Province, 310019, P.R. China

Phone: +86 (0) 571 8538 6989
Fax: +86 (0) 571 8538 6986

hzpcert@tuv-nord.com
www.tuv-nord.com/cn

Test Report
No. TRPVP01062/26P/01

Commission Testing
according to IEC 61215-2 / EN IEC 61215-2

Applicant: **Lanzhou University**
No. 222 Tianshui South Road, Lanzhou, Gansu Province, P. R. China, 730000

File No.: PVP01062/26P-01

Designed: by:
(Project Engineer)

Reviewed: by:
(Technical Certifier)

TÜVNORD

Test Report

File No.: PVP01062/26P-01 Test Report No.: TRPVP01062/26P/01

IEC 61215-2 / EN IEC 61215-2		
Clause	Requirement + Test	Result - Remark	Verdict

Test results of IEC 61215-2 / EN IEC 61215-2
Perovskite solar cell

4.2 Maximum power determination - MQT 02							—
Test date [YYYY-MM-DD] ..... :	2026-01-20						—
Test method ..... :	☒ Solar simulator / ☐ Natural sunlight						—
Module temperature [°C] ..... :	25±5						—
Irradiance [W/m²] ..... :	1000						—
Sample #	I_{sc} [mA]	V_{oc} [V]	I_{mp} [mA]	V_{mp} [V]	P_{max} [mW]	FF [%]	η [%]
1-forward	1.598	1.192	1.490	1.060	1.58	82.94	25.64
1-reverse	1.593	1.194	1.545	1.060	1.64	86.06	26.58

Supplementary information:
The tests are performed according to client's application.
During this maximum power determination, the spectral mismatch was not considered. And the lab did not perform light soaking procedure prior to measurements.
η [%] = Pmax [W] / area [m²] / 1000 [W/m²] x 100% (designated illuminated area: 0.0616 cm²).
The measurements were performed with a steady state solar simulator class AAA according to IEC 60904-9:2020.
Sample#-forward: The electrical resistance of solar simulator was scanned from 0 to +∞.
Sample#-reverse: The electrical resistance of solar simulator was scanned from +∞ to 0.
And the IV measurement characteristic was listed as below:

Figure B 5.4 Independent efficiency certification of PSC small-area device.

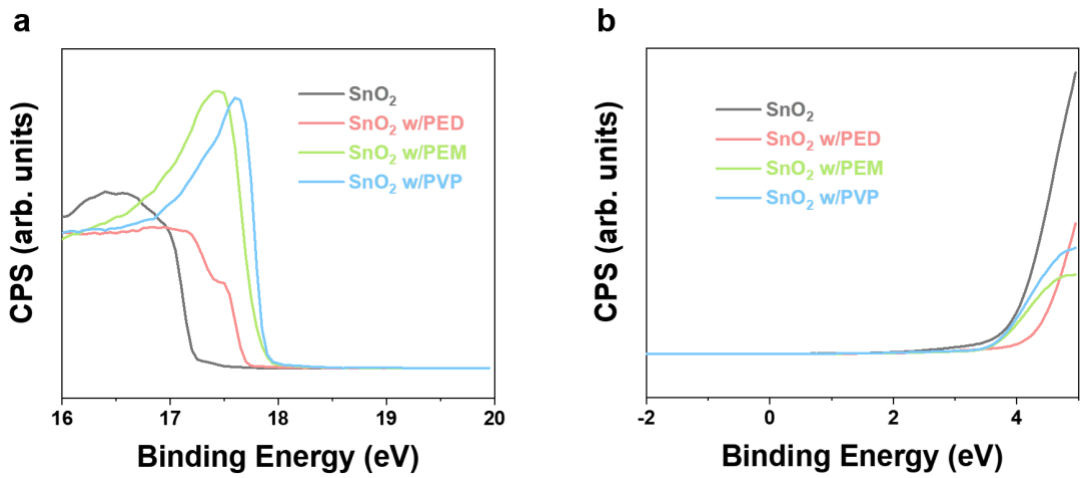

Figure B 5.5 UPS spectra of SnO_2 and polymer-modified SnO_2 buried interfaces. a, Valence-band onset region near the Fermi level; b, secondary electron cutoff region.

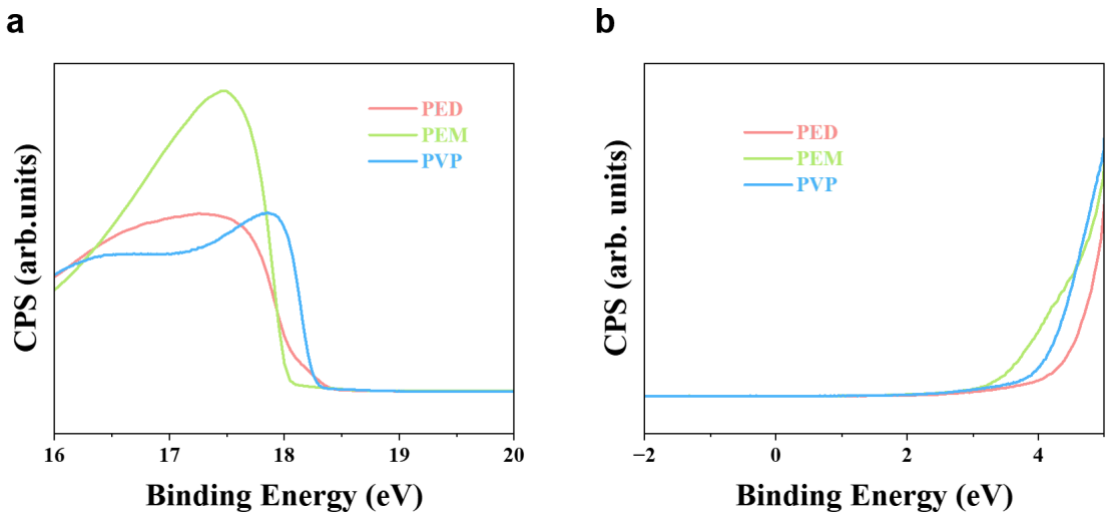

Figure B 5.6 UPS spectra of polymer only films. a, HOMO onset region near the Fermi level; b, secondary electron cutoff region.

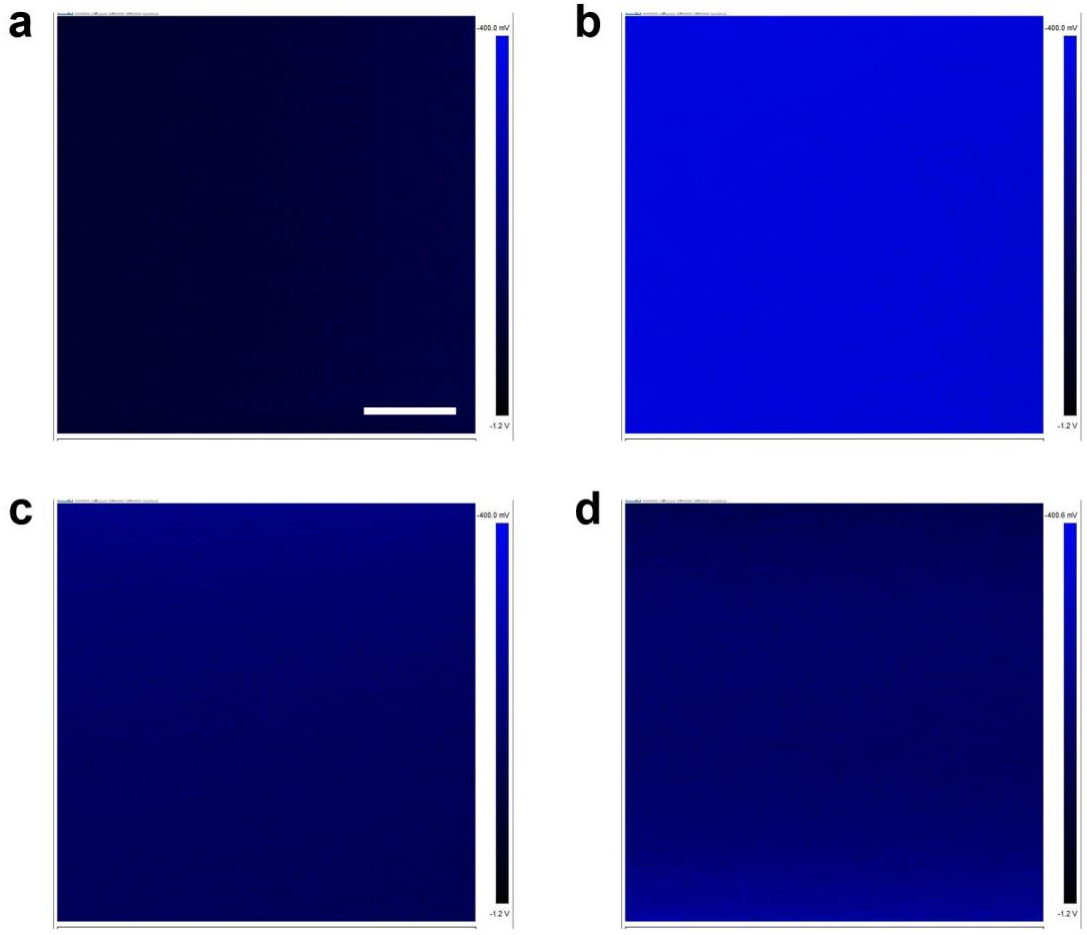

Figure B 5.7 KPFM for the buried interface work function. a, ITO/SnO_2; b, ITO/SnO_2/PED; c, ITO/SnO_2/PEM; d, ITO/SnO_2/PVP (scale bar, 1 μm).

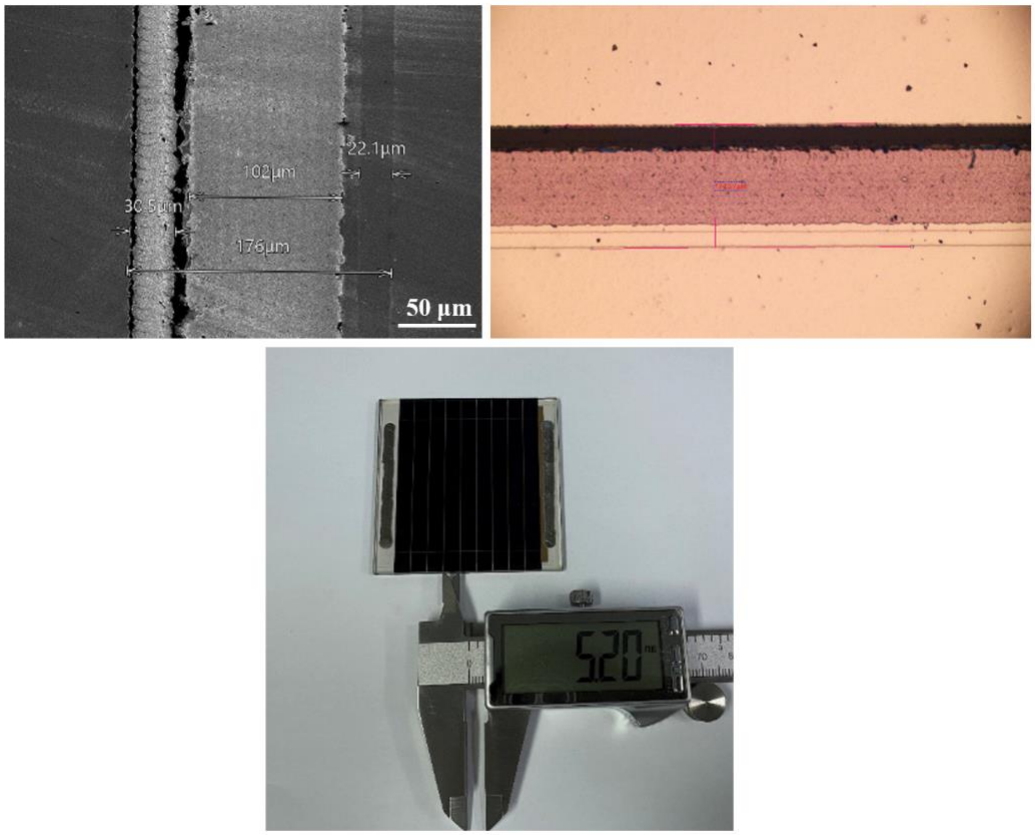

Figure B 5.8 Experimental verification of the module GFF and scribing quality.

B6

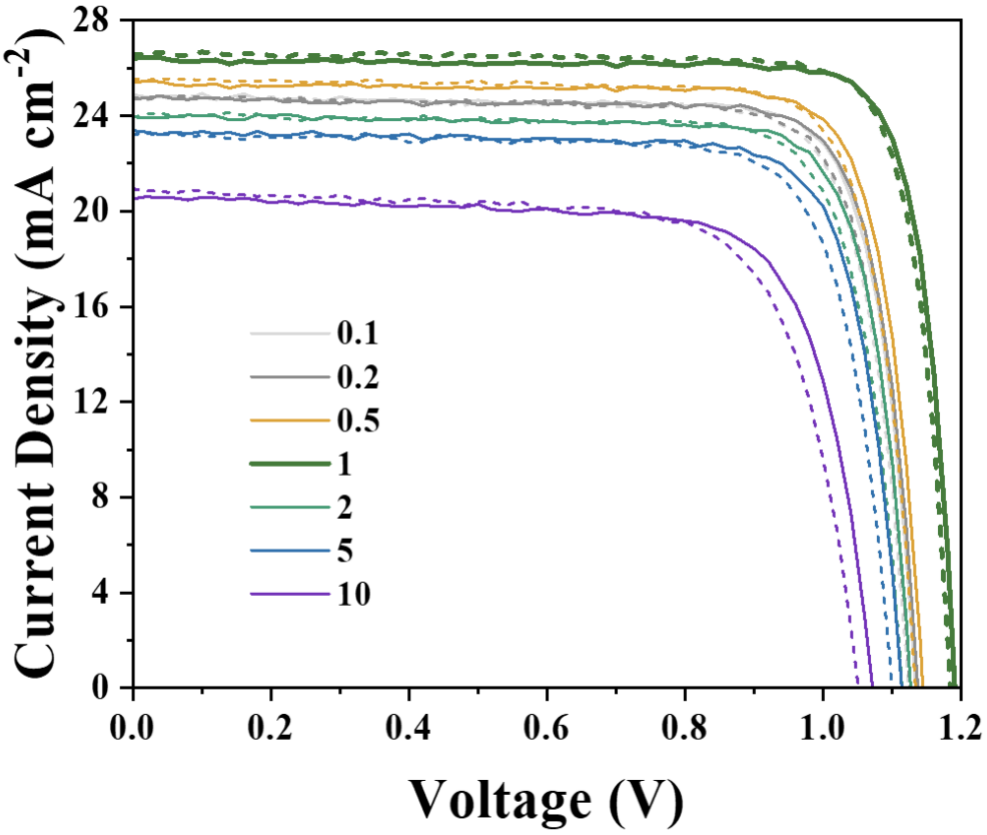

Figure B 6.1 Concentration-dependent device performance of PED-modified devices.

The unit of concentration is mg ml^{-1}.

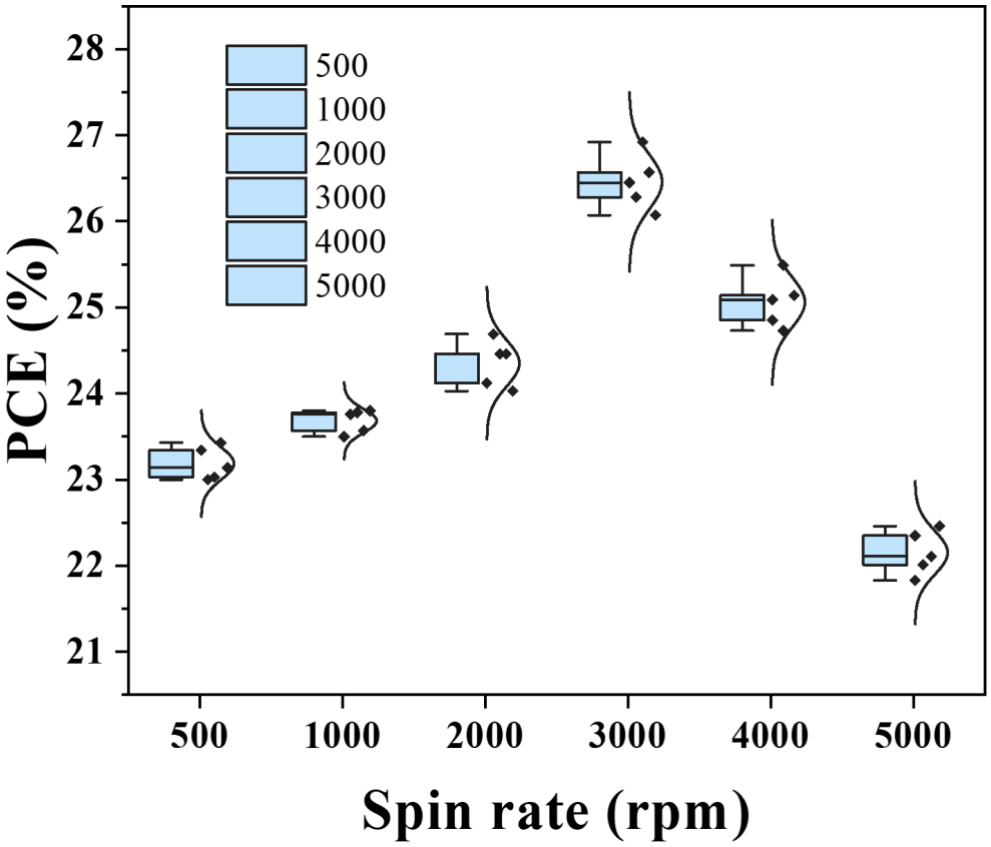

Figure B 6.2 Spin-speed-dependent device-performance screening of PED-modified devices

Results are extracted from 5 devices. Box plots show the median (center line), 25th and 75th percentiles (box limits), and the most extreme data points within 1.5 × the interquartile range (whiskers). Diamonds represent individual data points, and the curves represent the fitted normal distributions.

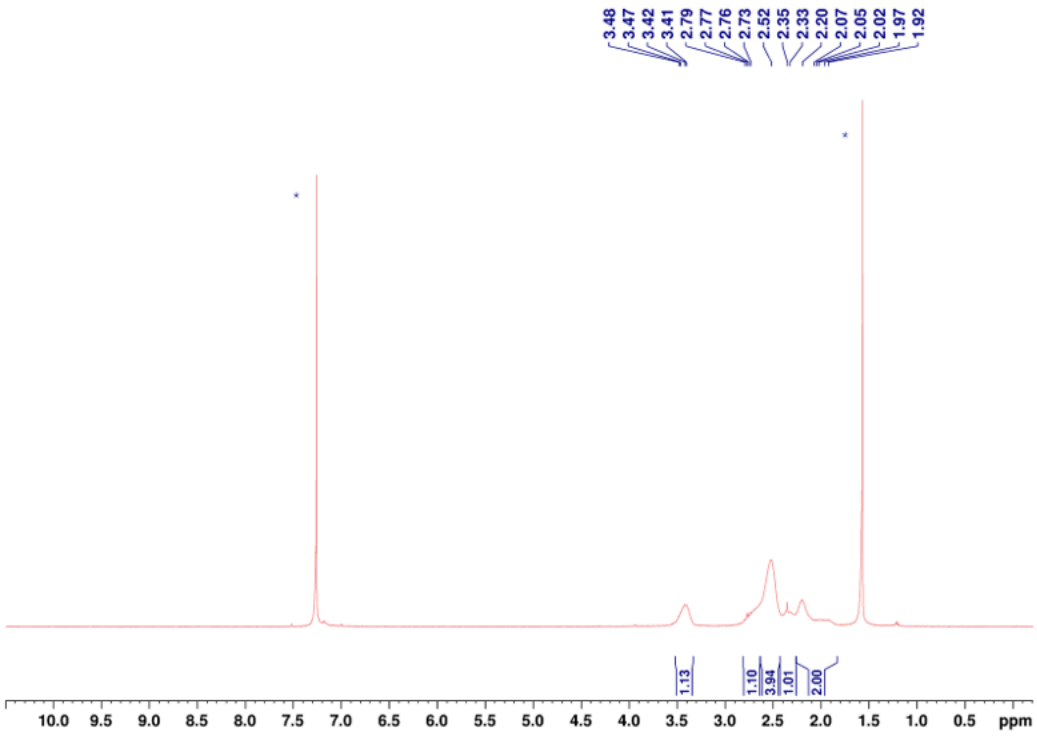

Figure B 6.3 ^{1}H NMR of PED.

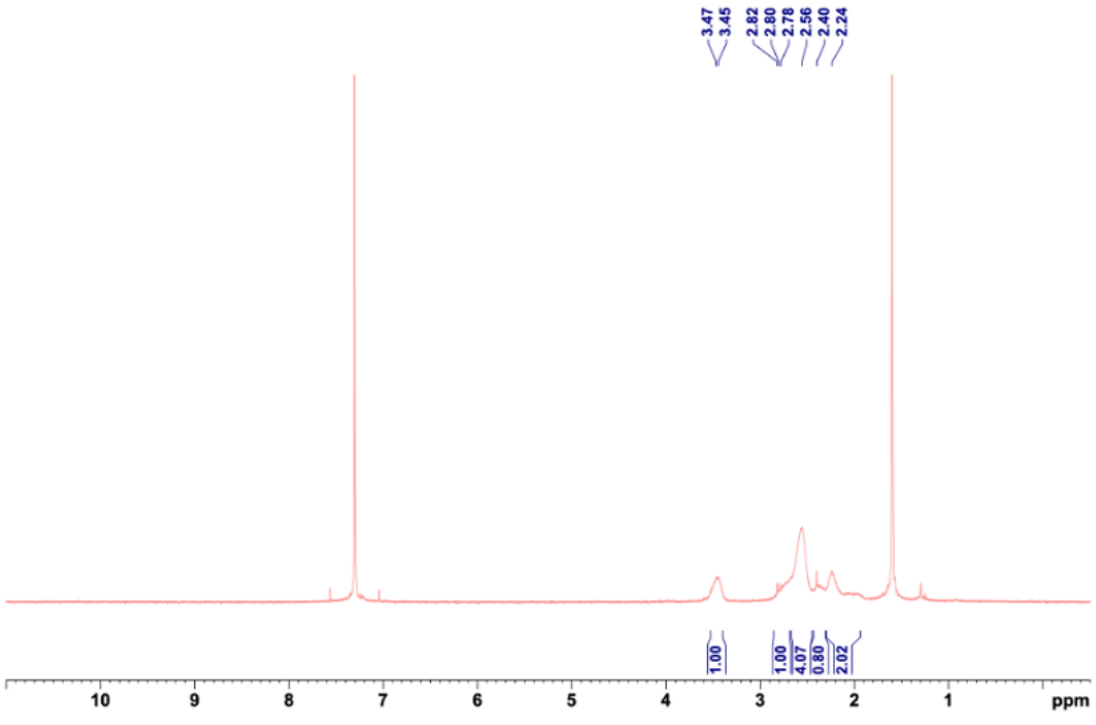

Figure B 6.4 ^{1}H NMR of PED after annealing at 150 °C for 13 minutes.

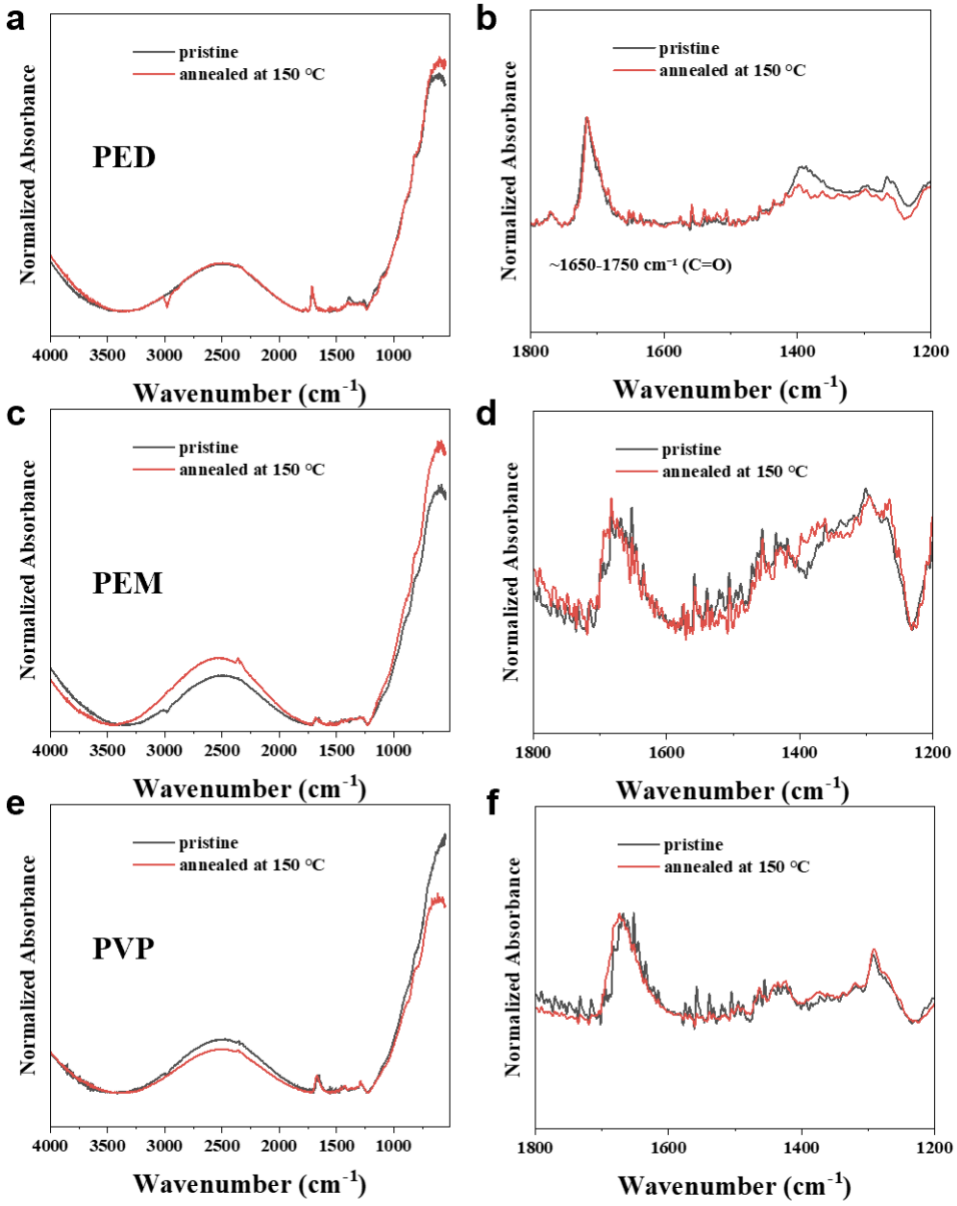

Figure B 6.5 ATR-FTIR characterization of polymer thermal stability under the perovskite annealing condition. a, c, e, Full-range normalized absorbance FTIR spectra of PED, PEM, and PVP, respectively, before and after annealing at 150 °C. b, d, f, Corresponding enlarged spectra in the 1800–1200 cm^{-1} region, covering the carbonyl-related and adjacent fingerprint regions. The spectra were baseline-corrected and normalized for comparison of peak positions and characteristic vibrational features.

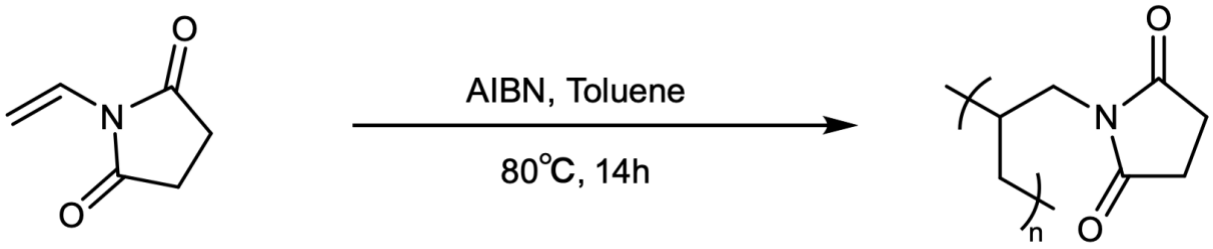

Figure B 6.6 Synthesis route of PED.

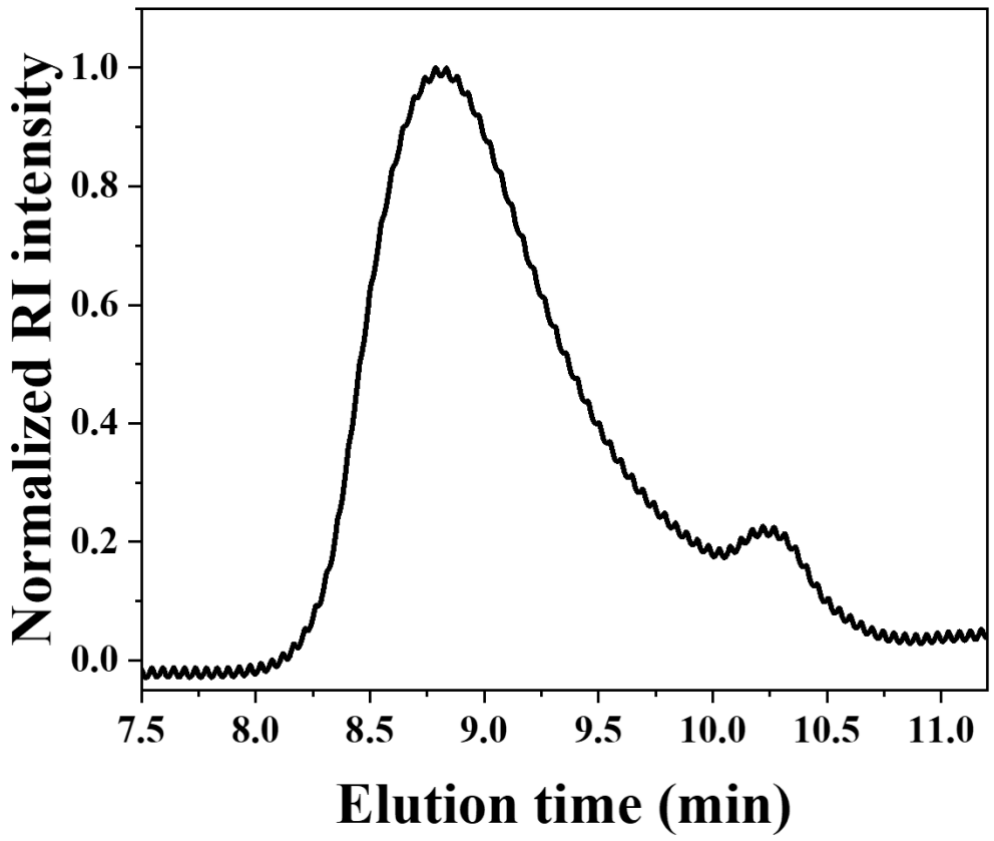

Figure B 6.7 GPC characterization of purified PED. The chromatogram is dominated by a main polymer peak. The purified PED exhibits M_n = 5,033, M_w = 7,465, and $Đ = M_w/M_n$ = 1.48. RI, refractive index.

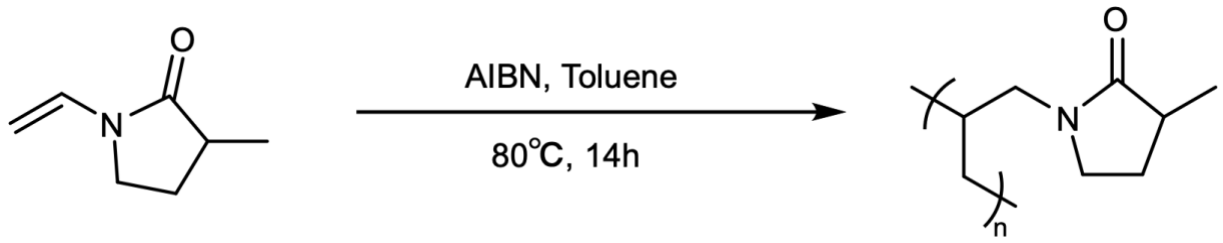

Figure B 6.8 Synthesis route of PEM.

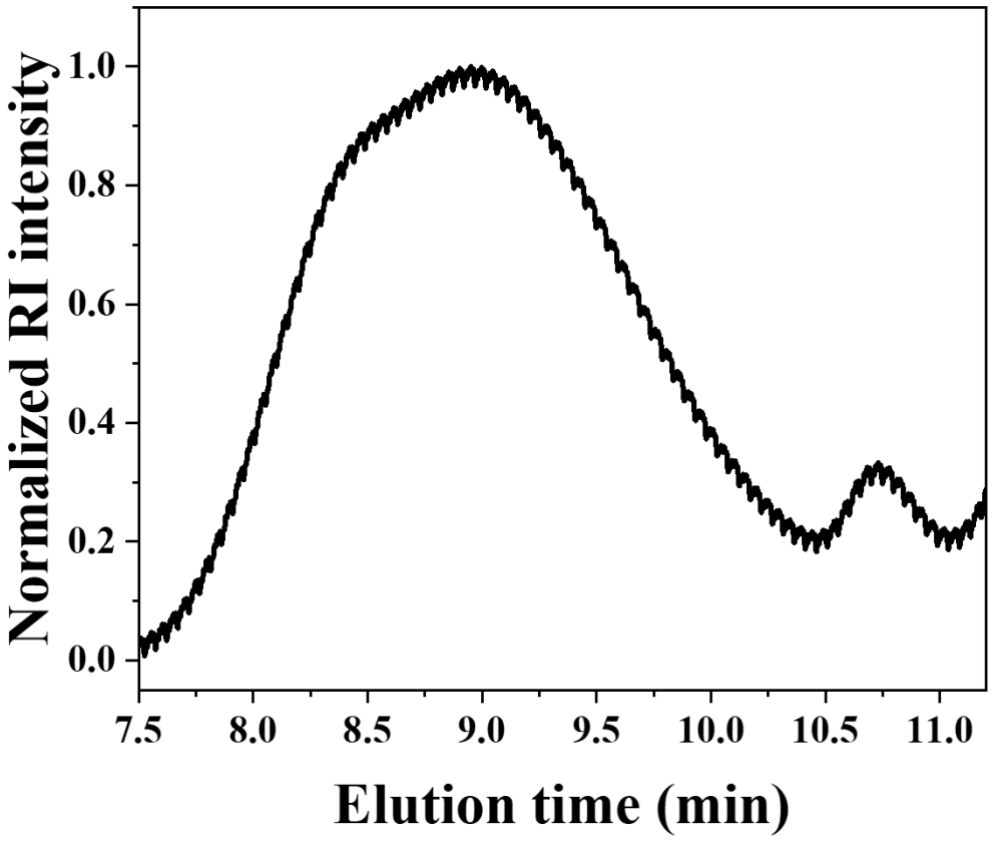

Figure B 6.9 GPC characterization of purified PEM. The chromatogram is dominated by a main polymer peak. The purified PEM exhibits M_n = 16304, M_w = 62018, and $Đ = M_w/M_n$ = 3.804.

Appendix C

C2

Table C 2.1 Fitted parameters for time resolved photoluminescence decay curves in Figure 2.3C.

	Control	PVA	PEG	PVK
A_1	0.466	0.120	0.170	0.182
Proportion [%]	57.11	15.38	22.42	22.58
τ_1 [ns]	95.8	110.8	100.0	80.0
A_2	0.350	0.660	0.588	0.624
Proportion [%]	42.89	84.62	77.57	77.42
τ_2 [ns]	339.9	1026.7	688.5	470.7
τ [ns]	139.3	877.2	556.5	382.4

Table C 2.2 Photovoltaic parameters

		Voc [V]	Jsc [mA cm^{-2}]	FF [%]	PCE [%]
Ref	forward	1.118	23.31	69.1	18.01
	reverse	1.120	23.28	78.5	20.47
PVA	forward	1.146	25.25	78.7	22.77
	reverse	1.149	25.24	80.0	23.20
PEG	forward	1.112	24.92	75.5	20.92
	reverse	1.126	24.94	79.6	22.35
PVK	forward	1.104	25.19	75.0	20.86
	reverse	1.106	25.27	78.6	21.97

The parameters of the PSCs tested under standard solar simulator (100 $mW \cdot cm^{-2}$ illumination, AM 1.5G). Open-circuit voltage (V_{OC}), short-circuit current density (J_{SC}), fill factor (FF), and power conversion efficiency (PCE).

Table C 2.3 Fitted parameters for dark *J-V* measurement in Figure B2.7. Series resistance (R_s), shunt resistance (R_{sh}), saturation current (J_0), and ideality factor (n)

	R_s [Ω cm^2]	R_{sh} [Ω cm^2]	J_0 [mA/cm^2]	*n*
Control	4.78	3.18×10^{5}	3.22×10^{-11}	1.58
PVA	4.39	3.61×10^{5}	3.17×10^{-12}	1.37
PEG	4.51	3.27×10^{5}	1.01×10^{-11}	1.45
PVK	4.73	3.19×10^{5}	3.05×10^{-11}	1.55

C3

C4

Table C 4.1 | XPS survey spectrum for aged reference sample

Name	Pos.	FWHM	Area	At%
N *1s*	399.91	2.16	1473.86	4.92
C *1s*	284.91	3.19	9729.99	58.5
O *1s*	532.91	2.83	6427.29	13.19
Sn *3d*	485.91	2.54	1041.87	0.25
Pb *4f*	137.91	2.22	42939.04	11.35
I *3d*	617.91	2.41	53716.62	9.6
Br *3p*	185.91	3.03	1824.88	2.18

C5

Table C 5.1 Calculated effective valence/HOMO levels of SnO_2 and SnO_2/polymer stacks from UPS results

Condition	SnO_2	SnO_2 w/PED	SnO_2 w/PEM	SnO_2 w/PVP
Cut-off Energy (eV)	17.18	17.65	17.82	17.89
Work function Φ (eV)	4.03	3.56	3.39	3.32
Valence/HOMO Onset (eV)	3.92	4.38	3.61	3.67
Calculated effective valence/HOMO level vs vacuum (eV)	-7.95	-7.94	-7.00	-6.99